MONTANUNIVERSITÄT LEOBEN

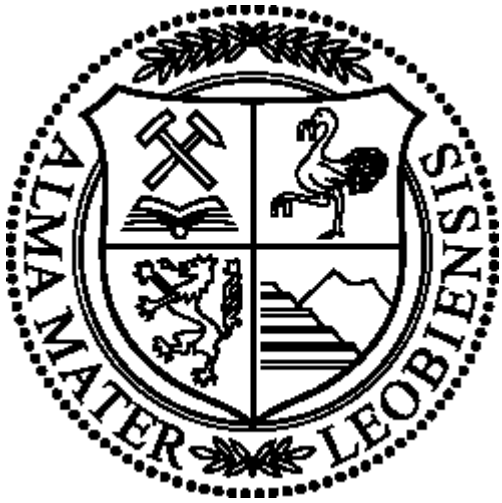

BENCHMARK STUDY OF CO_2 STORAGE IN THE JOHANSEN FORMATION

Master thesis

BENCHMARK STUDIE DER CO_2 SPEICHERUNG IN DER JOHANSEN FORMATION

Masterarbeit

Kata Kurgyis

Chair of Reservoir Engineering

Department of Petroleum Engineering

June 2015

Abstract

The increase of greenhouse gas in the atmosphere, particularly carbon-dioxide (CO_2), is often assumed as one of the main causes of climatic change. A potential short-term mitigation is a reduction of anthropogenic CO_2 emissions into the atmosphere via capture and geological storage. Thus, an important aspect of understanding the migration process taking place in the underground is the simulation of large-scale projects.

The aim of this study is to benchmark existing commercial and non-commercial simulators using a candidate site for large scale CO_2 sequestration as a simulation model. The setup of the model involves injection of carbon-dioxide into the Johansen formation. For the simulation of this assumed two-phase fluid process, three different simulators were used: Eclipse, IMEX and Open Porous Media (OPM). The following properties were compared: change of water volume and injected gas volume in the field (under reservoir and surface conditions), pressure and saturation profiles of the two phases, and simulation run-times.

The proposed benchmark is subdivided into two cases: the first case considers a model where both fluids are incompressible, while the second case considers fluids with varying degree of compressibility. In both cases the two-phase fluid flow is assumed isothermal and immiscible, where geo-mechanical and geochemical effects are neglected. The aim is to compare the capabilities and limits of the reservoir simulators using equivalent conceptual model definitions for input. The same corner point grid, identical Pressure-Volume-Temperature (PVT) tables and relative permeability curves for the fluid and rock model, equivalent initial conditions and well constraints were used for all simulators.

Comparing the computational efforts needed for the two cases has shown that calculation time increases with the introduction of compressibility as well as the Finite Volume method – Two-point flux approximation as a spatial discretization (i.e. in OPM). While using the commercial programs of Eclipse and IMEX the numerical simulations achieve a shorter run-time, however the formulation of fluid incompressibility is inaccurate.

Kurzfassung

Der dramatische Anstieg der Treibhausgaskonzentration in der Atmosphäre, vor allem von Kohlendioxid (CO_2), wird oft als die Hauptursachen des Klimawandels betitelt. Ein technischer Ansatz um anthropogenen Beitrag am Klimawandel zu reduzieren ist die Abscheidung von CO_2-Emissionen und die geologische Speicherung dieser. Die Beiträge von Simulation von Großprojekten haben einen wichtigen Aspekt für die Erweiterung des Verständnisses für die auftretenden Migrationsprozessse.

Das Ziel dieser Diplomarbeit ist die bestehenden kommerziellen und nichtkommerziellen Simulationsoftwaren, mit Hilfe einer Kandidatenfeld für große CO_2-Sequestrierung als Simulationsmodell, zu benchmarken. Das Modell beinhaltet die Injektion von Kohlendioxid in den salzhaltigen Aquifer der Johansen Formation. Der 2-Phasen-Prozess wurde mit den Simulationssoftwares Eclipse, IMEX und OPM erstellt. Als Vergleichsparameter dienten die Veränderungen von Wasservolumen und der injizierten Gasvolumen im untersuchten Einsatzgebiet unter Reservoir- und Oberflächenbedingungen, die Abweichungen im Druck- und Sättigungsprofil der beiden Phasen und die Dauer Simulationslaufzeiten.

Der verwendete Benchmark kann in zwei Szenarien unterteilt werden: das erste Szenario beinhaltet ein Modell mit nicht kompressiblen Flüssigkeiten. Indessen betrachtet das zweite Szenario mit verschiedenen Kompressibilitätsgraden. In beiden Fällen wird ein Zweiphasenströmung unter isothermen und nicht mischbar Bedingungen angenommen. Geomechanischen und geochemischen Auswirkungen wurden als vernachlässigbar identifiziert. Die genannten konzeptuellen Anfangsbedingungen werden verwendet um die Möglichkeiten und Limitierungen der Simulationssoftwares zu testen. Die Modelle der Simulationssoftwares beinhalteten identische Corner-point Grid, PVT-Tabellen, relative Permeabilitätskurven, Anfangsbedingungen und Bohrlochproduktivitäseinschränkungen.

Mit Hilfe der Diplomarbeit konnte gezeigt werden, dass die Simulationszeit steigt wenn kompressible Fluide angenommen werden und eine FVM-TPFA, welche bei der Simulationssoftware OPM zum Einsatz kommt, verwendet wird. Mit den kommerziellen Programmen von Eclipse und IMEX wurden kürzere Simulationszeiten erreicht, jedoch ist die Vergleichbarkeit nicht vollständig gegeben, da die Inkompressibilität nicht exakt gleich definiert ist. Weiter Abweichungen entstanden durch die Implementierung der Randbedingungen.

Acknowledgements

I would like to thank my advisor Dr. Julian Mindel (Federal Institute of Technology, Zurich) for mentoring me during my graduate studies and guiding the research that made this thesis possible. It was through his leadership that I found the patience and persistence I needed to overcome the challenges of this research. Thank you!

Secondly, I would like to acknowledge the financial support I was granted via the GeoCCS project by Exploration and Production, OMV as a Graduate Research Fellow. I would also like to say thank you for Professor Gerald Thonhauser and Professor Stephan Matthäi for all the equipment and technical support provided by the Chair of Reservoir Engineering at the Institute of Petroleum Engineering, University of Leoben.

Another important person in the realization of this essay is Roman Manasipov (PhD student, University of Leoben), who had the mathematical vision and programming knowledge that inspired a large portion of my research. Thank you for your help in needed time and patient debugging of OPM for hours.

Other people I would like to thank are Shahin Kord and Siroos Azizmohammadi (University of Leoben) for taking an interest in my research, answering all my random questions and always providing useful information.

I would also like to thank my friends and family for listening to my outburst of happiness in successful time and encouraging me in more difficult moments over the past 2 years.

Table of contents

1. Introduction 1
2. Scientific benchmarking 5
   2.1. The most significant benchmark studies in CCS 5
   2.2. On-going processes during CO_2 sequestration 13
   2.3. Fundamental properties of two-phase filtration 15
   2.4. Mathematical model of H^2 process 19
3. Numerical methods 25
   3.1. Finite difference method 25
   3.2. Finite volume method and the two point flux approximation 26
   3.3. Discretization of transient problem 30
4. The applied simulators 31
   4.1. Eclipse 31
   4.2. Computer Modelling Group 33
   4.3. Open Porous Media 35
5. Model description of the Johansen benchmark 38
   5.1. Model domain 38
   5.2. Fluid and rock models 40
   5.3. Boundary and initial conditions 42
   5.4. Well model 43
6. Results 45
   6.1. Capabilities and limits of the applied simulators 45
   6.2. Volume changes 46
   6.3. Saturation profiles 49
   6.4. Pressure profiles 59
   6.5. Computational time 69
7. Conclusion 71

References 73

Appendix 76

   Appendix A 76
   Appendix B 80
   Appendix C 84

List of Figures

Figure 1.1: Average per capita CO2 emission until 2013 1
Figure 1.2: Possible ways to store CO2 underground 2
Figure 1.3: Aquifer distributions around the world 3
Figure 2.1: Benchmarking strategies 5
Figure 2.2: Combined effect of JTC and VHD in layer B14a 7
Figure 2.3: Relevant precipitation and dissolution at equilibrium 8
Figure 2.4: Leakage scenario of the Stuttgart case 9
Figure 2.5: Computed leakage rates in the two Stuttgart problems 10
Figure 2.6: Geometry model of the Altmark case 11
Figure 2.7: Heat loss calculated in the Altmark case 11
Figure 2.8: CO_2 saturation profile after 20 years in the Svalbard case 12
Figure 2.9: Johansen formation geometry proposed by Class et al. (2008) 13
Figure 2.10: Dominant processes in CO2 injection 14
Figure 2.11: Definition of contact angle 17
Figure 2.12: Typical water wet relative permeability curves 18
Figure 2.13: Well representation as a source/sink term 22
Figure 2.14: Well representation by analytical formula 23
Figure 3.1: Spatial discretization for 3D finite difference approximation 25
Figure 3.2: 2D finite volume cell at time level *n* 28
Figure 3.3: Orthogonal neighboring cells in two point flux approximation 29
Figure 5.1: NPD5 structure as part of the full field model 38
Figure 5.2: Corner point grid arrangement of two adjacent cells 39
Figure 5.3: NPD5 sector model of Johansen formation (depth is in meters) 40
Figure 5.4: Initial pressure distribution in layer 6 43
Figure 5.5: Visualization of the wells 44
Figure 6.1: Cumulative CO_2 injection in the incompressible model 46
Figure 6.2: Cumulative brine production in the incompressible case 47
Figure 6.3: Cumulative CO_2 injection in the compressible model 48
Figure 6.4: Cumulative brine production in the compressible model 49
Figure 6.5: Gas saturation in the in the incompressible case at t=5 years 50
Figure 6.6: Gas saturation in the in the incompressible case at t=10 years 51
Figure 6.7: Gas saturation in the in the incompressible case at t=15 years 52
Figure 6.8: Gas saturation in the in the incompressible case at t=20 years 53
Figure 6.9: Gas saturation in the compressible case at t=5 years 55
Figure 6.10: Gas saturation in the compressible case at t=10 years 56
Figure 6.11: Gas saturation in the compressible case at t=15 years 57
Figure 6.12: Gas saturation in the compressible case at t=20 years 58
Figure 6.13: Pressure profile in the in the incompressible case at t=5 years 60
Figure 6.14: Pressure profile in the in the incompressible case at t=10 years 61
Figure 6.15: Pressure profile in the in the incompressible case at t=15 years 62
Figure 6.16: Pressure profile in the in the incompressible case at t=20 years 63
Figure 6.17: Pressure profile in the compressible case at t=5 years 65
Figure 6.18: Pressure profile in the compressible case at t=10 years 66
Figure 6.19: Pressure profile in the compressible case at t=15 years 67
Figure 6.20: Pressure profile in the compressible case at t=20 years 68

List of Tables

Table 1.1: Operating large scale projects worldwide in 2014 3
Table 2.1: Problem types corresponding to THMC processes 15
Table 2.2: THMC classification of the site specific benchmarks 15
Table 5.1: Fluid properties for incompressible case 41
Table 5.2: Fluid properties for compressible case 41
Table 5.3: Relative permeability data 42
Table 5.4: Well model definition (location and constraint) 43
Table 6.1: Pressure ranges in the incompressible scenario 64
Table 6.2: Pressure ranges in the compressible scenario 69
Table 6.3: Computational time of the simulations 69
Table 7.1: Features of numerical simulators 71

Notation

∇	Laplace operator
∇p	Pressure gradient
∇p_α	Pressure gradient of phase α
A_Γ	Area of common interface Γ
B_α	Formation volume factor of phase α
c_K	Center coordinate of block K
c_L	Center coordinate of block L
CNV_α	Convergence error of phase α
c_R	Rock compressibility
c_α	Fluid compressibility of phase α
$c_{\mu\alpha}$	Viscosibility of phase α
D	Euclidean distance
f_{geo}	Geometrical factor
f_{well}	Well factor
G	Gravitational acceleration
h	Block thickness
H	Flux term
k	Absolute permeability
$k_{r\alpha}$	Relative permeability of phase α
k_x	Absolute permeability in direction x
k_y	Absolute permeability in direction y
MB_α	Material balance error of phase α
m_α	Mass of phase α
$\hat{n}$	Outward face normal
p	Pressure
p_r	Reservoir pressure
p_{sc}	Standard condition pressure
p_{wf}	Bottom hole well flow pressure
p_{wh}	Well head pressure
p_α	Pressure of phase α
$Q_{block,\alpha}$	Net influx of phase α into the block
$Q_{mass,\alpha}$	Mass source term of phase α
$Q_{well,\alpha}$	Net influx of phase α into the well
r_e	Effective radius
r_{wb}	Well bore radius
R_g	Residual of gas phase
R_s	Dissolved gas-oil ratio
R_w	Residual of water phase
R_α	Residual of phase α
s	Skin factor
t	Time
T	Temperature
T_r	Reservoir temperature
T_{sc}	Standard condition temperature

T_α	Transmissibility of phase α
U	General continuous function
v_α	Actual velocity of phase α
V_B	Bulk volume
V_P	Pore volume
V_S	Solid rock volume
V_α	Volume of phase α
$V_{\alpha,sc}$	Volume of phase α under standard condition
WI	Well index
z_{bh}	Bottom hole depth
α	Phase
Γ	Common interface of neighboring blocks
δ	Dirac function
θ	Contact angle
Λ	Linear operator
λ_Γ	Cell mobility across common interface Γ
μ	Dynamic viscosity
μ_α	Dynamic viscosity of phase α
ρ_α	Density of phase α
σ_{12}	Interfacial tension between Fluid 1 and Fluid 2
σ_{s1}	Surface tension between solid and Fluid 1
σ_{s2}	Surface tension between solid and Fluid 2
ϕ	Porosity
Φ	Potential
Ω	Model domain

Subscript

i	Node index in direction x
j	Node index in direction y
k	Node index in direction z
m	Block index
v	Perforated block index
α	Phase
g	Gas phase
w	Water phase
O	Oil phase

Superscript

n	Previous time step
n+1	Current time step

1. Introduction

The increase of atmospheric greenhouse gas, particularly carbon-dioxide (CO_2) is one of the main causes of the climatic changes such as the inordinate weather, the melting of the polar ice and consequent rise in sea-level. Therefore, capture and geologic storage of CO_2 has been studied in the last two decades in order to decrease anthropogenic CO_2 emissions into the atmosphere as it is a potential, short-term solution to mitigate these climate changes.

The variations in CO_2 emanation worldwide and in the four countries with the highest emission rate per capita in the time period from 1960 to 2013 are illustrated in Figure 1.1. The graph indicates that since 1960 the largest emitter has been the USA. In the last decade the CO_2 emission has been dramatically increasing in China, while during this time period the discharge rate has decreased in the USA.

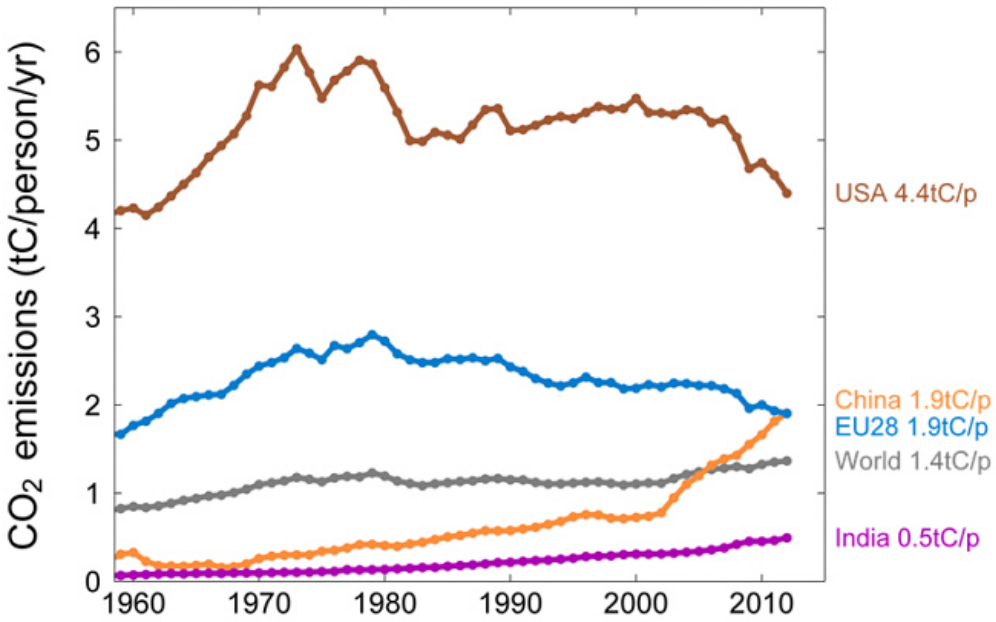

Figure 1.1: Average per capita CO2 emission until 2013

(Le Quéré, et al., 2013)

One way to reduce CO_2 emissions produced by burning of natural gas, crude oil and coal would be to return them back to the ground in the form of CO_2, thus creating a closed loop in the energy production system. There are four principle ways to store CO_2 underground as presented in Figure 1.2: in depleted hydrocarbon fields, in operating hydrocarbon fields as a form of enhanced recovery method, in saline aquifers, and in coal seams that cannot be mined – due to economic or technologic limits.

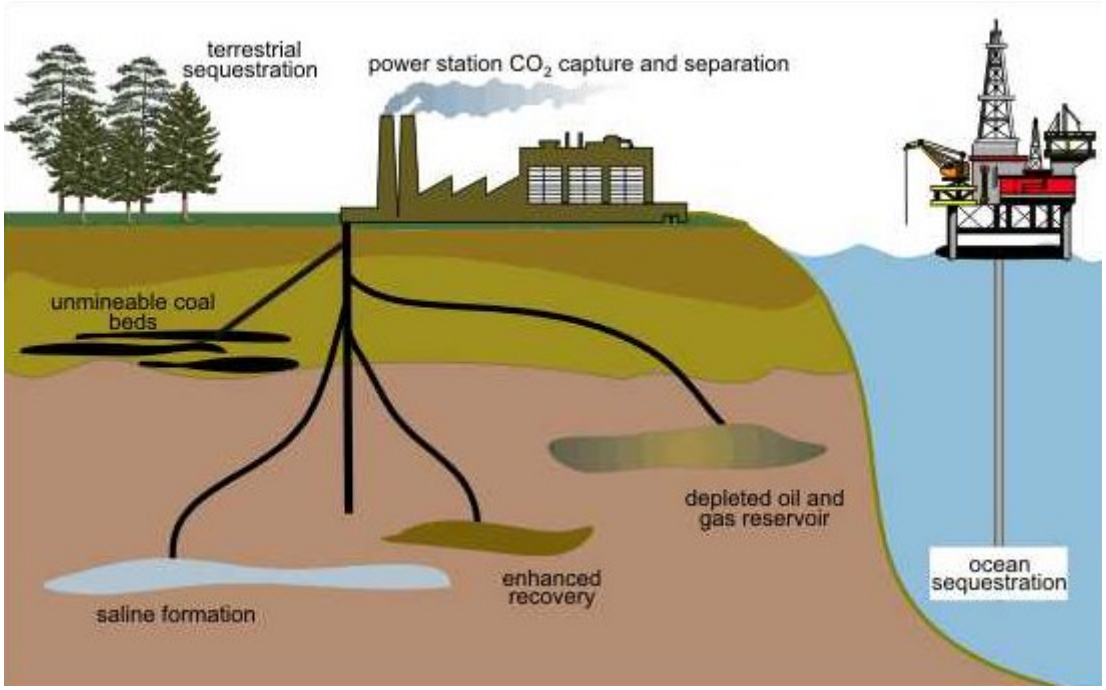

Figure 1.2: Possible ways to store CO2 underground

(Osman, 2007)

Injecting into saline formations in sedimentary basins is one of the most promising methods of carbon capture and storage (further on: CCS) for the long-term sequestration of CO_2 as such basins are present all over the world. Figure 1.3 illustrates the distribution of aquifers around the globe. Major basins contain profuse, relatively easily accessible groundwater. More complex basins are composed of several aquifers isolated by impermeable rock. Local and shallow aquifers provide limited amount of water.

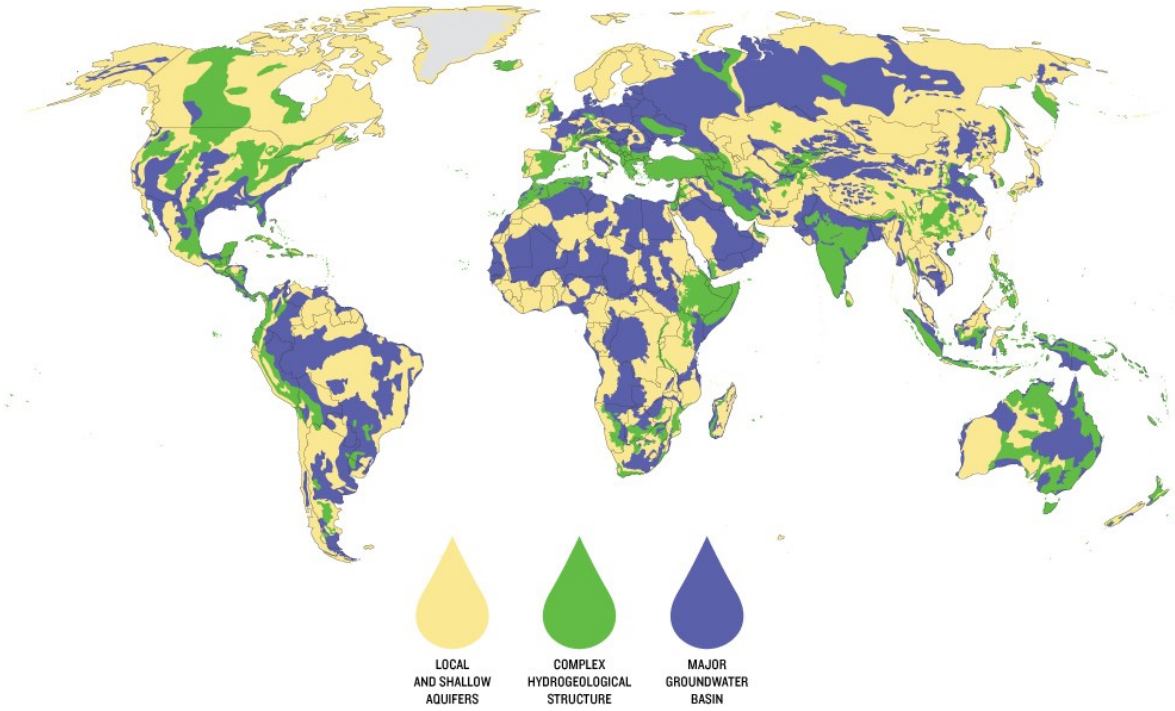

Figure 1.3: Aquifer distributions around the world

(Barnett, 2015)

Aquifers generally have a high capacity to store CO_2. There are currently 12 large scale projects in operation related to CCS, based on the Global CCS Report (Report, 2014). These are listed in Table 1.1.

Table 1.1: Operating large scale projects worldwide in 2014

Project name	Country	Date	Capacity [Mt/a]
Century Plant	USA	2010	8.4
Shute Creek Gas Processing Facility	USA	1986	7.0
Great Plains Synfuel Plant and Weyburn-Midale Project	Canada	2000	3.0
Val Verde Natural Gas Plant	USA	1972	1.3
Air Products Steam Methane Reformer EOR Project	USA	2013	1.0
Coffeeville Gasification Plant	USA	2013	1.0
Sleipner CO_2 Injection	Norway	1996	0.9
Lost Cabin Gas Plant	USA	2013	0.8-1.0
Petrobas Lula Oil Field CCS Project	Brazil	2013	0.7
Enid Fertilizer CO_2-EOR Project	USA	1982	0.7
Snohvit CO_2 Injection	Norway	2008	0.6-0.8
In Salah CO_2 Storage	Algeria	2004	0.5

(Global CCS Institute, 2014)

An important aspect of understanding CO_2 migration in large-scale projects is the simulation of the processes occurring in such reservoir. Analytical solutions are often hard to achieve when using complex models such as real-site formations. Such reservoir software have been developed in the industry that focus on simulating these reservoir processes. Benchmarking is a scientific tool used for software code verification and model validation. My aim in this work is to create a benchmark study using a candidate site for large scale CO_2 sequestration. The concept of the model is the injection of CO_2 with constant rate into a well-documented saline aquifer, the Johansen formation (offshore of the south-western coast of Norway), over 50 years. The two-phase fluid flow (CO_2 and brine) is considered isothermal and immiscible. CO_2, that is gaseous under surface conditions and is injected under supercritical conditions, is considered slightly compressible, while brine is incompressible. Geo-mechanical and chemical effects are neglected in the modelling. For the simulation of this process, three different simulator software were used: IMEX (Computer Modelling Group Ltd., Canada), Eclipse (Schlumberger Limited, USA) and OPM (Open Porous Media Initiative). Among the simulation results I compared the following properties:

- Volumes: change of water volume and cumulative injected CO_2 volume in the modeled field under surface conditions
- Pressure distribution
- CO_2 saturation profile
- Computational time

In my thesis different benchmarking approaches are introduced at first, followed by short descriptions of benchmarking projects in the field of CO_2 storage that I considered important to emphasize. In section 2.2 the processes occurring during and after injection of CO_2 are presented, while in section 2.3 the fundamental properties in reservoir engineering are introduced followed up by the description of the conceptual model of the proposed benchmark in terms of governing equations and constituting laws. In section 3, different numerical methods are described that are used by the software introduced briefly in in section 4. The simulation model is defined in detail in section 5 followed by demonstration and comparison of the simulation results in section 6.

2. Scientific benchmarking

Benchmarks can be generally defined as scientific tools used to confirm the suitability and/or accuracy of algorithms implemented in the software used for modelling. Benchmarking involves running simulation test cases that may be either process- or site-related. For CCS simulation software, the aim of process-related benchmarks is to determine the capability of the simulator with respect to coupled mechanisms (e.g. thermos-hydro-mechanical-chemical or THMC), while site specific cases investigate different geological model settings for reservoirs where CO_2 is planned to be stored.

A proposed benchmark may be either a curiosity-driven study which analyses the importance of process coupling and selection of constitutive laws, or a data driven case when the test simulations are based on real sites which is the case in this thesis. (Kolditz, et al., 2012) suggested the following benchmarking strategies (Figure 2.1) to be applied for the previously introduced benchmarking approaches:

- Process based strategy: numerical analysis of the occurring phenomena related to CCS simulated separately and coupled in different manners with increasing complexity
- Thermodynamic based strategy: describe more complicated fluid behavior by applying various constitutive relations
- Scenario based strategy: develop site-specific test cases modelling typical conditions in distinct geological settings. (Kolditz, et al., 2012)

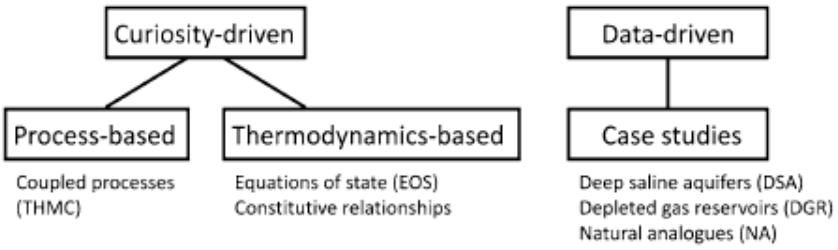

Figure 2.1: Benchmarking strategies

(Kolditz, et al., 2012)

2.1. The most significant benchmark studies in CCS

Several CCS-related benchmark cases have been defined by modelers in scientific articles. The comparison studies found in the literature which I considered important to emphasize and introduce will be presented focusing on the proposed strategies. As the subject of my thesis is a site specific approach, case studies

related to real geological formations (especially saline aquifers) are emphasized. The selected research models are:

- Process based examples:
    - Thermal effects during CO_2 injection (Singh, et al., 2012)
    - Geochemical effects induced by CO_2 (De Lucia, et al., 2012)
- Thermodynamic based example:
    - Thermal equation of states for CO_2 (Böttcher, et al., 2012)
- Data driven examples:
    - Stuttgart case: (Ebigbo, et al., 2007), (Celia, et al., 2005), (Humez, et al., 2011)
    - Altmark case: (Singh, et al., 2012), (Beyer, et al., 2012), (Hou, et al., 2012)
    - Svalbard case: (Nordbotten & Dahle, 2011), (Kolditz, et al., 2012)
    - Johansen case: (Wei & Saaf, 2009), (Class, et al., 2009), (Eigestad, et al., 2009)

Thermal effects during CO_2 injection

In this work, non-isothermal effects during CO_2 injection were examined focusing on the Joule-Thompson cooling and viscous heat dissipation effects on temperature change in the reservoir during CO_2 injection. Numerical solutions (using the Altmark conceptual model) were independently calculated using two software tools: OpenGeoSys (OGS) and FeFlow. OGS differs from FeFlow in the capability of representing multi-component effects on the thermal recovery behavior after injection is completed. The shut-in temperature profiles (temperature versus distance from well center) along the injector were compared and results showed that reservoir temperature varies significantly due to repressurization: in the injected layer, where viscous heat dissipated, the formation is cooled by the Joule-Thompson effect (see Figure 2.2 where B14a is the most permeable layer where CO_2 is injected). The shut-in pressure profiles from the two simulators were also compared, which verified that the multi-componential effects modelled by OGS produced stronger thermal recovery in the injected layers. (Singh, et al., 2012)

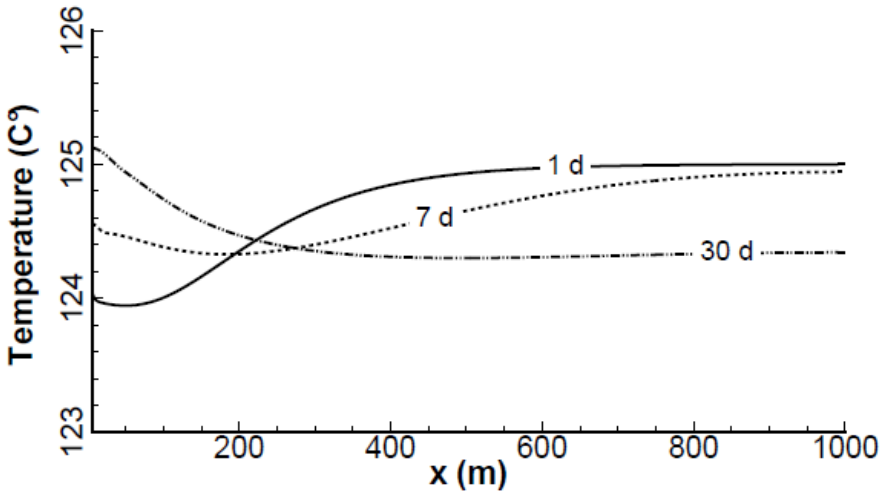

Figure 2.2: Combined effect of JTC and VHD in layer B14a
(Singh, et al., 2012)

Geochemical effects induced by CO_2

This example involves modelling fluid-rock interaction induced by CO_2 to assess the reliability of thermodynamic data associated with deep saline aquifers. The high salinity and high temperature in the reservoir at and below 3000 meter depth may push the validity limits of thermodynamic databases generally used for geochemical modelling (such as Debye-Hückel activity model). This benchmark addressed this validation by using a simplified geochemical model which is consistent with the fluid composition and mineralogical rock structure of Altensalzwedel compartment (part of Altmark gas field). The simulated reactions due to CO_2 injection under assumed thermodynamic equilibrium resulted in a moderate reactivity of the reservoir with hematite dissolution and anhydrate cementation. The precipitation of calcite and siderite compensated the decrease in mineral volume. Figure 2.3 shows the mineral alteration in moll/liter rock due to injection of CO_2 calculated using the LLNL (Lawrence Livermore National Laboratory), Quintessa and GRS (Gesellschaft für Anlagen und Reaktorsicherheit) database. The LLNL database was generated based on the Debye-Hückel formulation that provides data for a large number of minerals and aqueous components over a range of temperature from 0-300°C and thus is often adopted for CO_2 applications. Quintessa and GRS are databases which were produced based on the theoretical model developed by Pitzer that consider specific ion interactions as well, while the Debye-Hückel model only captures redox reactions. However the databases based on the Pitzer model were not consistently parametrized for temperatures higher than 25°C. Results show that even if the Pitzer model is inconsistent, the activity model of Pitzer has to be applied as simulations

based on the Debye-Hückel activity model lead to severe discrepancy from experimental data used for comparison. As proved in Figure 2.3 the dissolution of anhydrite and hematite, and the precipitation of K-Feldspar, Calcite and Siderite were not captured by the simulation using the LLNL database. (De Lucia, et al., 2012)

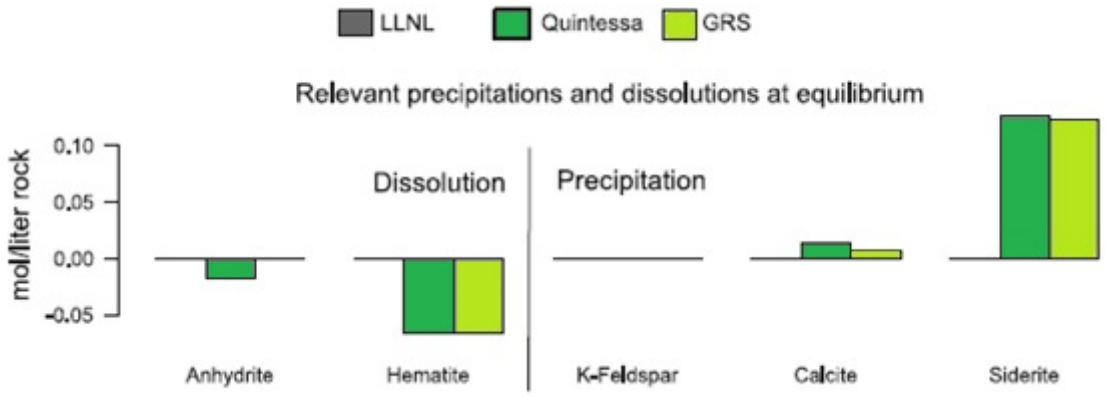

Figure 2.3: Relevant precipitation and dissolution at equilibrium
(De Lucia, et al., 2012)

Thermal equation of states for CO_2

This topic was suggested to confront the inaccuracy of the density which is a function of pressure and temperature that can cause significant errors in fluid property correlations employed for determining CO_2 parameters such as viscosity, thermal conductivity and heat capacity. Three equation of states were analyzed: the simpler cubic equation by Peng and Robinson was contrasted to the more complex equation by Duan et al. as well as a fundamental equation by Span and Wagner. The Peng-Robinson formula handles single component system conveniently by adjusting the two fitting parameters, meanwhile the other two (Duan et al. and Span-Wagner) had to be tuned to individual substances by several fitting parameters. The researchers also studied how the different presented equations of state affect the results of numerical simulations related to CO_2 sequestration: the difference among the particular results show that even small differences in the density function causes considerably varying results of identical simulation results. (Böttcher, et al., 2012)

The Stuttgart case

This benchmark study was developed by researchers of Stuttgart University. CO_2 is injected into a deeper aquifer and allowed to migrate. Upon reaching a “leaky” well the gas rises up to a shallower aquifer (see Figure 2.4). The goal in this case is to determine the leakage rate which depends on the pressure build up in the deeper aquifer. (Ebigbo, et al., 2007) created two subcases in this benchmark problem: in

the first case the lower aquifer is considered to be very deep and among other simplifications the most important one is that the fluid properties are constant; however in the second more complex case, the aquifer depth is shallower and the fluid properties are dependent on the aquifer conditions (temperature, pressure, brine salinity and CO_2 mass fraction in brine).

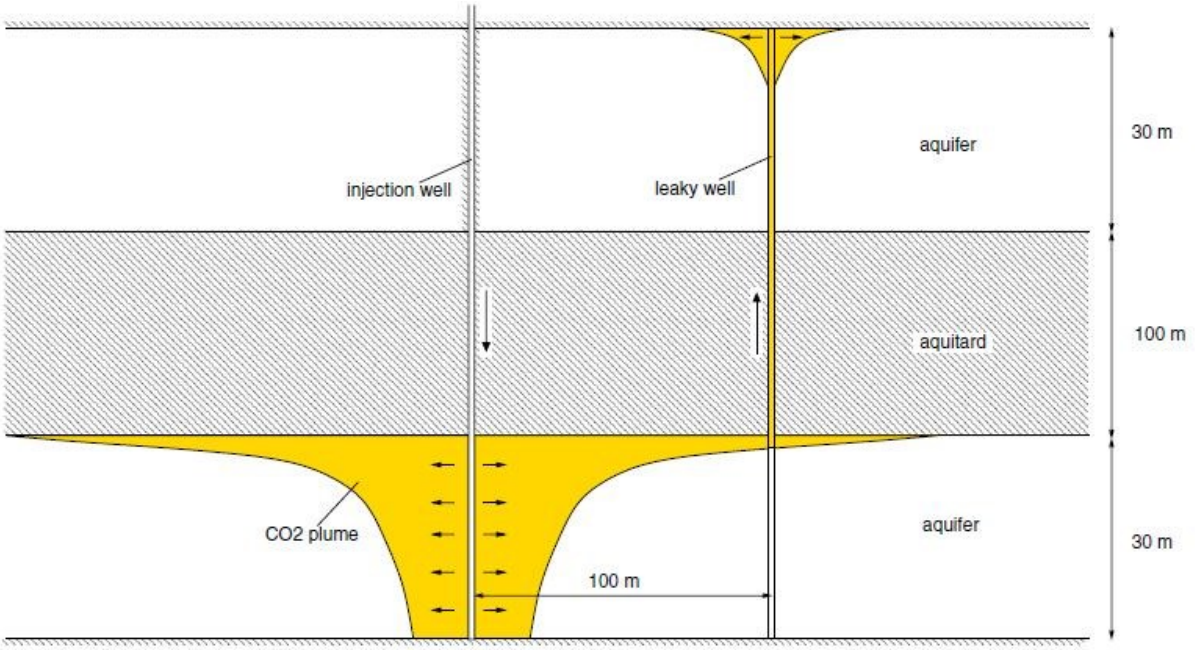

Figure 2.4: Leakage scenario of the Stuttgart case
(Ebigbo, et al., 2007)

In this benchmark the ratio of CO_2 leakage to injected CO_2 was compared by 13 different simulations in the simplified case and by 9 simulations when the properties depend on the aquifer conditions illustrated in Figure 2.5.

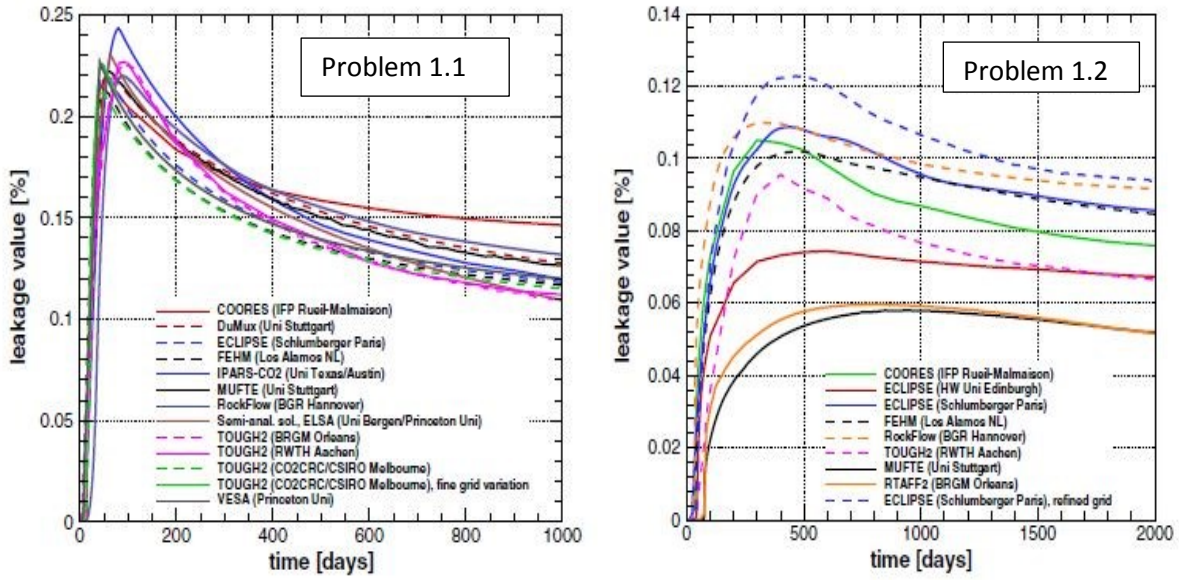

Figure 2.5: Computed leakage rates in the two Stuttgart problems
(Ebigbo, et al., 2007)

A fully analytical, as well as a semi-analytical solution for this problem. Readers with interest in these solutions are referred to (Nordbotten, et al., 2005b) and (Nordbotten, et al., 2005a).

Altmark case study

A multi-layered caprock-reservoir model is considered for this benchmark case, where the entire domain is composed of four different rock types (19 layers are assumed – Figure 2.6). This case study was the continuation of the benchmark study examining geochemical effects related to CO_2 injection. The reservoir was considered to be initially filled with methane and nitrogen then CO_2 injection was introduced.

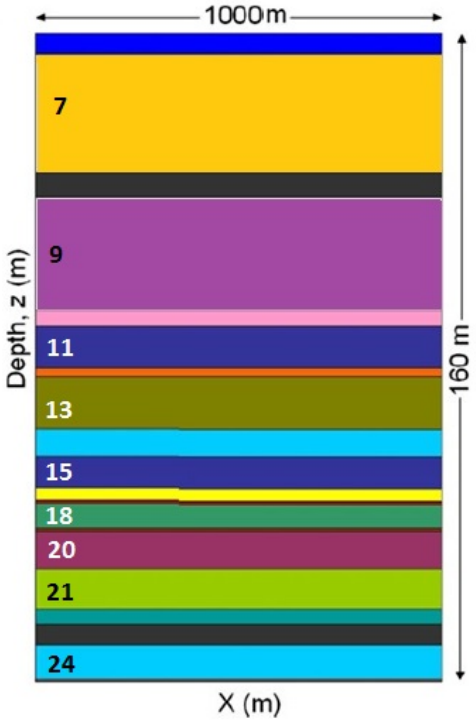

No.	Rock type	z_p (m)
6	Sandstone	5
7	Anhydrite	29
8	Sandstone	6
9	Siltstone	28
10	Sandstone	4
11	Siltstone	11
12	Sandstone	2
13	Siltstone	12
14	Sandstone	6
15	Siltstone	8
16	Sandstone	3
17	Siltstone	1
18	Sandstone	6
19	Siltstone	1
20	Sandstone	9
21	Claystone	10
22	Sandstone	4
23	Claystone	6
24	Sandstone	9

Figure 2.6: Geometry model of the Altmark case
(Singh, et al., 2012)

The aim was to model non-isothermal gas flow through different porous layers under axisymmetric conditions: mass transport, concentration distribution of each species and heat transfer were calculated. Heat loss was investigated through two different scenarios: in the first case the heat provided by the solid matrix is taken into account, whereas in the second case this heat is neglected. The numerical results produced by the simulator OpenGeoSys agree well with the calculated analytical solutions as presented in Figure 2.7 which confirms the capability of the simulation code. (Singh, et al., 2012)

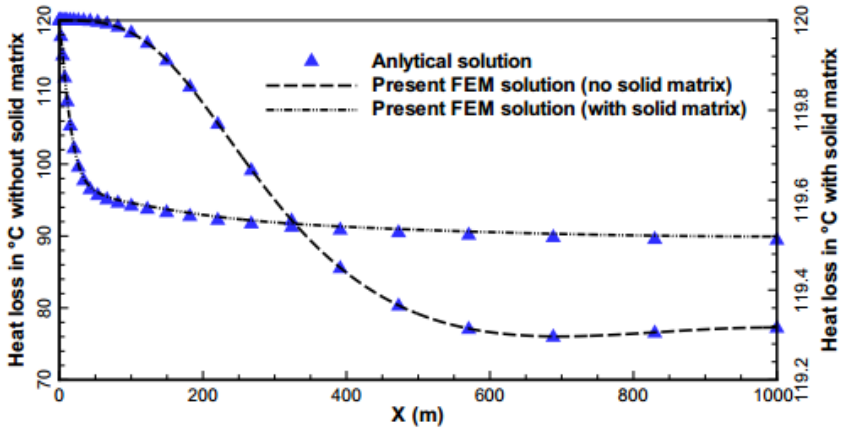

Figure 2.7: Heat loss calculated in the Altmark case
(Singh, et al., 2012)

Svalbard case study

The benchmark properties are motivated by a typical sedimentary formation: the aquifer bounded by parallel impermeable confining formations has a dip of 1% above and below. A horizontal well with a length of 1 km, perpendicular to the dip, is injecting CO_2 at the bottom impermeable boundary of the formation. The formation is considered homogeneous, and the solid rock is incompressible, with no fractures, while hysteresis is taken into account in the relative permeability curve. Typical PVT properties are assumed for pure components of CO_2 and pure water. Initially water fills the reservoir. The model defines a modeling time period of 20 years. The purpose of this problem is to model the fate of the CO_2 plume in the reservoir (see Figure 2.8: saturation profile of CO_2 after 20 years of injection) and assess of upscaling and modeling applicability for CCS. (Nordbotten & Dahle, 2011)

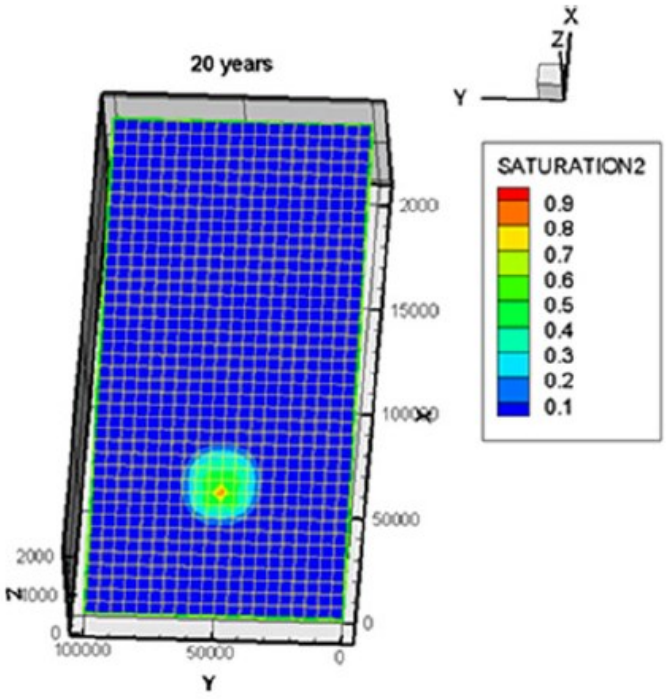

Figure 2.8: CO_2 saturation profile after 20 years in the Svalbard case
(Nordbotten & Dahle, 2011)

Johansen formation

The Johansen case study was formulated by (Class, et al., 2009) to estimate CO_2 effective capacity in a heterogeneous geological formation. The overestimation of the storage potential could lead to leakage especially in geology containing significant fault system such as the Johansen formation (see Figure 2.9), while an underestimation will result in waste of injection capabilities. To simulate CO_2

spreading accurately, the appropriate processes (such as thermal, gravity, capillary and hysteresis effects) must be captured by the model. (Class, et al., 2009) introduced two subcases: first case neglects hysteresis effects, while the second case considers the hysteresis of CO_2-brine relative permeability-saturation relationship. Results showed that hysteresis leads to increased residual trapping and slower spreading.

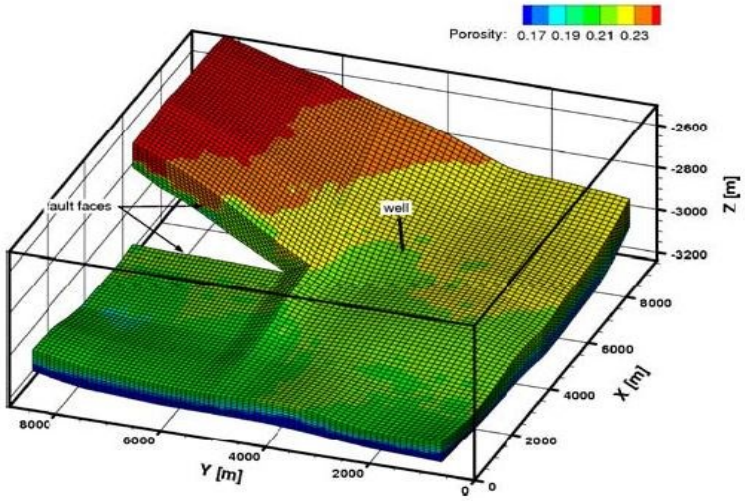

Figure 2.9: Johansen formation geometry proposed by Class et al. (2008)
(Class, et al., 2009)

(Eigestad, et al., 2009) discussed further this benchmark: they created a complete dataset for the Johansen formation considering a sensitivity analysis with respect to different vertical grid refinements, permeability/transmissibility data and relative permeability curves as part of the MatMoRA project (sponsored by Sintef). In this work the model geometry called NPD5 they created was used. For the original data the reader is referred to (Dahle, 2009)

2.2. On-going processes during CO_2 sequestration

During CO_2 injection physical and chemical processes occur that a model must account for and therefore any benchmark problem should aim at introducing a model for them. These processes and trapping mechanisms vary significantly, particularly after injection. The dominant processes during and after the different phases of injection are illustrated in Figure 2.10.

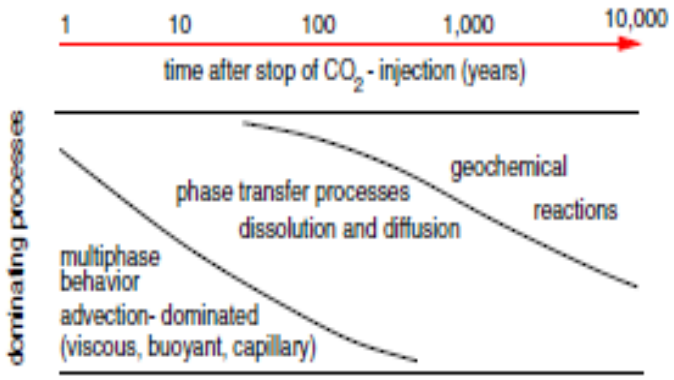

Figure 2.10: Dominant processes in CO2 injection
(Class, et al., 2009)

During injection and in the first phase after injection, advective multi-phase processes dominate the CO_2 spreading driven by viscous forces and buoyancy. After some time, fluid flow becomes secondary to the effect of dissolution of CO_2 into the brine. Over hundreds of years the injected CO_2 dissolves completely or generates significant mineralization due to geochemical processes like the precipitation of calcite. Other short-term chemical reactions are the production of carbonic acids from water and CO_2 or biological and organic effects in the near wellbore region. (Class, et al., 2009)

One possible classification of the processes related to CO_2 sequestration that was created by modelers is the THMC approach suggested by (Kolditz, et al., 2012):

- T: thermal processes (e.g. non-isothermal flow)
- H: hydrologic processes (e.g. single-phase flow or multiphase flow)
- M: mechanical processes (e.g. consolidation)
- C: chemical processes (e.g. compositional flow, or reactive transport)

Some problem types described by THMC classification is presented in Table 2.1.

Table 2.1: Problem types corresponding to THMC processes

Problem type	Acronym
Compressible flow	H
Two-phase flow	H^2
Unsaturated consolidation	HM
Two-phase flow consolidation	H^2M
Thermo-mechanics	TM
Non-isothermal compressible flow	TH
Non-isothermal two-phase flow	TH^2
Non-isothermal single-phase consolidation	THM
Non-isothermal two-phase flow consolidation	TH^2M
Non-isothermal compositional flow	THC^n
Reactive transport	HC^n
Compositional gas flow (natural analogues)	HC

(Kolditz, et al., 2012)

The site specific benchmark cases introduced in section 2.1 is described by the THMC approach in Table 2.2.

Table 2.2: THMC classification of the site specific benchmarks

Benchmark title	Dimension	THMC class
Stuttgart case	2D	H^2
Altmark case	2D radial	THC^3
Svalbard case	3D	H^2M
Johansen case	3D	THC^2

Although the previously introduced benchmark studies prove the importance of modeling thermal effects, I chose to neglect temperature effects to simplify the proposed model setup. Geo-mechanical effects are also not considered in the scope of my thesis. As illustrated in Figure 2.10, with a simulation time of 20 years, geochemical effects are negligible. Therefore I have chosen to model two-phase fluid flow under isothermal and immiscible assumptions. Using the introduced THMC classification from Table 2.1, my considerations qualify as an H^2 process.

2.3. Fundamental properties of two-phase filtration

In this section all the important properties are defined that are necessary to describe two-phase fluid flow in a porous medium.

Petro-physical parameters that describe the reservoir rock containing the examined fluids are the following properties:

- Porosity
- Rock compressibility
- Wettability
- Permeability

- Relative permeability curves

The features that are crucial to define a fluid system composed of two immiscible phase are listed below:

- Density under surface condition
- Formation volume factor at given pressure points
- Fluid compressibility (in case of compressible fluids)
- Viscosity

Porosity

Porosity of a solid medium is the ratio of the pore volume with respect to the total bulk volume of the medium which is expressed as:

$$\phi = \frac{V_P}{V_B} = \frac{V_B - V_S}{V_B} \tag{2.1}$$

Two kinds of porosity can be distinguished: total porosity considers every pore present in the medium including isolated pores, whereas effective porosity is calculated taking into account only those interconnected pores which are open to fluid transport. The storage capacity always depends on effective porosity. From this point, when porosity is mentioned in the thesis, I always mean effective porosity.

Rock compressibility

The reservoir rock may not be considered as a rigid medium. If the elastic ability of the rock is not negligible then the medium is regarded compressible: due to variance in pressure the pore volume in the rock changes which affects porosity as well. Under isothermal conditions, the rock compressibility is:

$$c_R = \frac{1}{\phi}\left(\frac{\partial \phi}{\partial p}\right)_T \tag{2.2}$$

Wettability

The ability of one fluid in the presence of another fluid to spread on the surface of the rock is called wettability. This ability is measured by the contact angle of the interface between the immiscible phases. The tension appearing on the interface separating two (gaseous or liquid) fluids is called interfacial tension, while surface tension forms on rock-fluid interface. (Heinemann, 2005)

The fluid is considered the wetting phase if the contact angle of the interface between the fluid and the solid surface is less than 90°. In the opposite case, when

the contact angle is more than 90° then the fluid is the non-wetting phase. In Figure 2.11 the wetting phase is Fluid 1, the non-wetting phase is Fluid 2.

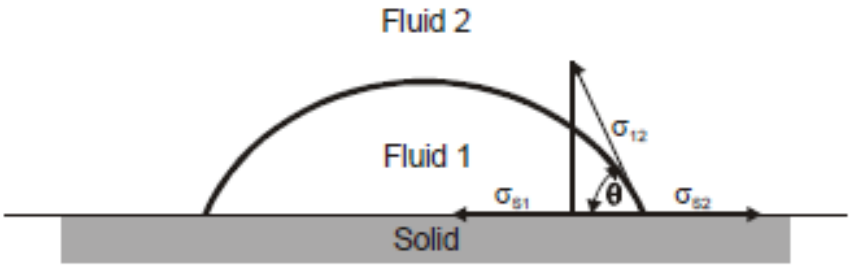

Figure 2.11: Definition of contact angle

(Heinemann, 2005)

Using the surface tensions and interfacial tension developing on all present interfaces (fluid-fluid, fluid-rock), the trigonometric function of the contact angle can be derived as given in Equation (2.3)

$$cos\theta = \frac{\sigma_{s2} - \sigma_{s1}}{\sigma_{12}} \tag{2.3}$$

The contact angle severely affects capillary pressure which is the pressure difference arising at both sides of the interface forming between two immiscible fluids. When the fluid-fluid interface is exactly perpendicular to the rock surface, the capillary pressure is zero. Therefore neglecting capillary effect leads to a contact angle of 90°.

Permeability

Permeability is the ability of a fluid to flow through a unit of cross-section by the cause of a pressure drop. Darcy proved the hypothesis that the pressure drop causing the fluid flow is proportional to the velocity, and this proportionality depends on the permeability of the porous medium and the viscosity of the fluid flowing through the pore system.

$$v = -\frac{k}{\mu}\nabla p \tag{2.4}$$

Equation (2.4) is called the Darcy's Law.

Relative permeability

In case of multi-phase fluid flow, the ability of one of the phases to flow in the presence of other phases is described by relative permeability. Relative permeability

of a phase is the ratio of the effective permeability of the phase, when another phase is also present in the system, to the absolute permeability of the rock.

$$k_{r\alpha} = \frac{k_\alpha(S_\alpha)}{k} \tag{2.5}$$

The effective permeability depends on the degree of saturation - the relative amount of fluid present in the pore with respect to the total pore space – which results in relative permeability being saturation dependent. This relationship is described by the relative permeability curve; a typical relative permeability curve is shown in Figure 2.12 for and two-phase fluid system (oil and water) in a water wet rock.

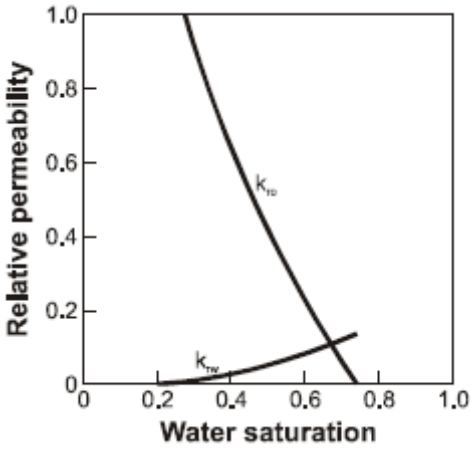

Figure 2.12: Typical water wet relative permeability curves

(Heinemann, 2005)

Density

Density is the relative heaviness of a material measured by its mass per unit volume describing the degree of compaction of the material.

$$\rho_\alpha(p,T) = \frac{m_\alpha}{V_\alpha} \tag{2.6}$$

As the degree of compaction is affected by pressure and temperature, density is always defined under given conditions. Surface conditions in reservoir engineering usually mean standard atmospheric pressure and temperature: 1 atm = 1.013 bar, 15°C = 273.15 K. Standard density is density defined under those conditions.

Formation volume factor

The conversion factor called formation volume factor specifies the change of volume as a result of pressure or temperature variance. Assuming that the

conservation of mass is valid in a system, the formation volume factor characterizes the change in density as well since the mass of the phase does not diversify by a variation of conditions which is proved in Equation (2.7)

$$B_\alpha = \frac{V_\alpha(p_r, T_r)}{V_\alpha(p_{sc}, T_{sc})} = \frac{\frac{m_\alpha}{\rho_\alpha(p_r, T_r)}}{\frac{m_\alpha}{\rho_\alpha(p_{sc}, T_{sc})}} = \frac{\rho_\alpha(p_{sc}, T_{sc})}{\rho_\alpha(p_r, T_r)} \tag{2.7}$$

Fluid compressibility

In case of certain fluids their volumes tend to change as pressure changes under isothermal conditions. When this variance is constant the material is considered low or slightly compressible fluid, otherwise the fluid is considered fully compressible. This constant is the isothermal fluid compressibility:

$$c_\alpha = -\frac{1}{V_\alpha}\left(\frac{dV_\alpha}{dp}\right)_T \tag{2.8}$$

When the conservation of mass applies in the system, the compressibility defined in Equation (2.8) can be obtained by using either density, formation volume factor or compressibility factor in case of gases.

$$c_\alpha = -\frac{1}{\frac{m_\alpha}{\rho_\alpha}}\frac{d\left(\frac{m_\alpha}{\rho_\alpha}\right)}{dp} = \frac{1}{\rho_\alpha}\frac{d\rho_\alpha}{dp} = -\frac{1}{B_\alpha}\frac{dB_\alpha}{dp} \tag{2.9}$$

Viscosity

Viscosity is the resisting ability of a fluid to flow describing the internal friction forming in the fluid caused by the movements of the fluid particles. Viscosity is measured by the force per unit area resisting uniform flow. Viscosity is also a property which depends on the pressure and temperature conditions like compressibility or formation volume factor.

2.4. Mathematical model of H^2 process

This section presents a short overview of the governing equations and constitutive laws describing the physical phenomenon of two immiscible fluids simultaneously flowing through porous media, but the reader is referred to (Heinemann, 2005) and (Heinemann, 2013) for a detailed derivation of the mathematical model.

The basic principle is that the conservation of mass applies to the flow of each phase which is defined by Equation (2.10). This mass balance characterizes the advective transport process in the reservoir.

$$\frac{\partial(\phi\rho_\alpha S_\alpha)}{\partial t} + \nabla \cdot (\rho_\alpha v_\alpha) + Q_{mass,\alpha} = 0 \tag{2.10}$$

The first term of the left hand size in Equation (2.10) is called the transient term that gives the change of mass of phase α over time in a volume, where α = w for wetting phase – brine - and α = g for non-wetting phase – CO_2. The second term is the advection term, which describes the divergence of the mass flux, and the third term is the source term for phase α.

If rock compression may be neglected which results in constant porosity, Equation (2.10) may be simplified, be excluding porosity from the transient term shown in Equation (2.11)

$$\phi\frac{\partial(\rho_\alpha S_\alpha)}{\partial t} + \nabla \cdot (\rho_\alpha v_\alpha) + Q_{mass,\alpha} = 0 \tag{2.11}$$

The conservation of momentum for a fluid characterizes the flow path in a given direction. Applying this equation of momentum balance, also known as the Navier-Stokes equation in a flow system, the fluid pressure at any point of the system can be determined. When the fluid flow is slow enough to disrespect inertia forces, Navier-Stokes equation takes the form given in Equation (2.12).

$$-\nabla \mathrm{p}_\alpha - \frac{\mu_\alpha \phi v_\alpha}{k_\alpha} + \rho_\alpha g = 0 \tag{2.12}$$

Rearranging this equation to volumetric flux (v_α) present in the advective term of the mass balance equation, the extended Darcy's Law is formulated:

$$v_\alpha = -\frac{k k_{r\alpha}}{\mu_\alpha}(\nabla \mathrm{p}_\alpha - \rho_\alpha g) \tag{2.13}$$

This volumetric flux which gives the flow velocity of phase α in a given direction is driven by the pressure gradient of the phase and the gravitational force projected in the assumed direction.

Knowing that only two phases occupy the pore space a constitutive law may be formulated declaring that the sum of the phase saturations must total to unity:

$$S_w + S_g = 1$$

(2.14)

The equation describing the diffusion processes in the reservoir (commonly known as the pressure equation) is derived by inserting the extended Darcy's Law into the mass balance equation and summing the resulting equation for both phases (in order to exclude phase saturation terms). As capillary effect is neglected, the pressure equation for two-phase slightly compressible fluid flow takes the form of:

$$\phi c_\alpha \frac{\partial p}{\partial t} - \nabla \cdot [\frac{k_\alpha}{\mu_\alpha} (\nabla p - \rho_\alpha g)] + \frac{Q_{mass,\alpha}}{\rho_\alpha} = 0$$

(2.15)

Equation (2.10) may be simplified when the fluids are considered incompressible and rock compression is negligible. These conditions lead to constant density and porosity and these properties can be excluded from the time derivative term as given in Equation (2.16).

$$\phi \frac{\partial S_\alpha}{\partial t} + \nabla \cdot v_\alpha + \frac{Q_{mass,\alpha}}{\rho_\alpha} = 0$$

(2.16)

To provide solution to a partial differential problem, boundary conditions must be defined. A closed boundary condition means that no fluid is allowed to enter or leave through the surface of the boundary. When fluid movement across the boundary surface is allowed we speak of open boundary condition. Two main types of boundary conditions exist:

- A Dirichlet boundary condition defines the value of the variable (pressure or saturation is imposed) at the boundary. Normally, specifying such a condition will allow fluid to flow through a boundary with this condition specified for pressure. How much fluid and in which direction it will flow depends on the interior conditions. Incoming flux will normally require that a saturation Dirichlet condition is also defined at the boundary.
- When the gradient of the variable is defined at the boundary in the direction normal to the boundary surface, then a Neumann boundary condition is asserted. Such a condition is not normally specified for saturation but for pressure. Specifying an outward pressure gradient

essentially results in an incoming flux. Such a situation requires the definition of a Dirichlet value for saturation (i.e. to specify which fluid is coming in).

In case of transient problems the initial state of the unknown variables must be declared which will yield a unique solution for the problem. Equation (2.10) defines a set of partial differential equations with a transient term for which an initial condition has to be provided (for saturation and pressure).

When wells are operated in a field they must be accounted for the reservoir simulation as well. The inclusion of wells into the governing equations may occur in two different ways:

- As a source or sink term depending on the operation mode of the wells: producing wells are sink terms, while injectors are considered sources. Only those grid cells will have a source or sink term which are connected to a well and this connection is an open connection (grid blocks at which the well is perforated). The visualization of this well implementation strategy is represented in Figure 2.13.

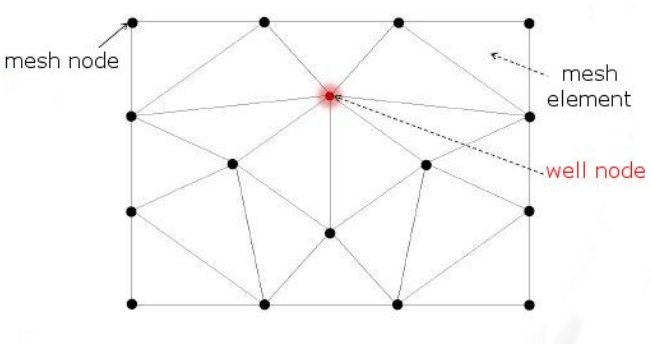

Figure 2.13: Well representation as a source/sink term

- As a Neumann or Dirichlet boundary condition applied on a small circle (when the problem is 2D) surrounding the well (see Figure 2.14). These circles are enveloped with a fine grid which takes the constitution of the well into account. Since wells have a generally smaller scale than a discretized reservoir, defining an analytical model is the first step which will estimate the pressure changes inside the grid block containing the well. This analytical formula is then included in the governing equation applied on all the nodes of this cell.

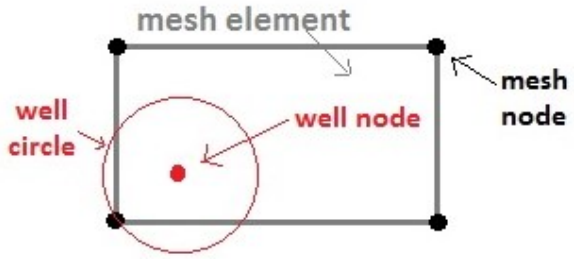

Figure 2.14: Well representation by analytical formula

In a grid block associated with a well, one of two variables may be specified:

1) Bottom hole pressure of the well,
2) Flow rate either at the well head under surface condition or at the bottom of the well under reservoir condition,

The analytical formula suggested in the second well modelling option previously described is determined in Equation (2.17). This equation is valid for a well which penetrates several grid layers and multi-phase fluids flow through the well. (Chen & Zhang, 2009)

$$Q_{mass,\alpha} = \sum_{\nu} \frac{2\pi h_\nu \sqrt{k_{x,\nu} k_{y,\nu}}}{ln\left(\frac{r_{e,\nu}}{r_{wb,\nu}}\right) + s_\nu} \frac{\rho_{\alpha,\nu} k_{r\alpha,\nu}}{\mu_{\alpha,\nu}} \left[p_{wf} - p_{\alpha,\nu} - \rho_{\alpha,\nu} g(z_{bh} - z_\nu)\delta(x - x_\nu)\right] \tag{2.17}$$

Grouping the constant properties in Equation (2.17), the well index is introduced:

$$WI_\nu = \frac{2\pi h_\nu \sqrt{k_{x,\nu} k_{y,\nu}}}{ln\left(\frac{r_{e,\nu}}{r_{wb,\nu}}\right) + s_\nu} \tag{2.18}$$

Including the well index into Equation (2.17):

$$Q_{mass,\alpha} = \sum_{\nu} WI^\nu \frac{\rho_{\alpha,\nu} k_{r\alpha,\nu}}{\mu_{\alpha,\nu}} \left[p_{wf} - p_{\alpha,\nu} - \rho_{\alpha,\nu} g(z_{bh} - z_\nu)\delta(x - x_\nu)\right] \tag{2.19}$$

Well constraints may be specified as a pressure value (bottom well flow pressure) or as a rate value under surface or reservoir conditions. Pressure specified wells are set as a Dirichlet boundary conditions on nodes connected to the well, while the rate is distributed along the section of the well which is open to fluid flow

(perforated) for a rate specified well, then using Equation (2.19) the bottom hole pressure and the pressures at the nodes connected to the wells are modified.

When the bottomhole pressure is given, the flow rate of the well must be calculated using Equation (2.19). However, if the well is controlled by flow rate, then this equation must be solved for the bottomhole pressure.

In case of transient problems, the well equation must be calculated alongside the governing flow equations. Various approaches exist to obtain the time dependent parameters appearing in the well equation (phase densities, viscosities, pressures and the well index). If the properties are calculated at the time step t_n (i.e. current time-step where all other variables are known) the method is deemed explicit. When the variables are calculated at the next time step t_{n+1} (i.e. the future time step, for which none or most of the variables are unknown), the method is called implicit. Schemes involving pure versions and combined versions of these two approaches of time discretization exist, however there are numerical implications to each such as strict time-step limitations for explicit methods and the necessity of iterative matrix system solvers for large implicit problems.

3. Numerical methods

A usual approach for modeling two-phase fluid flow in porous medium is to use standard numerical models to approximate the partial differential governing equations. Although analytical solutions may be used for simple problems such as the Stuttgart leaky-well case, numerical methods provide flexibility for handling complex geometrical/geological systems. This section provides a short overview of the space and time numerical discretization which are implemented in the respective codes of the simulators used for the suggested benchmark. The application of these methods on the pressure and saturation governing equations is described in section 4.

3.1. Finite difference method

The finite difference method (FDM) is implemented in the commercial simulators, Eclipse and IMEX. Detailed information about this technique is found in (Celia & Gray, 1992).

A domain with finite size existing in a Cartesian coordinate system is assumed: the domain is rectilinear in shape with dimension L_x, L_y, L_z in directions x, y and z. This domain is then discretized by subdividing it into discrete, rectilinear volumes as illustrated in Figure 3.1.

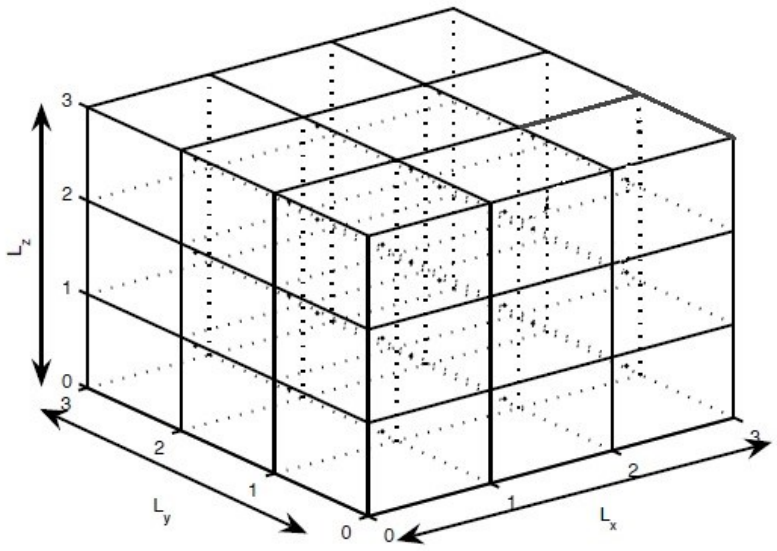

Figure 3.1: Spatial discretization for 3D finite difference approximation

(Celia & Gray, 1992)

The approximate values of the true solution for pressure and saturation at any point in time are represented at nodes which are at the corner of each discrete spatial volume. Each node is designated by the position in Cartesian space (x_i, y_j, z_k). The dimensions of each volume in x, y, and z are x_i, y_j, z_k respectively.

Given this spatial discretization, the next step is to approximate the derivatives in the governing equations with finite difference approximations. These finite differences are written in terms of the true solution of pressure and saturation located at each node in space and time. To demonstrate this concept in Equation (3.1), the second-order spatial derivative of *U* is taken, where *U* is the true solution to the continuous function *U=f(x)*.

$$\frac{\partial^2 U}{\partial x^2} \cong \frac{\left.\frac{\partial U}{\partial x}\right|_{x_{i+\frac{1}{2}}} - \left.\frac{\partial U}{\partial x}\right|_{x_{i-\frac{1}{2}}}}{x_{i+\frac{1}{2}} - x_{i-\frac{1}{2}}} \tag{3.1}$$

The resulting approximation is defined as the difference between 1st-order center differences that are defined at the half-points between neighboring cells. These derivatives are then approximated by differences between the values of the solution at two neighboring nodes in Equation (3.2) resulting in the 2nd order center differences:

$$\frac{\partial^2 U}{\partial x^2} \cong \frac{\frac{U_{i+1} - U_i}{x_{i+1} - x_i} - \frac{U_i - U_{i-1}}{x_i - x_{i-1}}}{x_{i+\frac{1}{2}} - x_{i-\frac{1}{2}}} \cong \frac{U_{i+1} - 2U_i + U_{i-1}}{(\Delta x)^2} \tag{3.2}$$

3.2. Finite volume method and the two point flux approximation

The two-point flux approximation is a finite volume scheme which is implemented in the simulation code of OPM. The finite volume method is another type of approximate solution for partial differential equations. Compared to the classical finite difference method the finite volume method (FVM) has the following advantages:

- The spatially discretized domain (mesh or grid) can accommodate to irregularly shaped boundaries to reduce geometric errors, also the mesh may be locally refined to give more resolution in regions of particular interest. However, this absolute flexibility is lost when the two-point flux approximation is applied as it generally converges for orthogonal grids only.

- The equations are presented in integral form and semi integral form keeping the temporal term as a partial differential shown in Equation (3.3) and (3.4). A consequence of this statement is that there is no need for dependent variables to be differentiable everywhere.

$$\iint_{\Omega} \frac{\partial U}{\partial t} d\Omega + \oint_{\Gamma} H \cdot \hat{n}\, d\Gamma = 0 \tag{3.3}$$

$$\frac{\partial U}{\partial t} + \oint_{\Gamma} H \cdot \hat{n}\, d\Gamma = 0 \tag{3.4}$$

- The finite volume method applied for conservation laws sustains conserved variables naturally: the total flow of a conserved quantity out of one cell is the same as that entering in the neighboring cell.

In the following paragraphs a short overview of the finite volume approximation is written when the finite volume method is applied to partial differential equation that takes the form given in Equation (3.5), but a detailed derivation of this procedure is described in (Causon, et al., 2011) and (Eymard, et al., 2010):

$$\frac{\partial U}{\partial t} + \nabla \cdot H = 0 \tag{3.5}$$

In Equation (3.5) U is the solution variable and the first term in the equation is the partial derivative of this U with respect to time. The second term is the divergence of flux density H that typically measures the net flux of U through a particular closed surface within the considered domain. The flux term is typically a function of the solution variable U. Equation (3.5) is called the finite volume form of a general partial differential equation (further on PDE).

Focusing on 2 dimensional partial differential equations, the first step is to integrate Equation (3.5) over region Γ of domain Ω, which results in the rearranged Equation (3.6) called the semi-integral finite volume form of a PDE. Using this finite volume form, the Gauss theorem can be applied that relates the flow of a vector field through a closed surface. The Gauss theorem states that the volume integral of the divergence of a vector field over the domain Ω can be replaced by the surface integral of the multiplication of a closed surface Γ of the domain Ω by its outward unit normal. The Gauss theorem is expressed in Equation (3.3)

$$\frac{\partial U}{\partial t} = -\frac{1}{\Omega}\oint_{\Gamma} H \cdot \hat{n}\, d\Gamma \tag{3.6}$$

Equation (3.6) states that the time dependent partial derivative equals to the surface integral of the flux term H multiplied by the outward pointing unit normal $\hat{n}$ of the arbitrary region Γ around the perimeter curve of Γ resulting in the total flux out of a given cell. Since the flux term is a function of the solution variable U which is likely to have different values in each cell on either side of a cell-face, fluxes are often discontinuous between two neighboring cells that yields typically unstable, non-conservative FVM unless a strategy (i.e. upwinding) is applied to resolve this discontinuity. In the FVM, the computational domain Ω is divided up into a mesh of finite number of polygonal cells, and then Equation (3.6) is approximated over each cell.

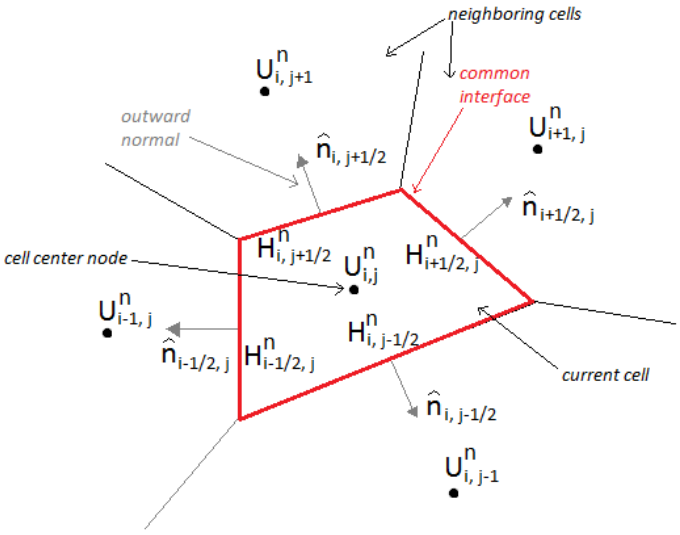

Figure 3.2: 2D finite volume cell at time level *n*

(Causon, et al., 2011)

As symbolized in Figure 3.2, segregating the domain Ω into finite quadrilateral cells and approximating the contour integral in Equation (3.6), the finite volume method is given in Equation (3.7):

$$\frac{\partial U}{\partial t} = -\frac{1}{\Omega}\left(H_{i+\frac{1}{2},j}\hat{n}_{i+\frac{1}{2},j} + H_{i-\frac{1}{2},j}\hat{n}_{i-\frac{1}{2},j} + H_{i,j+\frac{1}{2}}\hat{n}_{i,j+\frac{1}{2}} + H_{i,j-\frac{1}{2}}\hat{n}_{i,j-\frac{1}{2}}\right) \tag{3.7}$$

The left hand side in Equation (3.7) is the temporal derivative of U and the right hand side is the approximated total flux flowing out of the cell with indices of (i, j).

The two point flux approximation is a particular FV scheme estimating the fluxes on the neighboring cell interfaces in case of diffusive fluxes which is encountered in Darcy's law. Considering a diffusive flux that takes the form of:

$$H(x,t) = -\Lambda(x,t)\nabla U(x,t) \tag{3.8}$$

The first term on the right hand side in Equation (3.8) is a linear operator of the time and space variables, and the second term is the spatial derivative of the solution variable *U(x, t)* of the problem.

For any adjacent cells of L and K with the interface σ (see Figure 3.3), a simple consistent and conservative flux expression may be obtained upon satisfying two conditions:

1) The linear operator is an identity operator.
2) The mesh is orthogonal: in each adjacent cells (K and L) such particular points of x_K and x_L exist, called the center of the control volume, where the straight line connecting x_K and x_L is orthogonal to the common face of these cells. This condition is portrayed in Figure 3.3.

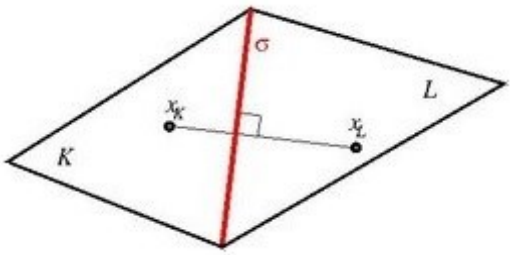

Figure 3.3: Orthogonal neighboring cells in two point flux approximation

(Eymard, et al., 2010)

The approximation formula for a flux defined in Equation (3.8) is given by Equation (3.9), where $d(c_K, c_L)$ denotes the Euclidean distance between points x_K with coordinates c_K, and x_L with coordinates c_L.

$$H(x,t)_{K,L} = \frac{U_K - U_L}{d(c_K, c_L)} \tag{3.9}$$

3.3. Discretization of transient problem

The temporal term of a partial differential equation may be estimated using Euler-type of approximation. There are different types of Euler methods with varying degrees of stability. A backward Euler method, where the solution at the next time step (t_{n+1}) also appears implicitly in the spatial derivative, results in an unconditionally stable solution, while in explicit forward Euler methods the solution of the spatial derivative term is taken from the actual time step (t_n). Explicit methods are conditionally stable: over a critical time step the approximation error becomes unbounded and does not converge to a solution, whilst the implementation of an implicit approach is generally more difficult.

The implicitly discretized form of the time dependent term of Equation (3.5) is inscribed in Equation (3.10), the explicit form is noted in Equation (3.11).

$$\frac{\partial U}{\partial t} = \frac{U_m^{n+1} - U_m^n}{t_{n+1} - t_n} = -\nabla \cdot H(U_m)|^{n+1} \tag{3.10}$$

$$\frac{\partial U}{\partial t} = \frac{U_m^{n+1} - U_m^n}{t_{n+1} - t_n} = -\nabla \cdot H(U_m)|^{n} \tag{3.11}$$

For the temporal discretization the implicit backward Euler approximation is utilized by all of the simulators I used for the modelling of CO_2 injection into the Johansen formation. (Celia & Gray, 1992)

4. The applied simulators

Three simulators were used to model isothermal, immiscible CO_2 injection into the saline aquifer of the Johansen formation. The proposed and used software tools are listed below. A brief introduction of these programs and the numerical solution methods implemented in them are outlined in the following sections:

- CMG (Computer Modelling Group Ltd.) – IMEX (black oil simulator)
  - Version: 2013.10
- Eclipse (Schlumberger Ltd.) – ECLIPSE 100 (black oil simulator)
  - Version: 2011.20
- OPM (Open Porous Media Initiative) – opm-core module
  - Version: 2013.10

4.1. Eclipse

The Eclipse simulator suite is a software package developed by Schlumberger Ltd. which is a French oil field company founded in 1926 with headquarters in Houston (Texas, USA). The Eclipse family of simulators consists of two separate simulating tools:

- ECLIPSE 100 (or E100) is a fully implicit, finite difference, three phase general purposed black oil simulator (applied for modelling in this thesis).
- ECLIPSE 300 (or E300) is a K-value thermal compositional simulator with cubic equation of states which has the temporal discretization approaches of implicit pressure – explicit saturation (IMPES), fully implicit and in adaptive implicit method (AIM). The spatial discretization of the governing equation is finite difference method.

Based on (Schlumberger Ltd., 2011), the residual form of the mass conservation law is solved indicated in Equation (4.8). The notation R stands for the non-linear residual for all fluids present in the reservoir calculated by Equation (4.9). The vector [p S_w] contains the primary solution variables which are the pressure and one of the phase saturations for a two phase model.

$$\begin{bmatrix} R_w \\ R_g \end{bmatrix} \left(\begin{bmatrix} p \\ S_w \end{bmatrix} \right) = 0 \tag{4.8}$$

$$R_\alpha = \frac{dV_{\alpha,sc}}{dt} + Q_{block,\alpha} + Q_{well,\alpha} \tag{4.9}$$

The volume change in Equation (4.9) during the time step $\Delta t = t_{n+1} - t_n$ in an implicit solution is the difference between the mass at time step $t_{n+1} = t_n + \Delta t$ and mass of time step t_n where the mass at the given time t_n is determined by Equation (4.10):

$$V_{\alpha,sc}\big|_{t_n} = V_P \frac{S_\alpha}{B_\alpha} \tag{4.10}$$

The flow rate from a neighboring cell *c* into grid cell *m* is enumerated by the transmissibility between the two cells and the potential difference as shown in Equation (4.11). The first multiplier is the transmissibility established in Equation (4.12) and the second term is the potential difference given in Equation (4.13).

$$Q_{block,\alpha,m} = \sum_c \left(T_{c,\alpha} d\Phi_c\right) \tag{4.11}$$

$$T_{c,\alpha} = \frac{k\, k_{r\alpha}}{\mu_\alpha B_\alpha}\bigg|_c \tag{4.12}$$

$$d\Phi_c = p_{\alpha,c} - p_{\alpha,m} - \rho_\alpha g(z_c - z_m) \tag{4.13}$$

The last term in Equation (4.9) is the net flow rate into the wells. The flow rate into a production well from grid cell *m* is defined as:

$${Q_{well,\alpha}}^{\nu} = -\left[WI \frac{k_{r\alpha}}{\mu_r B_r}\right]_\nu \left(p_{\alpha,\nu} - c_{head,\nu} - p_{wf}\right) \tag{4.14}$$

In the black oil simulator E100 the multi-phase, non-linear fully implicit equations are solved with high accuracy by reducing all residuals to very fine tolerances, especially the material balance error. The tolerance is analyzed by two error definitions which are:

- Material balance error: the sum of the residuals for each phase over all reservoir cells corresponds to the net mass accumulation plus the net influx through the wells (Equation (4.15)) scaled to equivalent field saturation values (Equation (4.16)). The flow terms from Equation (4.9) cancel because the sum of the flow out of one cell and the corresponding flow into its neighboring cell equals zero.

$$\sum_m R_{\alpha,m} = \sum_m \frac{dV_{\alpha,sc,m}}{dt} + \sum_m Q_{well,\alpha,m} \tag{4.15}$$

$$MB_\alpha = B_\alpha(t_{n+1} - t_n)\left[\frac{\sum_m R_{\alpha,m}}{V_P}\right] \tag{4.16}$$

- Convergence error: the maximum of the saturation normalized residuals over all cells of the reservoir marked in Equation (4.17)

$$CNV_\alpha = B_\alpha(t_{n+1} - t_n)MAX\left[\frac{R_{\alpha,m}}{V_P}\right] \tag{4.17}$$

Non-linearity is solved by the Newton iteration method and the solution of the resulting linear equations is determined by the Orthomin algorithm after each Newton iteration. The reader is referred to (Greenbaum, 1987) for an explanation of the Orthomin approximation.

4.2. Computer Modelling Group

CMG is a reservoir simulator software package used in the oil and gas industry, developed by the Computer Modelling Group Ltd. with a base in Calgary, Alberta, Canada. The software is composed of three simulation applications:

- IMEX is a conventional three-phase black oil simulator used for primary, secondary and tertiary (enhanced) oil recovery processes;
- GEM is an equation of state compositional simulator applied for unconventional reservoirs;
- STARS is a simulator used for non-isothermal flow.

IMEX is a three-phase black oil simulator with gravity and capillary terms which can be run in explicit, fully implicit – applied in this thesis - and adaptive implicit modes. The law of conservation of mass presented in Equation (2.1) for the water phase and for the gas phase is discretized using the finite difference method in first order backward form in time and second order central differences in space with upstream mobility displayed in Equation (4.1) – (4.2). (Computer Modelling Group Ltd., 2013)

$$\frac{V_{B,m}}{t_{n+1}-t_n}\left[\left(\frac{\phi S_w}{B_w}\right)_m^{n+1}-\left(\frac{\phi S_w}{B_w}\right)_m^{n}\right]$$
$$=\left[T_{w,m+\frac{1}{2}}(p_{w,m+1}-p_{w,m})\right]^{n+1}-\left[T_{w,m-\frac{1}{2}}(p_{w,m}-p_{w,m-1})\right]^{n+1} \quad (4.1)$$

$$\frac{V_{B,m}}{t_{n+1}-t_n}\left[\phi^{n+1}\left(\frac{R_s S_o}{B_o}+\frac{S_g}{B_g}\right)_m^{n+1}-\phi^{n}\left(\frac{R_s S_o}{B_o}+\frac{S_g}{B_g}\right)_m^{n}\right]$$
$$=\left[T_{o,m+\frac{1}{2}}R_{s,m}(p_{o,m+1}-p_{o,m})\right]^{n+1}-\left[T_{o,m-\frac{1}{2}}R_{s,m}(p_{o,m}-p_{o,m-1})\right]^{n+1}$$
$$+\left[T_{g,m+\frac{1}{2}}(p_{g,m+1}-p_{g,m})\right]^{n+1}-\left[T_{g,m-\frac{1}{2}}(p_{g,m}-p_{g,m-1})\right]^{n+1} \quad (4.2)$$

Water phase is considered slightly compressible, gas phase is fully compressible and rock compressibility is also taken into account in these equations. I disregard the conservation of oil mass as there is no oil present in the proposed model which also leads to the negligence of gas-oil dissolution (R_s = 0). Gas and water are recognized as immiscible phases. Therefore in Equation (4.2) the first two terms of the space discretized expressions equal zero and the first part of the time discretization amounts to null as these are all the segments including solution gas-oil ratio. The simplified form of Equation (4.2) is Equation (4.3):

$$\frac{V_{B,m}}{t_{n+1}-t_n}\left[\left(\frac{\phi S_g}{B_g}\right)_m^{n+1}-\left(\frac{\phi S_g}{B_g}\right)_m^{n}\right]$$
$$=\left[T_{g,m+\frac{1}{2}}(p_{g,m+1}-p_{g,m})\right]^{n+1}-\left[T_{g,m-\frac{1}{2}}(p_{g,m}-p_{g,m-1})\right]^{n+1} \quad (4.3)$$

The notation $T_{\alpha,m}$ in the above equations is the property called transmissibility which is a group of terming constituted of the phase permeability, dynamic viscosity and formation volume factor expressed in Equation (4.4).

$$T_{\alpha,m+\frac{1}{2}}=\left.\frac{k\,k_{r\alpha}}{\mu_\alpha B_\alpha}\right|_m$$
$$T_{\alpha,m-\frac{1}{2}}=\left.\frac{k\,k_{r\alpha}}{\mu_\alpha B_\alpha}\right|_{m-1} \quad (4.4)$$

These non-linear equations are deciphered by the linear solver design called Newton iteration method. The linearized matrix solution equation is then solved by the Generalized Minimum Residual (GMRES) algorithm. Detailed description of these methods may be found in (Deuflhard, 2011) and (Greenbaum, 1987).

In IMEX, wells are implemented using Equation (2.8) in a fully implicit approach. The well index is calculated by Equation (4.5), and the surface flow rates for the gas and for the water phase by Equation (4.6) and (4.7).

$$WI = \frac{2\pi \cdot k \cdot h \cdot f_{well} \cdot f_{geo}}{ln\left(\frac{r_e}{r_{wb}}\right) + s} \tag{4.5}$$

$$Q_{g,sc} = \sum_{\nu} WI^{\nu} \frac{k_{rg}}{\mu_g} (p_{wf} + p_{wh} - p_{g,\nu})/B_g \tag{4.6}$$

$$Q_{w,sc} = \sum_{\nu} WI^{\nu} \frac{k_{rw}}{\mu_w} (p_{wf} + p_{wh} - p_{w,\nu})/B_w \tag{4.7}$$

For producing wells the bottomhole pressure is always smaller than the block pressure, which yields negative flow rate. In case of injectors, the pressure ratio is the exact opposite and Equation (4.6)-(4.7) result in positive flow rate.

4.3. Open Porous Media

The Open Porous Media (OPM) initiative provides a set of open-source tools focusing on the modelling of fluid transport in porous media. The initiative was proposed in June 2009 by the Statoil Research Center in Trondheim, Norway, and currently is supported by ten organizations (e.g.: SINTEF Applied Math, IRIS Energy, Total E&P, University of Bergen, University of Stuttgart, University of Heidelberg). The software is built on the C++ template libraries of Distributed and Unified Numerics Environment (DUNE). DUNE is also a modular toolbox for solving partial differential equations with grid-based methods. (Rustad, 2013)

The reason for including this simulator in the analysis despite its young development history is that it was possible to load the same available corner point grid as in the other two (Eclipse and IMEX), it has the ability to model multi-phase fluid flow, and finally because its underlying spatial discretization is different from Eclipse and IMEX. It is also an open source code and hence no costs were involved.

The modules used during the simulation of my benchmark are:

- Opm-parser: a comprehensive parser for reading input data from the Eclipse reservoir simulator.
- Dune-cornerpoint: a DUNE module with implementation of corner point grids.
- Opm-core: it provides infrastructure and utilization for linear solvers (of non-linear problems) and basic solvers (for linear/linearized problems).

In the opm-core module the solver used for the black oil pressure calculation utilizes the spatial discretization of two-point flux approximation. As mentioned in Section 3.2 the two point flux approximation is a scheme applied in the finite volume method to estimate diffusive fluxes. In the pressure equation the flux term over the common interface of neighboring cells *m* and *m+1* takes the following form:

$$H = -\oint_{\Gamma} \frac{k_r}{\mu} \nabla p \cdot \hat{n}_{m,m+1} \, d\Gamma$$

(4.18)

The gradient of pressure is then estimated using the pressure values of the neighboring center points (c_{m+1}, c_m) of these cells divided by their Euclidian distance:

$$\nabla p \approx \frac{2(p_{m+1} - p_m)}{d(c_{m+1}, c_m)}$$

(4.19)

The directional cell mobility (λ), which corresponds to the linear operator of the diffusive flux, across the common interface (Γ) is estimated by a distance weighted harmonic mean:

$$\frac{k * k_r}{\mu} = \lambda_{\Gamma} \approx \frac{d(c_{m+1}, c_m)}{\frac{d(c_{m+1}, \Gamma)}{\lambda_{\Gamma,m+1}} + \frac{d(c_m, \Gamma)}{\lambda_{\Gamma,m}}}$$

(4.20)

Inserting Equation (4.19) and (4.20) into Equation (4.18) the flux term is then approximated as:

$$H_{\Gamma} = -\frac{2(p_{m+1} - p_m)}{d(c_{m+1}, c_m)} \oint_{\Gamma} \frac{d(c_{m+1}, c_m)}{\frac{d(c_{m+1}, \Gamma)}{\lambda_{\Gamma,m+1}} + \frac{d(c_m, \Gamma)}{\lambda_{\Gamma,m}}} \cdot \hat{n} \; d\Gamma = \frac{2A_{\Gamma}(p_{m+1} - p_m)}{\frac{d(c_{m+1}, \Gamma)}{\lambda_{\Gamma,m+1}} + \frac{d(c_m, \Gamma)}{\lambda_{\Gamma,m}}}$$

(4.21)

In Equation (4.21) A_{Γ} denotes the area of the common interface Γ. Defining transmissibility as noted in Equation (4.22) as group of terming from Equation (4.21),

the semi-discretized pressure equation applying for multi-phase, slightly compressible fluids, takes the form given in Equation (4.23)

$$T_\Gamma = \frac{2A_\Gamma}{\frac{d(c_{m+1},\Gamma)}{\lambda_{\Gamma,m+1}} + \frac{d(c_m,\Gamma)}{\lambda_{\Gamma,m}}} \tag{4.22}$$

$$\phi c_f \frac{\partial p}{\partial t} - \sum_\Gamma T_\Gamma \left(p_{m+1} - p_m\right) = 0 \tag{4.23}$$

For the detailed description of discretized form of the saturation equation the reader is referred to the articles of (Lee, et al., 2008) and (Eymard, et al., 2010). As temporal discretization an implicit scheme is applied and the non-linearity of the transport equation is handled by reordered Gauss-Seidel iteration. The default linear solver implemented in the opm-core simulator is a method called Unsymmetric Multifrontal (UMFPACK) method (Davis & Duff, 1993).

5. Model description of the Johansen benchmark

5.1. Model domain

The Johansen formation is located at the west coast of Norway in the deeper part of the Sognefjord delta. The Sognefjord formation which is the uppermost sand layer in the Sognefjord delta is the reservoir for the Troll gascap field. The depth level of the Johansen formation situated more than 500 m below the Sognefjord formation ranges from 2200 – 3100 m with a constant temperature of 94 °C. The Johansen and the Sognefjord formation is isolated by the shale of Dunlin Group. The lateral extension of the formation is 100 x 60 km^2 with an average reservoir thickness of 100 m. Due to the large size of the formation only a 16 x16 km^2 part of the structure is chosen as the model domain illustrated in Figure 5.1. The model was created as part of the MatMoRA project (Eigestad, et al., 2009) based on existing high quality seismic and log data from more than 12 exploration wells.

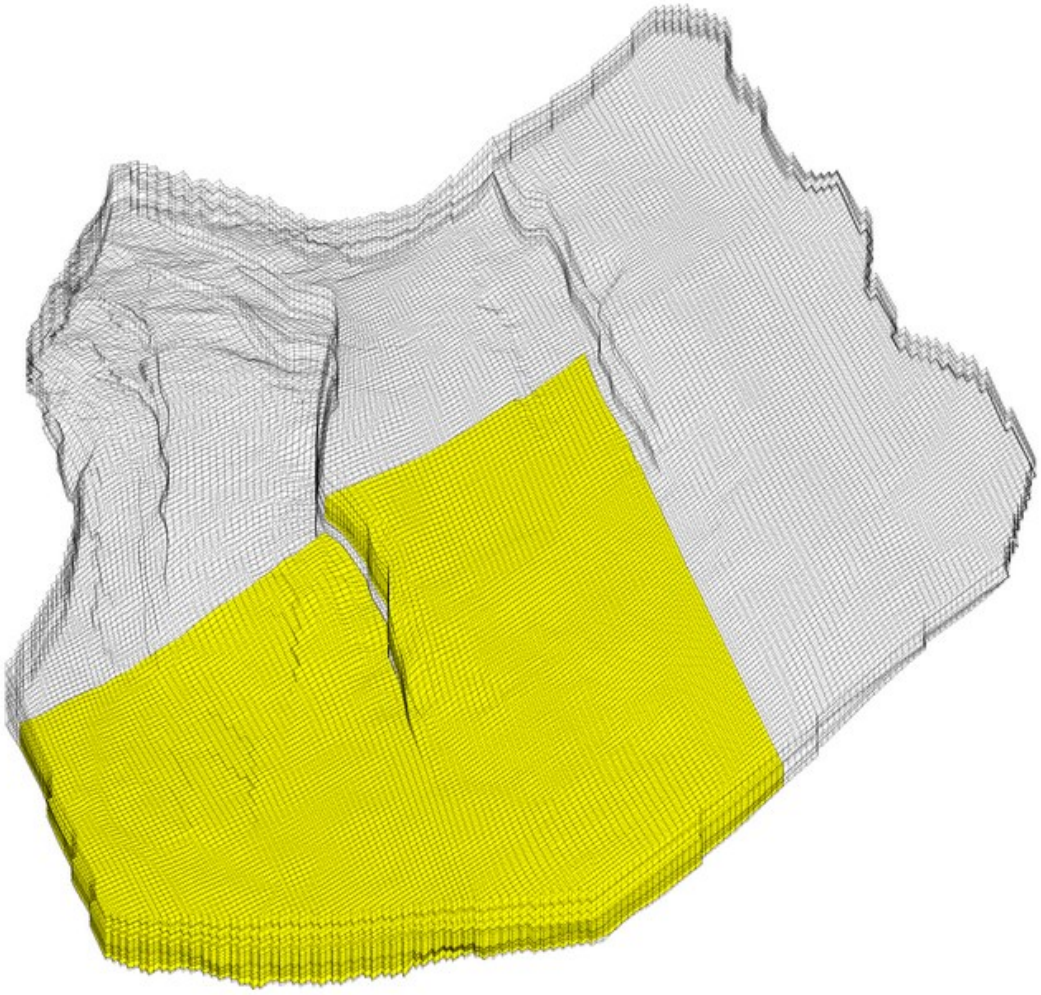

Figure 5.1: NPD5 structure as part of the full field model

(Dahle, 2009)

The model is divided into 11 layers, where the top five layers correspond to the Dunlin Group shale, the next five layers are the Johansen formation and at the bottom a sealing shale layer of the Amundsen Group is defined. For the sector model NPD5 a 100 x 100 mesh was generated with 11 layers resulting in 110 000 grid blocks. The simulation grid is given in corner point format composed of hexahedral elements.

The corner point grid format is an extended type of Cartesian grid: all elements are hexahedral cells with 8 - not necessarily distinct - vertices where the grid block corners are distributed along vertical pillars (Figure 5.2). The blocks may not be conforming from one cell to its neighboring cell as vertical faulting is allowed in the grid system.

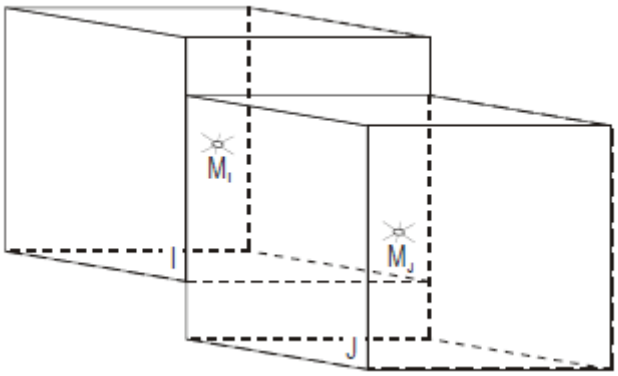

Figure 5.2: Corner point grid arrangement of two adjacent cells

(Heinemann, 2013)

The fault interpretation of the structure is also based on the seismic data. The most significant fault of the area is the north-south trending fault shown in Figure 5.3 with green shades which is recognized as a fully permeable fault (fault transmissibility set to value 1). The pinch-out area of the Johansen formation to the west marked by the empty grid blocks is based on seismic information confirmed by well data.

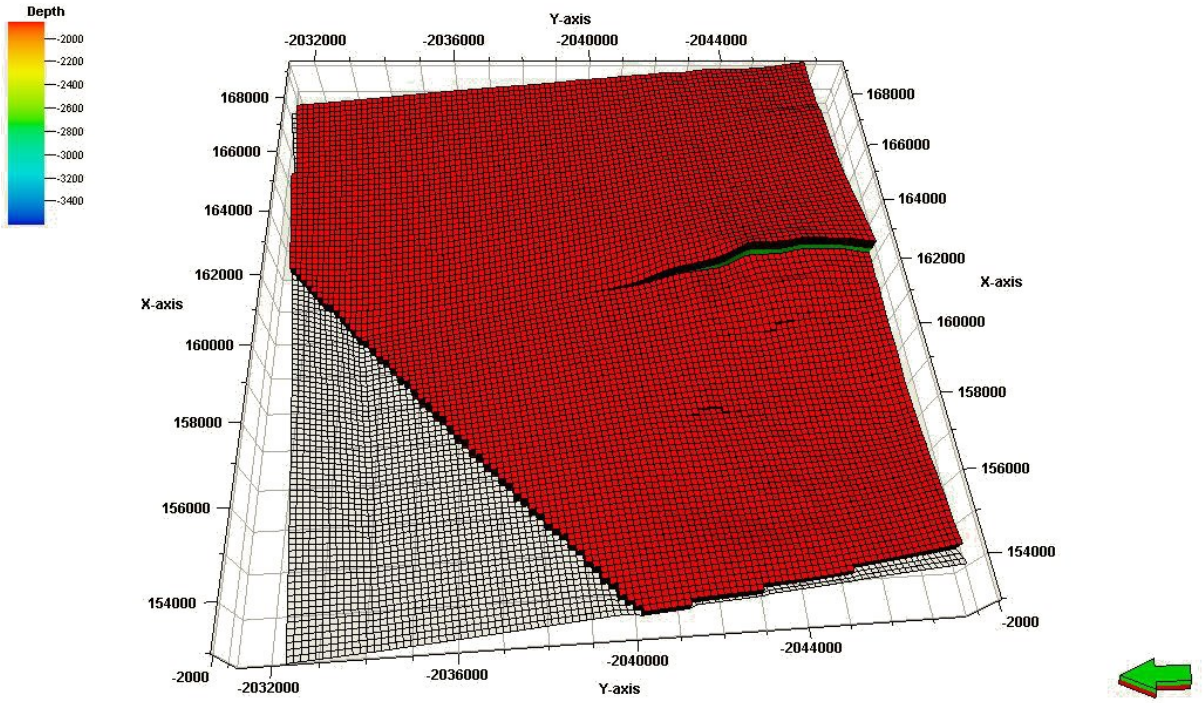

Figure 5.3: NPD5 sector model of Johansen formation (depth is in meters)

Porosity distribution for each layer was calculated by a porosity-depth trend depending on log and core data from the exploration wells penetrating the Johansen field. This data set has a value range from 10% up to 30%. Permeability values in direction x ranging from 64-900 mD were modeled from porosity-permeability trends obtained from lithology data similar to the Johansen formation by cause of limited data in the study area. The permeability in direction y is assumed equal to the permeability in direction x and the vertical permeability is considered ten times smaller than the horizontal permeability in order to lessen vertical flow effects. All shale layers of the Dunlin Group have constant porosity of 10% and homogeneous horizontal permeability of 0.01 mD. Porosity distribution of all Johansen-layers may be found in Appendix A, permeability data is provided in Appendix B. (Dahle, 2009)

5.2. Fluid and rock models

The main purpose of this benchmark is to model CO_2 storage for which fluid flow simulation is limited to two-phase isothermal immiscible flow. The benchmark is divided into two subcases:

- The first case assumes both fluids - CO_2 and brine - incompressible.
- In the second case brine is still considered incompressible, but CO_2 is assumed as slightly compressible phase.

As thermal and miscibility effects are neglected and the gas phase is composed of one single component, the use of an equation of state compositional simulator is not necessary, and solving the two-phase black oil model with water and gas phases produces accurate results. Capillary effects are neglected while gravity is taken into account.

The fluid properties for the gaseous CO_2 and the liquid brine phases are summarized in Table 5.1 for the first fully incompressible subcase. For the subcase with varying degree of compressibility all fluid properties are provided in Table 5.2. The PVT data is given for 94°C. All PVT data was created as part of the MatMoRA project.

Table 5.1: Fluid properties for incompressible case

Property name	Notation	Value	Unit
Brine surface density	$\rho_{w,sc}$	1149.81	kg/m^3
Brine formation volume factor	$B_{w,sc}$	1.0	rm^3/sm^3
Brine compressibility	c_w	0.0	1/bar
Brine viscosity @ 350 bar	μ_w	0.5014	cp
Brine viscosibility	$c_{\mu w}$	0.0	cp/bar
CO_2 surface density	$\rho_{g,sc}$	1.8415	kg/m^3
CO_2 formation volume factor @ 350 bar	$B_{g,sc}$	1.0	rm^3/sm^3
CO_2 compressibility @ 350 bar	c_g	0.0	1/bar
CO_2 viscosity @ 350 bar	μ_g	0.063164	cp
CO_2 viscosibility @ 350 bar	$c_{\mu g}$	0.00015	cp/bar

Table 5.2: Fluid properties for compressible case

Property name	Notation	Value	Unit
Brine surface density	$\rho_{w,sc}$	1149.81	kg/m^3
Brine formation volume factor	$B_{w,sc}$	1.0	rm^3/sm^3
Brine compressibility	c_w	0.0	1/bar
Brine viscosity @ 350 bar	μ_w	0.5014	cp
Brine viscosibility	$c_{\mu w}$	0.0	cp/bar
CO_2 surface density	$\rho_{g,sc}$	1.8415	kg/m^3
CO_2 formation volume factor @ 350 bar	$B_{g,sc}$	0.018411	rm^3/sm^3
CO_2 compressibility @ 350 bar	c_g	0.000811	1/bar
CO_2 viscosity @ 350 bar	μ_g	0.063164	cp
CO_2 viscosibility @ 350 bar	$c_{\mu g}$	0.00015	cp/bar

Both sand and shale are assumed incompressible, therefore rock compressibility is equal zero. As shale has really low permeability it acts as a sealing layer, and assigning the same rock data for both of them will not lead to significant error. The relative permeability data issued by Eigestadt et al. (2009) is compiled in

Table 5.3: it is a water wet rock; CO_2 has zero end-point saturation with maximum relative permeability of 0.2142; the connate water saturation is 0.1 with maximum relative permeability of 0.8. The same relative permeability curve is applied in both subcases. (Dahle, 2009)

Table 5.3: Relative permeability data

S_w	k_{rw}	k_{rg}
0.1	0.0000	0.2142
0.2	0.0099	0.1057
0.3	0.0395	0.0474
0.4	0.0889	0.0188
0.5	0.1580	0.0063
0.6	0.2469	0.0017
0.7	0.3556	0.0003
0.8	0.4840	0.0002
0.9	0.6321	0.0001
1.0	0.8000	0.0000

5.3. Boundary and initial conditions

As the implementation of boundary conditions is not as advanced in the OPM simulator, no flow boundary condition is assumed over all boundaries of the model domain: on the sides, at the top and at the bottom as well. However to avoid “bursting” the reservoir by the constant injection, three water producing wells were defined with a cumulative water production equivalent to the amount of the injected gas.

The reservoir is completely water saturated prior to injection, the gas-water contact is defined far above the model domain to avoid any CO_2 leakage from the top through the fault. The initial pressure distribution is hydrostatic with a reference pressure value of 310 bar at 3100 m depth. Figure 5.4 illustrates the initial pressure distribution for the first sand layer of the Johansen formation (6th layer in the model domain).

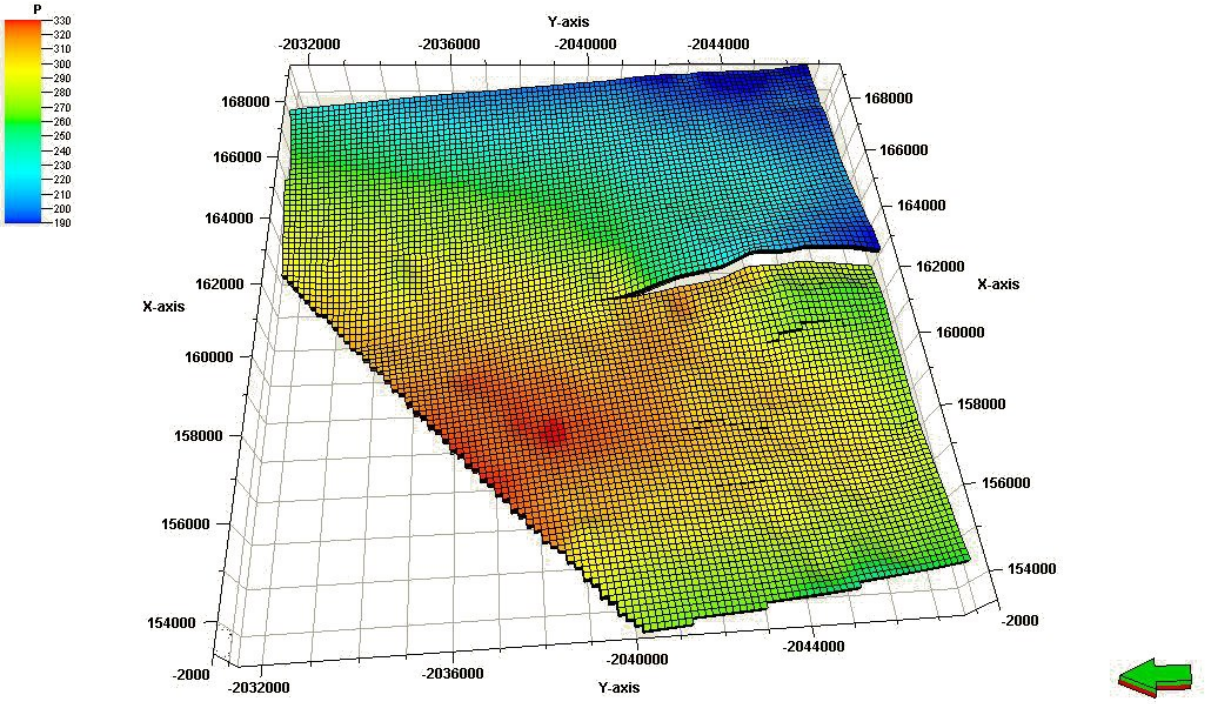

Figure 5.4: Initial pressure distribution in layer 6

5.4. Well model

CO_2 is injected through a single well positioned near the middle of the domain (see Figure 5.5), while three wells produce brine to prevent unexpected accumulation in the formation as closed boundary conditions are presumed at all sides of the domain including top and bottom as well.

Table 5.4: Well model definition (location and constraint)

Well name	Cell indices connected to the well			Well type	Well constraints
INJ	48	48	From 6 to 10	CO_2 injector	60 000 rm^3/d
PROD1	5	5	From 6 to 10	Brine producer	20 000 rm^3/d
PROD2	62	5	From 6 to 10	Brine producer	20 000 rm^3/d
PROD3	5	95	From 6 to 10	Brine producer	20 000 rm^3/d

CO_2 is injected with a surface flow rate of 60 000 m^3/day over 20 years of simulation time. The cumulative production of the water producers must equal to this value, evenly distributing this amount leads to a surface water production of 20 000 m^3/day per well. Table 5.4 outlines the position of the wells by naming the cell indices in each direction to which the wells are connected. The completion data is administered in Appendix C. The locations of the wells are visualized in Figure 5.5.

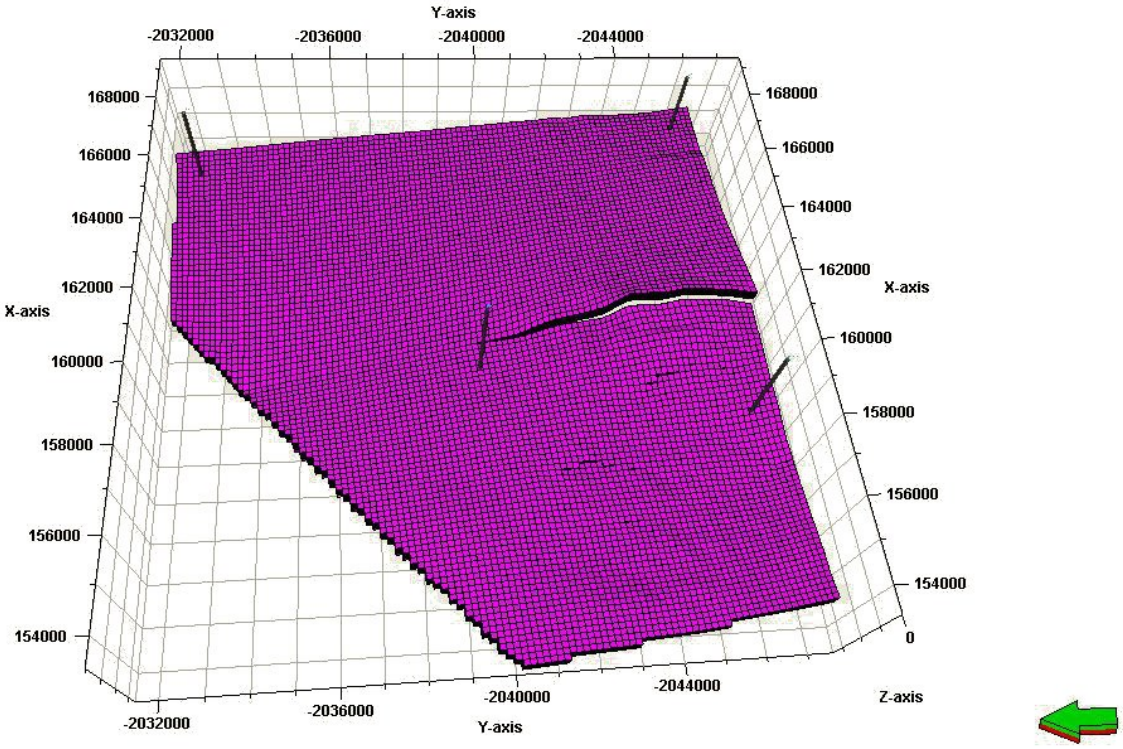

Figure 5.5: Visualization of the wells

6. Results

6.1. Capabilities and limits of the applied simulators

A very important factor for my choice of software tools to model the benchmark problem I proposed in this thesis is that the Johansen data set that I used is provided in an Eclipse corner point grid format. Among those simulators that are able to read corner point grids, IMEX and Eclipse are such commercial programs which have a good converting interface and both are available for the Chair of Reservoir Engineering. Although OPM is a recently developed software (the development started only in 2009), it has an Eclipse grid reader module implemented, and thus the very same mesh could be used for all three simulators. With this, the deviation in the results caused by different grid structure is completely avoided. Another advantage of OPM is that it is an open source code, and thus a user has access to the source code. This is a feature not available for commercial software and it helped me gain further understanding of how a reservoir simulator works.

OPM does have its limitations in modelling exactly by the cause of its really young development history:

- The opm-core module is only able to simulate two-phase flow: only “oil” and “water” phase can be defined in the input file.
- In this version of code only the possibility of injecting the “water phase” has been implemented, the injection of “oil phase” had not been programmed into the code.

Due to these reasons I had to use the following fluid model definition: CO_2 was defined as the “water phase” in the program and the brine initially present in the Johansen formation was declared as the “oil phase” in the code. This uncommon phase definition lead to several problems during the model definition and limits in the property settings. As “water phase” is considered a fluid with constant compressibility, CO2 had to be defined using only a single value of compressibility instead of setting it as a fully compressible gas phase with pressure dependent compressibility. Since brine is assumed as an incompressible fluid in the model definition, the “oil” compressibility was set to zero.

Another constraint worth mentioning is that the opm-core simulator only allows the setting of Dirichlet boundary conditions. Neumann boundary conditions were not implemented in the 2013.10 version. Certain commercial programs (such as IMEX),

which are generally used to make field development projects with real site data, specify aquifers as a boundary condition definition type instead of strict Dirichlet or Neumann boundary conditions.

A disadvantage of the commercial software, Eclipse and IMEX is the inaccurate formulation of an incompressible fluid. In these simulators, incompressibility is defined by modifying the variation of formation volume factor with pressure to output a range of values between 0.9999 and 1. In contrast, in OPM the fluid compressibility could be exactly defined as 0, providing a more accurate incompressible fluid model.

6.2. Volume changes

The diagrams from Figure 6.1 - Figure 6.4 present the predicted changes in the CO_2 volume existing in the reservoir and the brine volume leaving the reservoir over time in the suggested incompressible case. The predicted quantity of CO_2 and the amount of brine leaving the reservoir in all three simulators demonstrate negligible dissimilarity which proves the statement that the different spatial discretization methods do not produce much discrepancy in case of two-phase, immiscible, incompressible fluid flow in a rock system with negligible compressibility.

The changes of volumes are plotted versus time over the 20 years of simulation. All volumes are calculated at surface conditions.

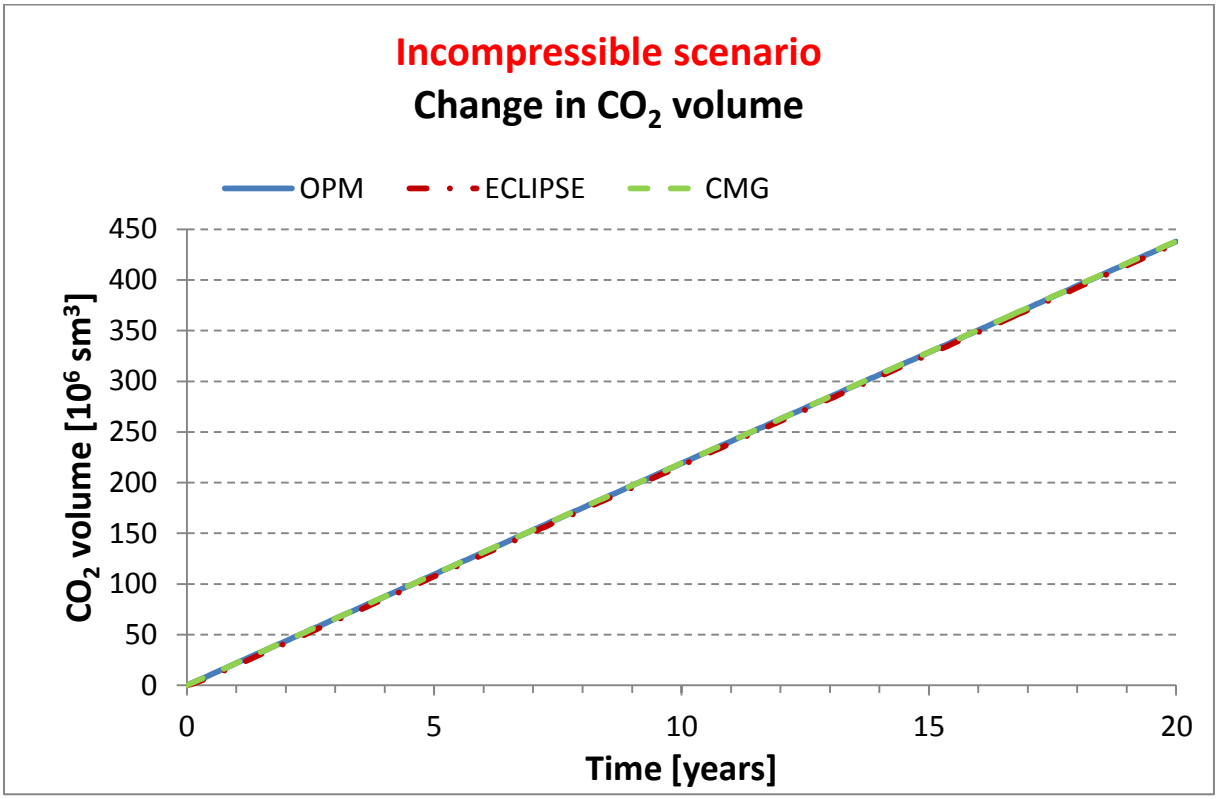

Figure 6.1: Cumulative CO_2 injection in the incompressible model

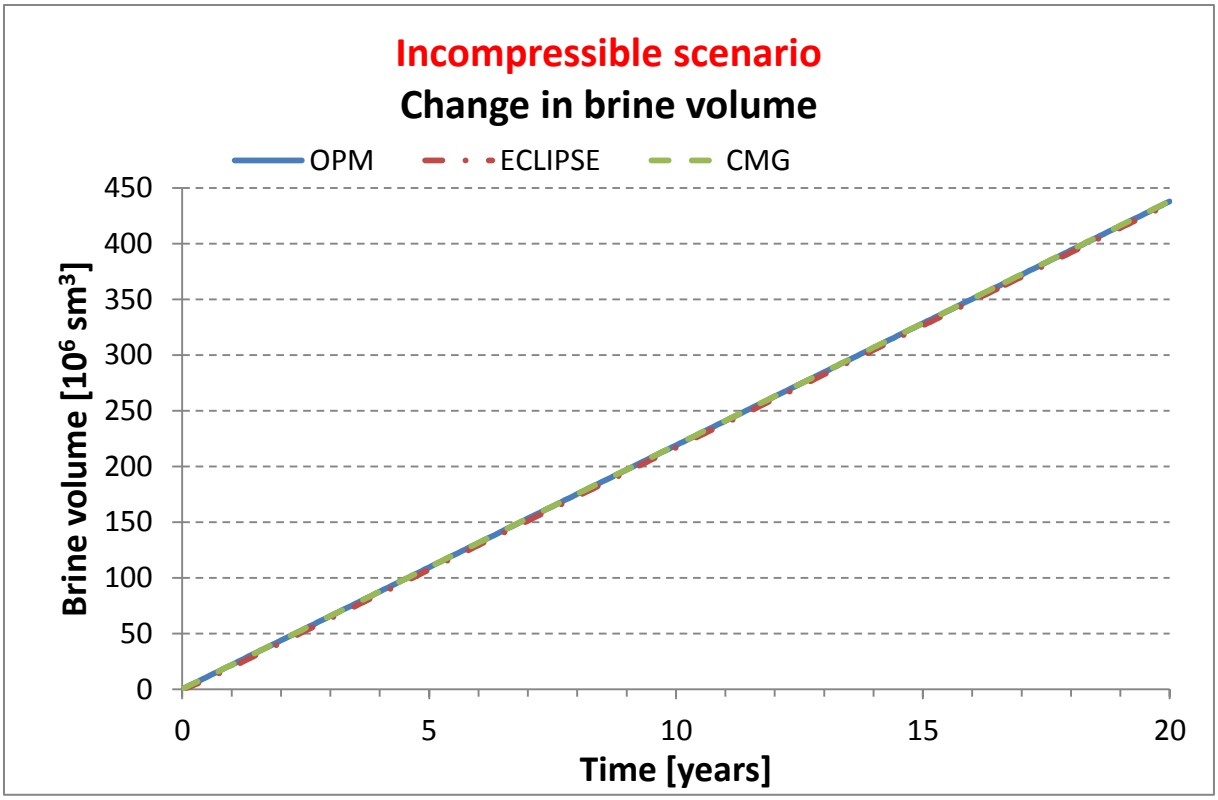

Figure 6.2: Cumulative brine production in the incompressible case

When fluid compressibility is introduced into the model definition, the changes in the CO_2 amount existing in the reservoir predicted by the three simulators are slightly different illustrated in Figure 6.3. After 20 years of CO_2 injection IMEX calculated the most CO_2 volume, over 31 billion m^3 at surface conditions, and OPM determined the least quantity, 26 billion surface m^3. The difference is about 5 billion surface m^3 which yields a divergence of about 16% between IMEX and OPM. The results predicted by Eclipse are about 2 billion higher than the volume approximated by OPM.

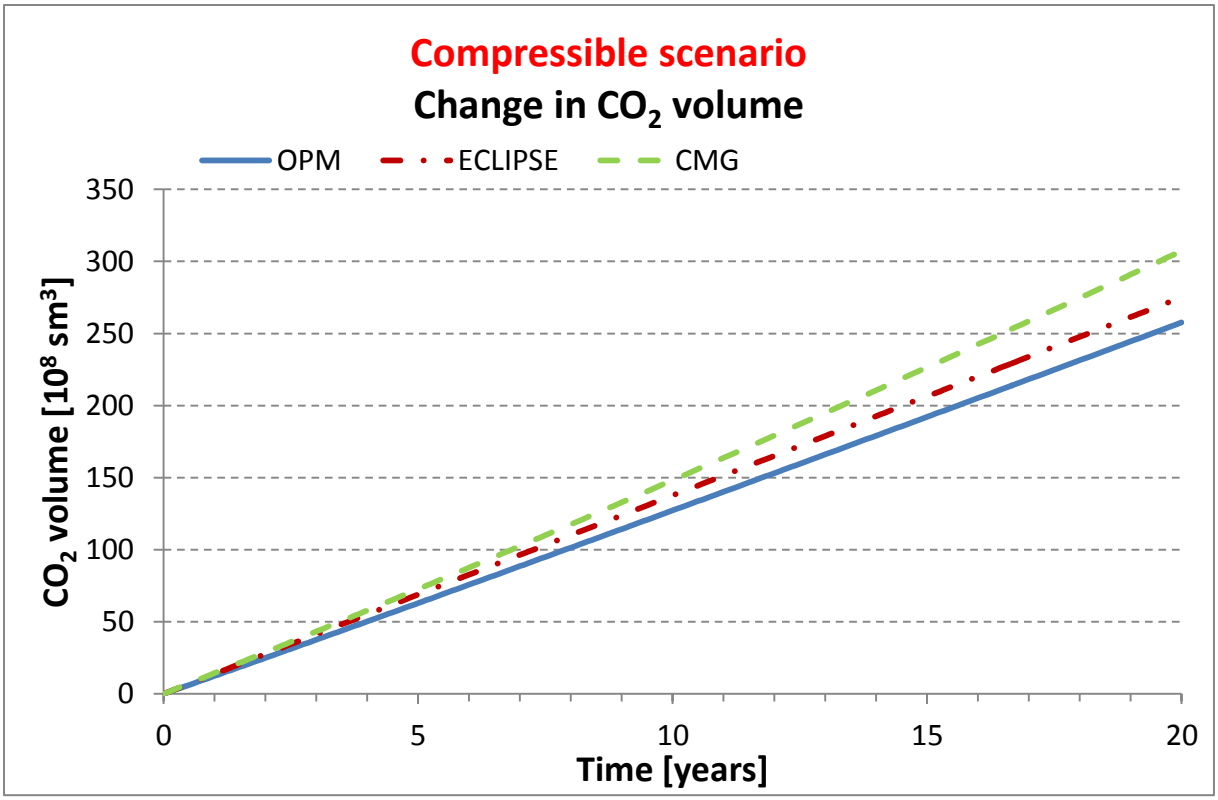

Figure 6.3: Cumulative CO_2 injection in the compressible model

Brine is considered incompressible in the compressible scenario, the total brine amount leaving the reservoir equals to the quantity predicted in the incompressible case for Eclipse, IMEX and OPM as well. The changes in brine volumes calculated by these software are in good agreement as shown in Figure 6.4.

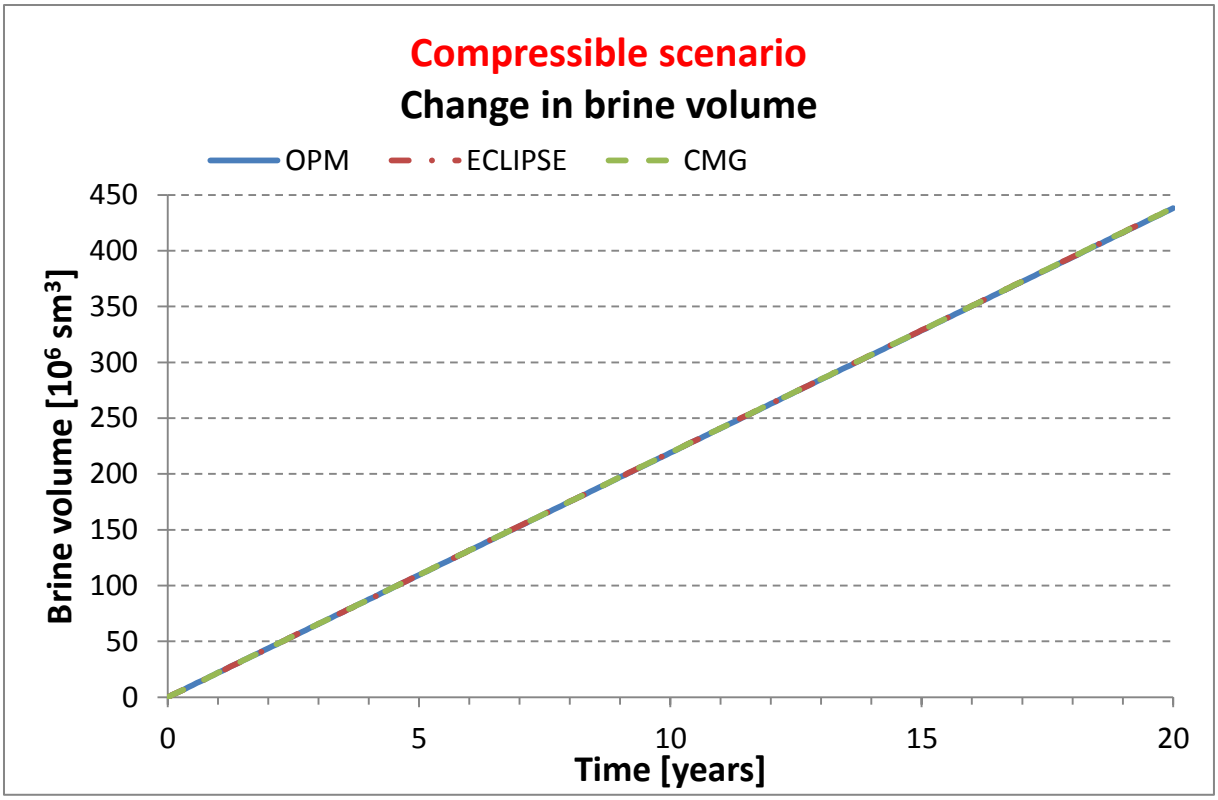

Figure 6.4: Cumulative brine production in the compressible model

6.3. Saturation profiles

The saturation distribution in layer 6, which is the topmost sand layer in the Johansen formation, determined by the simulators of Eclipse, IMEX and OPM were compared at various time steps: after 5, 10, 15 and 20 years of injection. The reason why the geometry looks different in OPM in the figures presented in section 6.3 and 6.4 is that it was not possible to define the layers explicitly in the input model for OPM, and as the uppermost 5 layers are impermeable layers CO_2 migration does not occur in them, thus they had to be made invisible so that the migration process occuring in the middle Johansen formation could be observed. In order to make this possible I applied a threshold on porosity in the program used for visualizing the output of OPM (which is called ParaView) to a minimum value of 11% which set all cells invisible which have a porosity value below 11%. The three small bubbles appearing in the left side of the model output of OPM are sand collocations of the Johansen formation into the shale of the Dunlin Group.

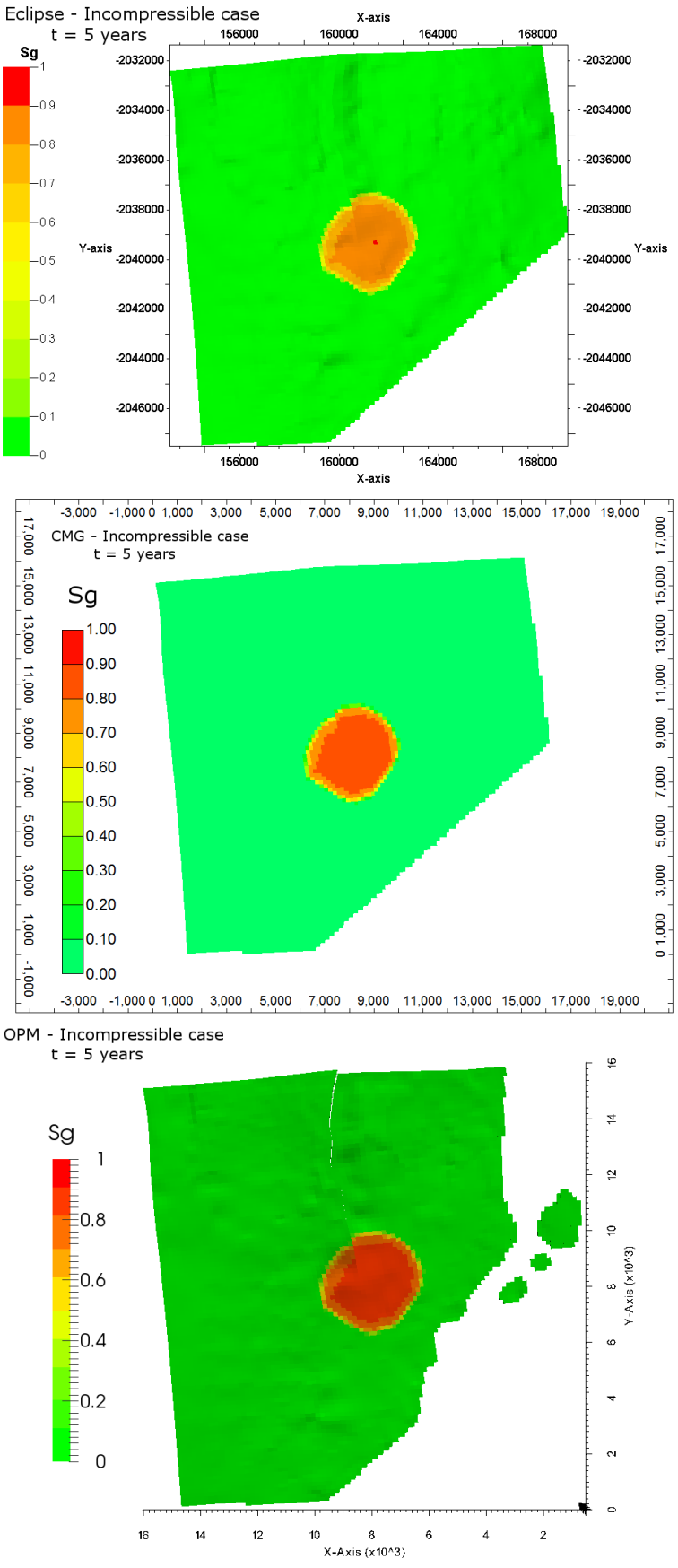

Figure 6.5: Gas saturation in the in the incompressible case at t=5 years

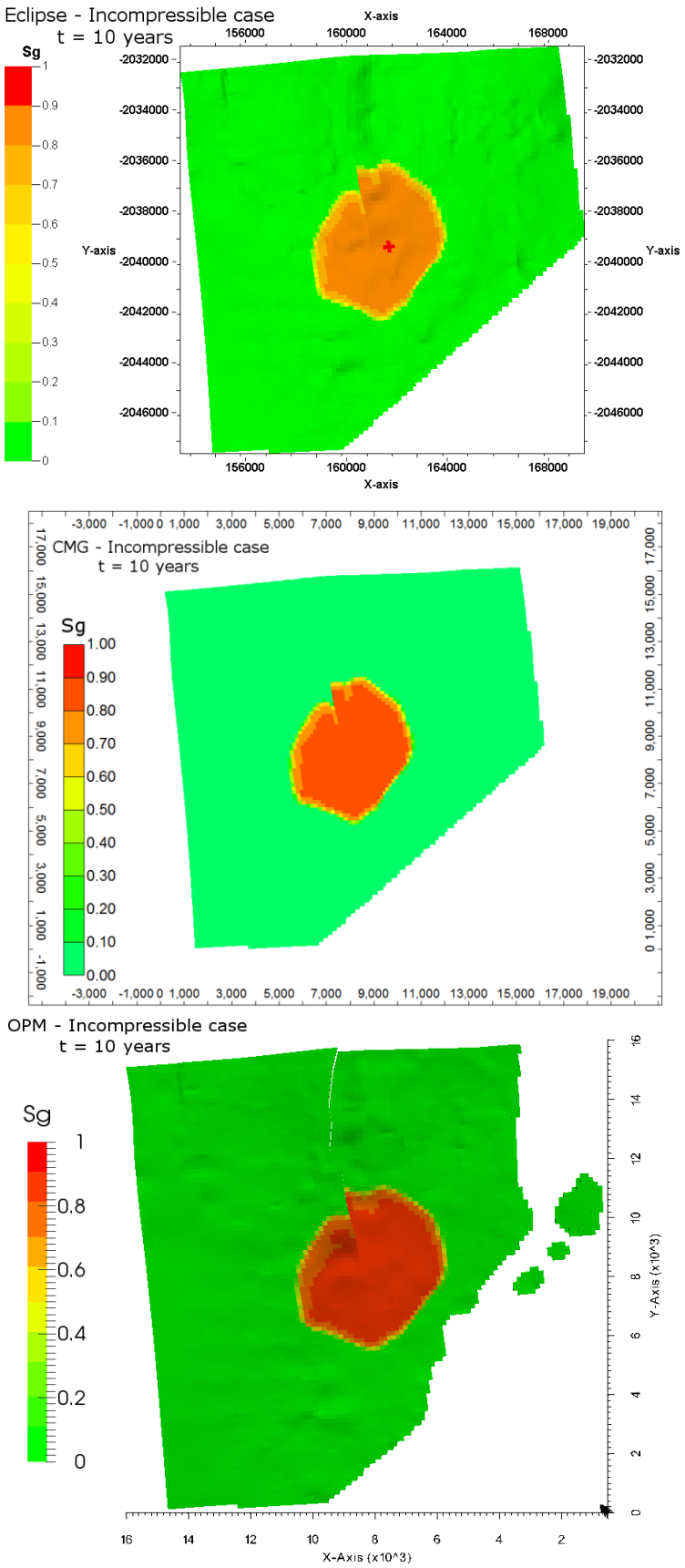

Figure 6.6: Gas saturation in the in the incompressible case at t=10 years

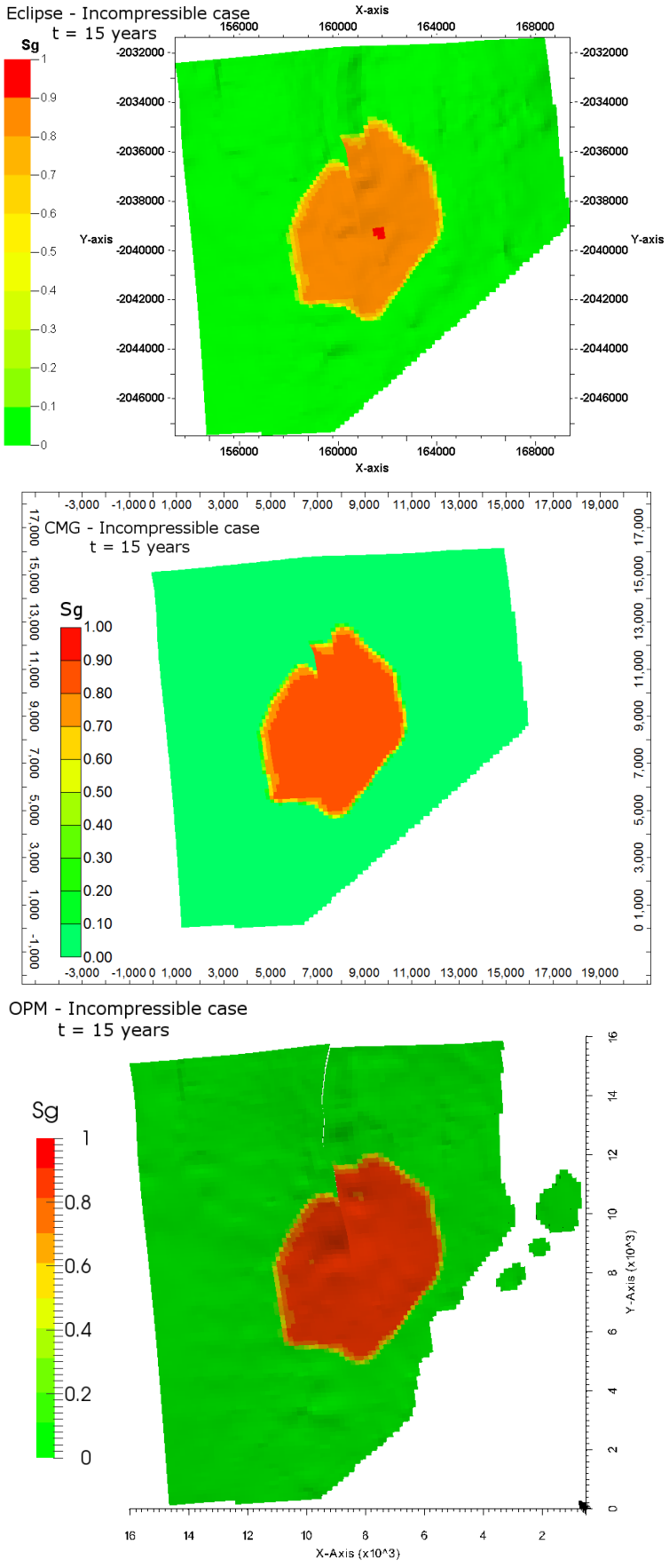

Figure 6.7: Gas saturation in the in the incompressible case at t=15 years

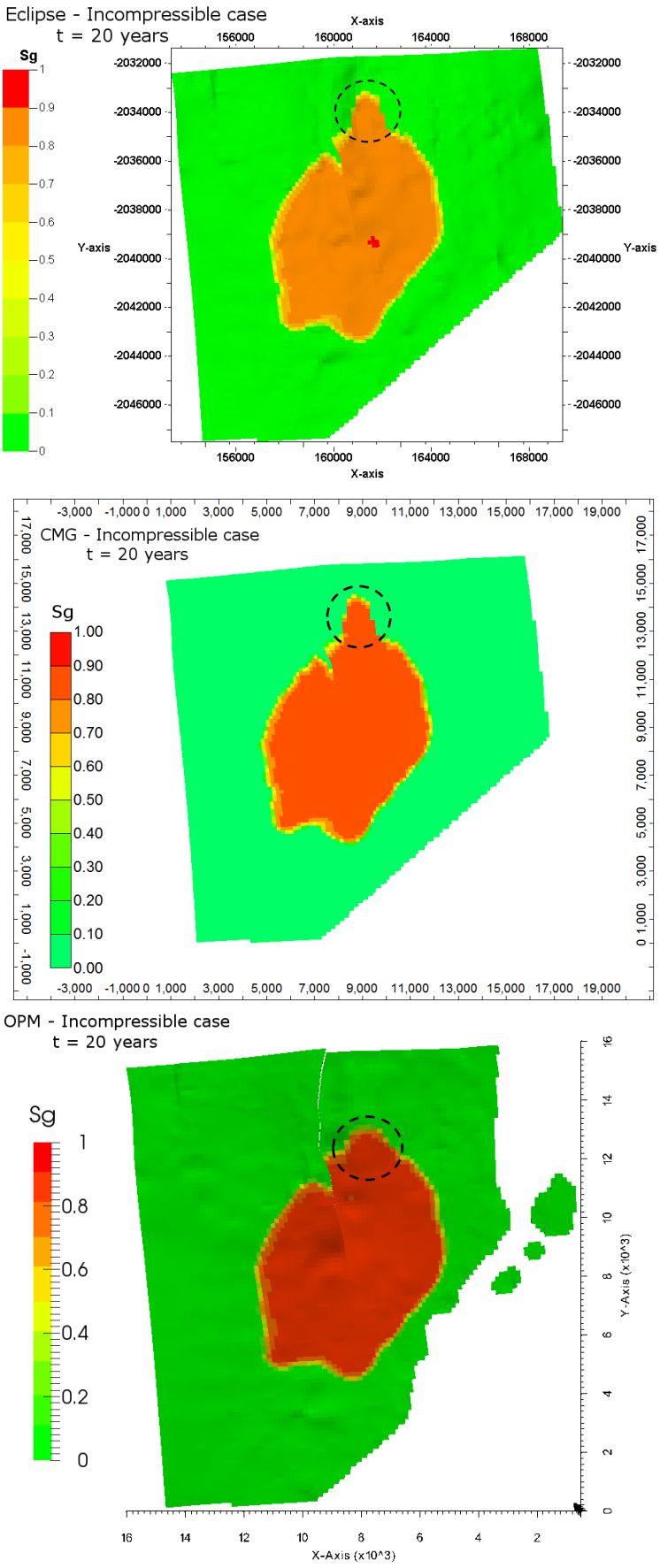

Figure 6.8: Gas saturation in the in the incompressible case at t=20 years

In the incompressible case, the shapes of the saturation distributions calculated (see Figure 6.5 – Figure 6.8) are similar. A minor difference in the saturation “foot prints” is visible at the last time step (20 years) in the region signed by the black circles in Figure 6.8. In this area the moving of the CO_2 front simulated by OPM seems to be a bit slower than in the cases of Eclipse and IMEX.

The changes of saturation allocations over time for the compressible CO_2 model are presented in Figure 6.9 - Figure 6.12 at the same time steps as in the incompressible scenario.

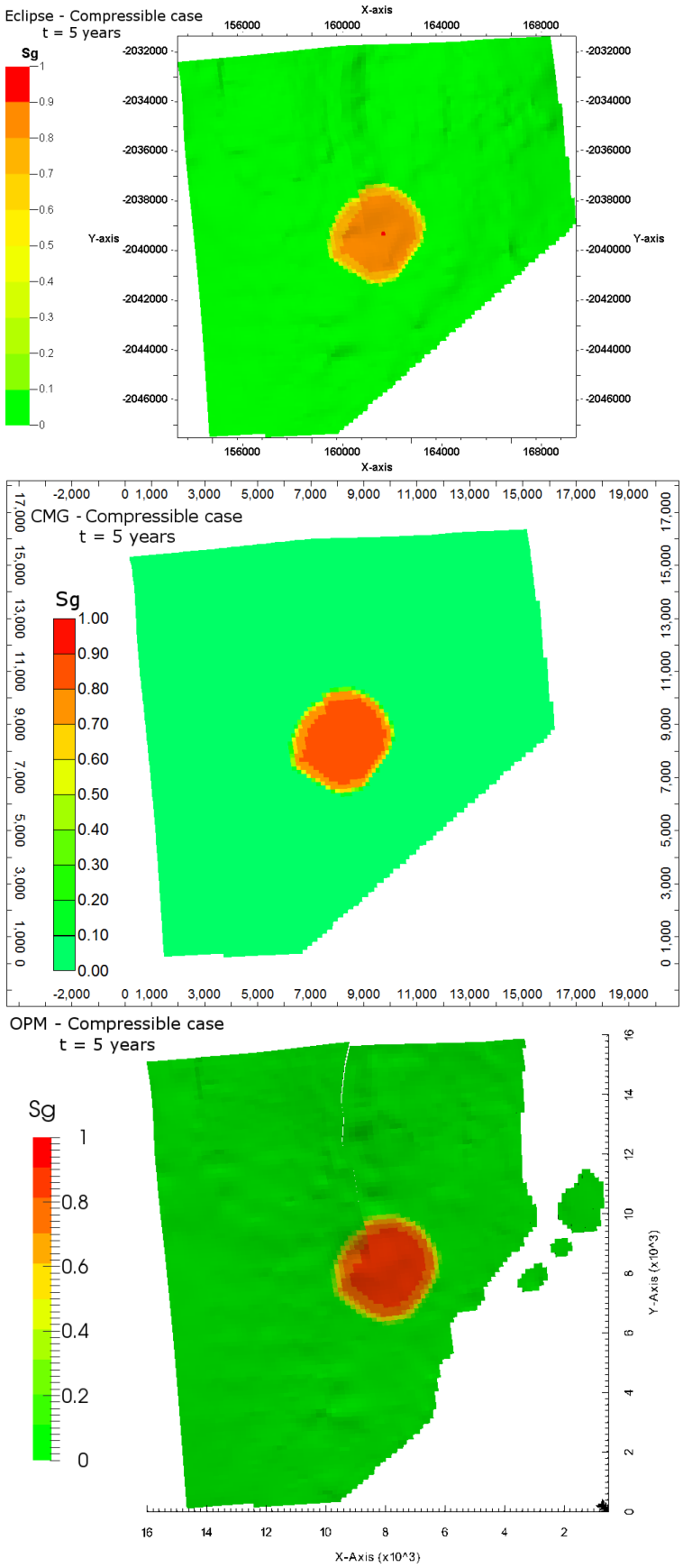

Figure 6.9: Gas saturation in the compressible case at t=5 years

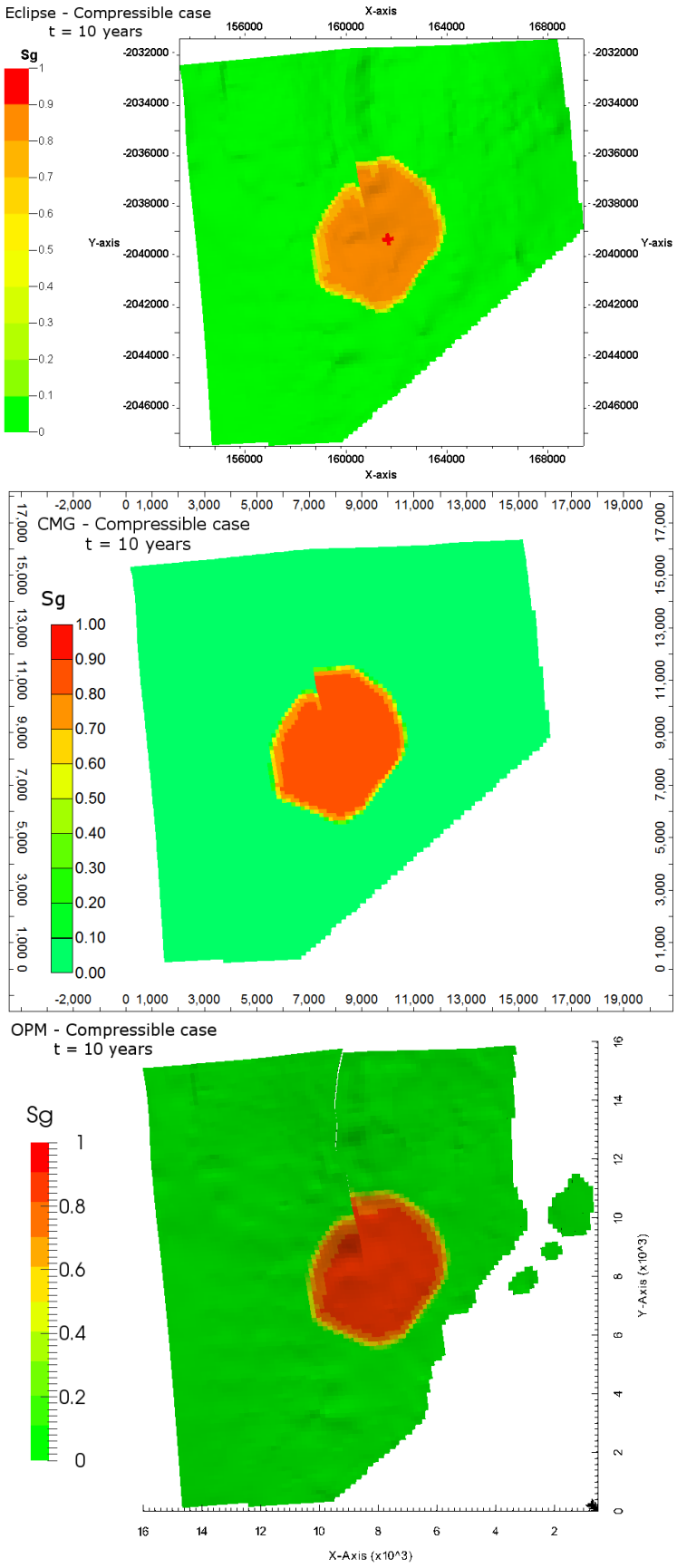

Figure 6.10: Gas saturation in the compressible case at t=10 years

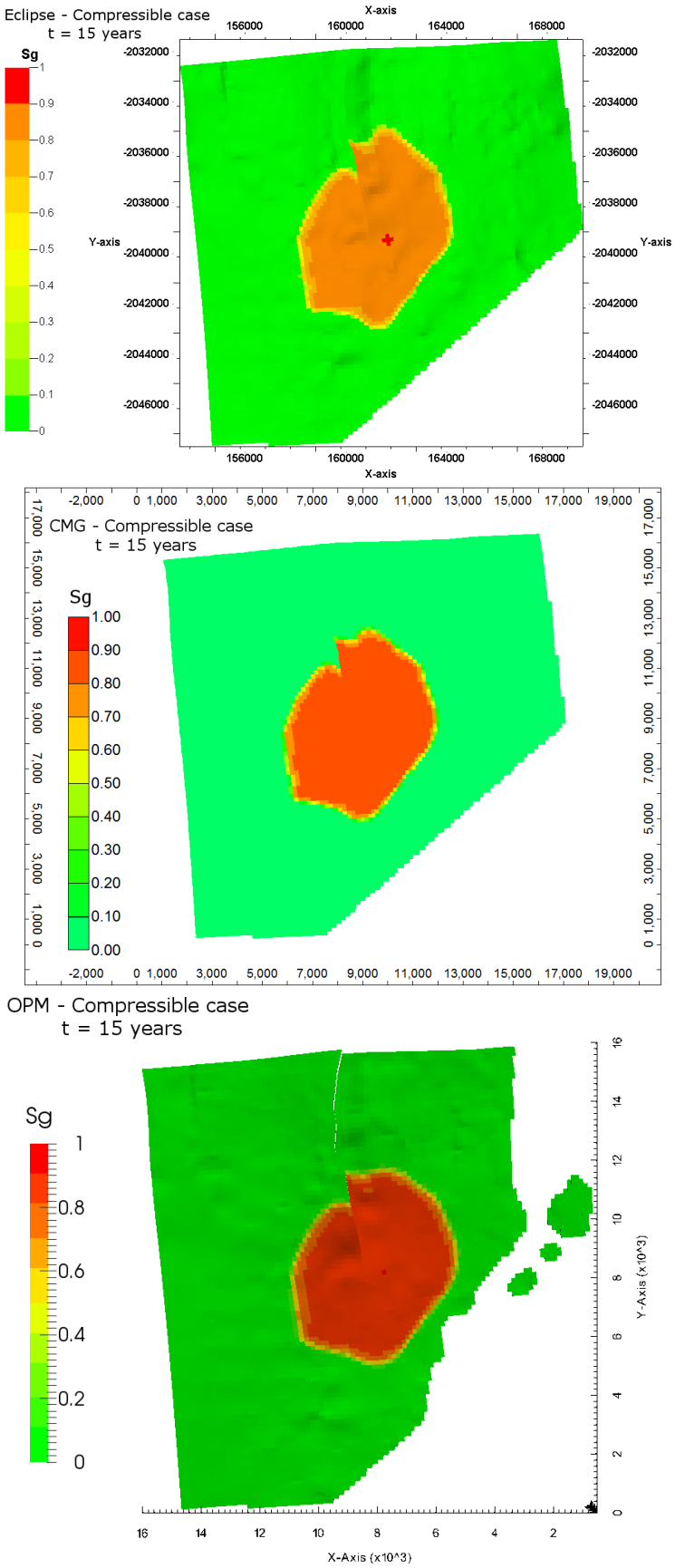

Figure 6.11: Gas saturation in the compressible case at t=15 years

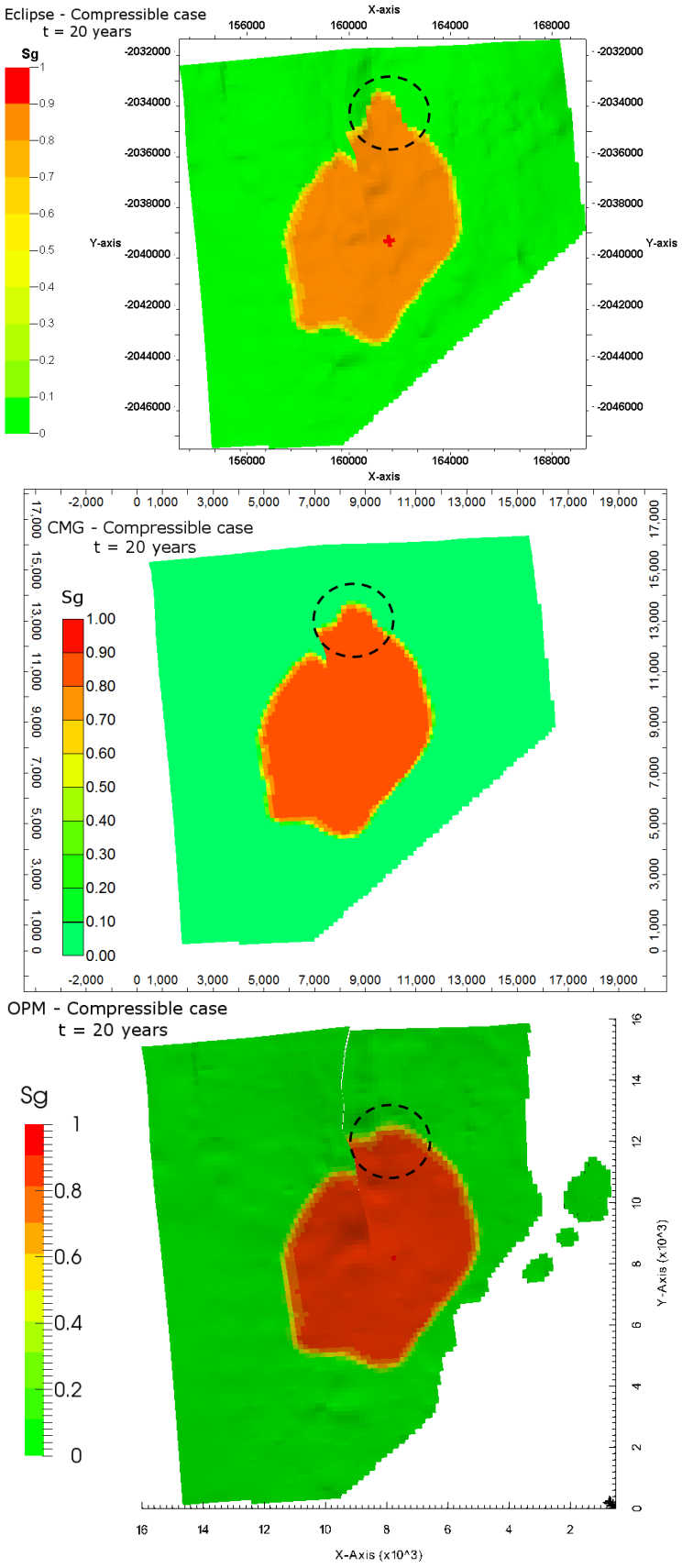

Figure 6.12: Gas saturation in the compressible case at t=20 years

In contrast to the incompressible case, the results of the transport process estimation exhibit more substantial alteration. CO_2 spreads further in the region indicated by the black circles in Figure 6.12.

6.4. Pressure profiles

By solving the diffusion equation described by Equation (2.15) in section 2.4 the average pressure at each grid block is calculated. For the incompressible subcase, this pressure distribution is illustrated in Figure 6.13 - Figure 6.16 and for the compressible subcase in Figure 6.17 - Figure 6.20.

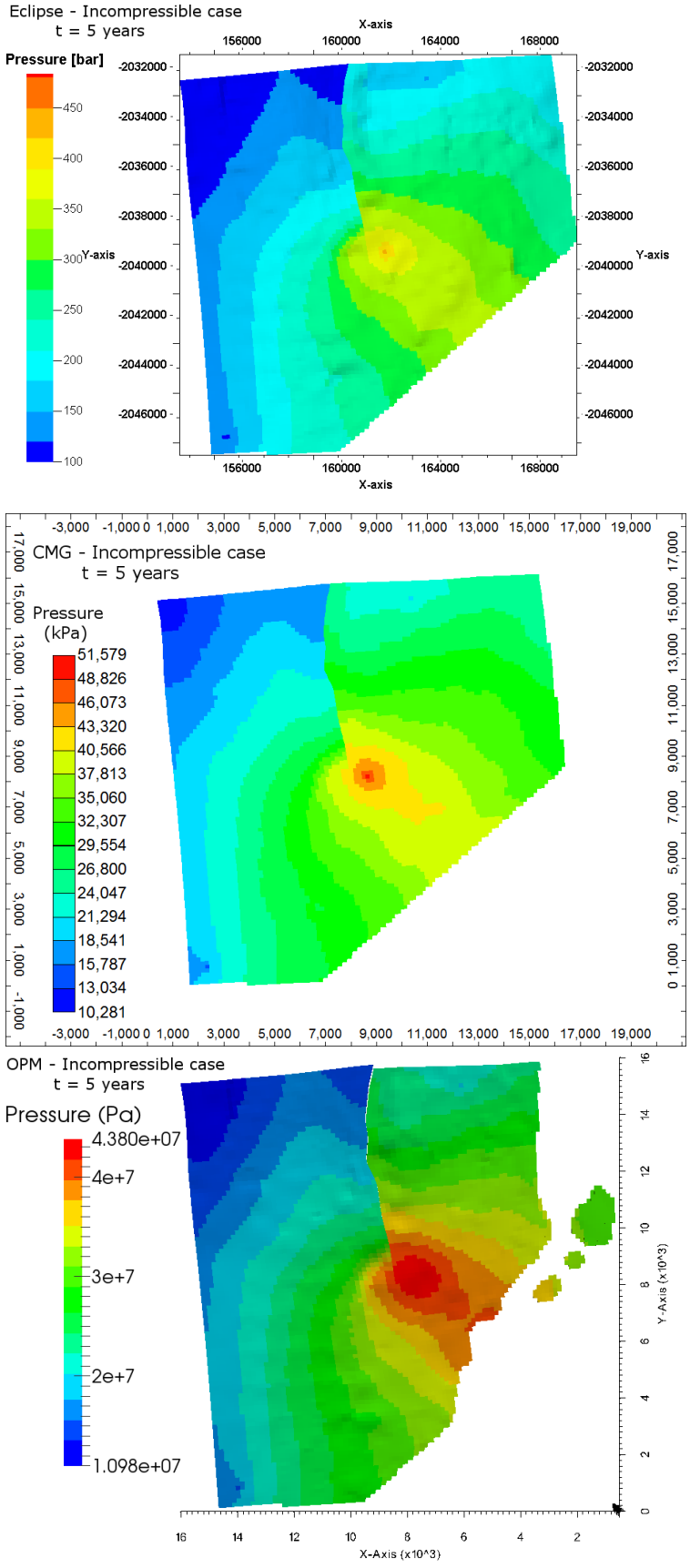

Figure 6.13: Pressure profile in the in the incompressible case at t=5 years

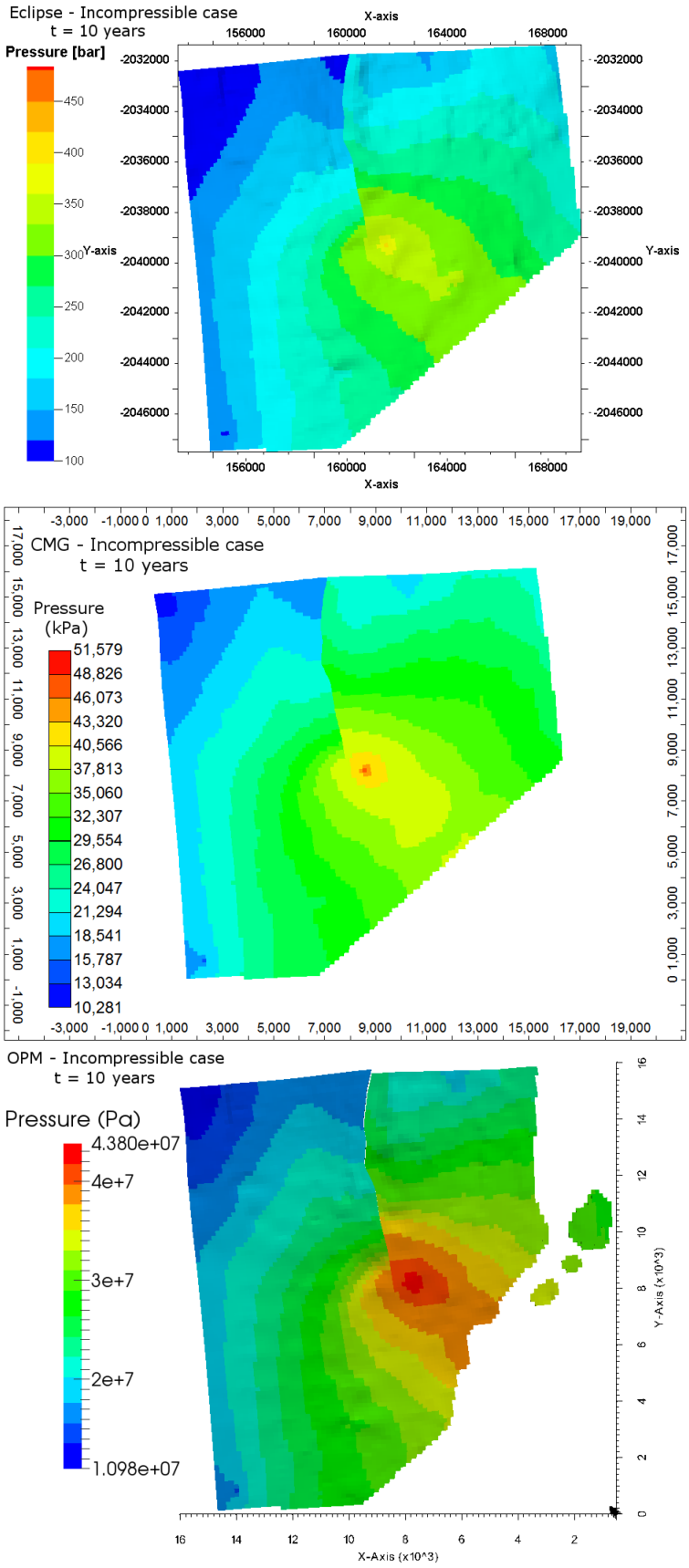

Figure 6.14: Pressure profile in the in the incompressible case at t=10 years

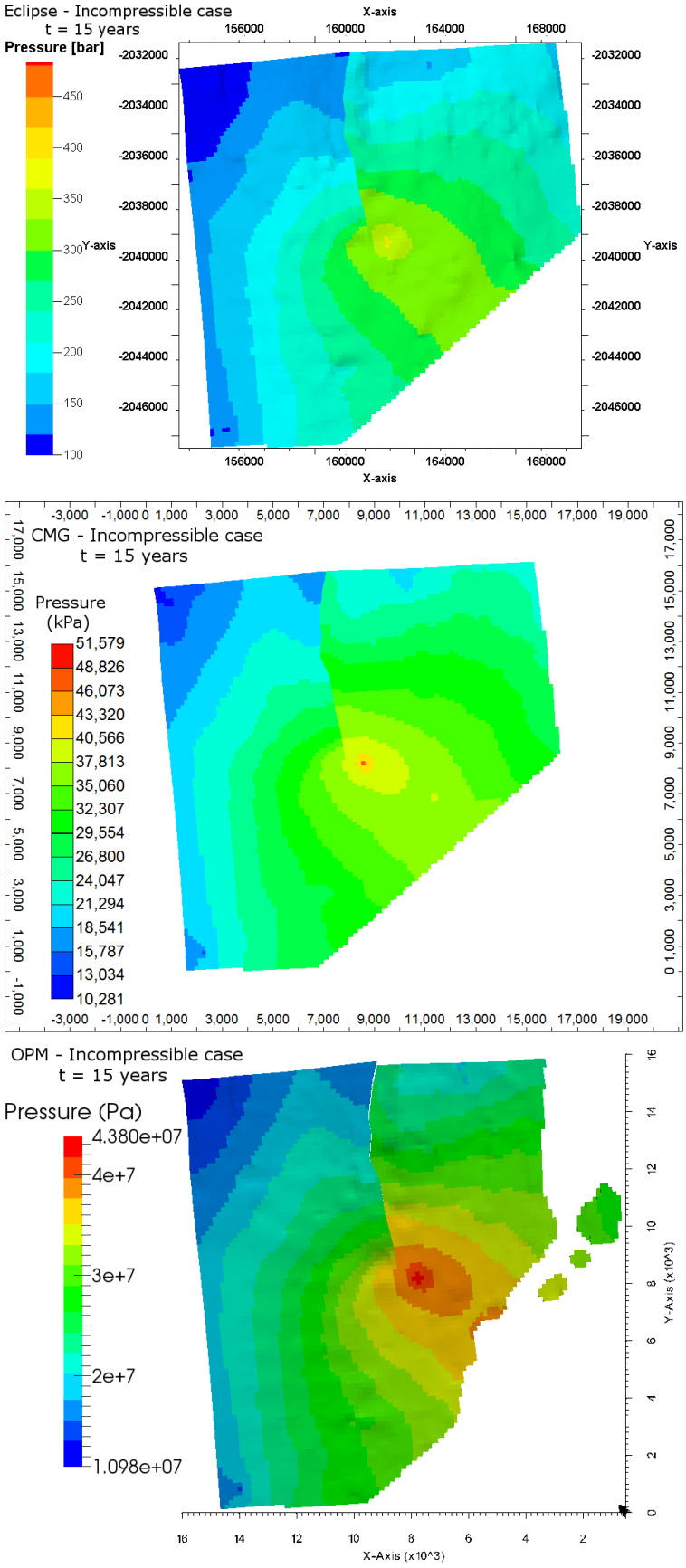

Figure 6.15: Pressure profile in the in the incompressible case at t=15 years

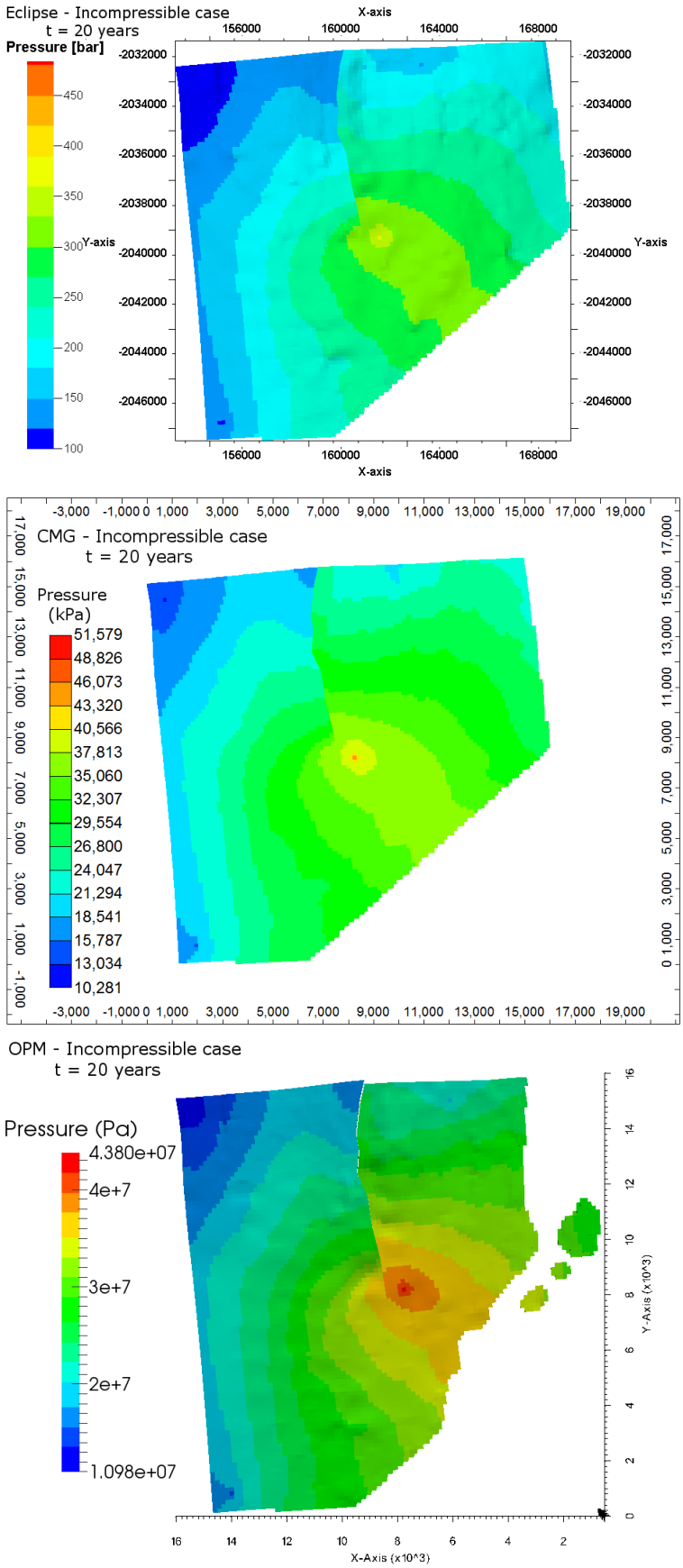

Figure 6.16: Pressure profile in the in the incompressible case at t=20 years

The shape of the pressure distribution determined by the three simulators are similar, however, deviation develops in the range of the pressure values and not in the shape of the distribution. Shortly after injection begins, pressure builds up in the middle of the domain around the injecting well then slowly decreases as CO_2 spreads deeper into the reservoir towards the producers. The minimum pressure occurs in areas close to producing wells. The ranges of the predicted pressure values are enlisted in Table 6.1.

Table 6.1: Pressure ranges in the incompressible scenario

Simulator	Pressure ranges [bar]
Eclipse	98 - 483
IMEX	103 - 516
OPM	109 - 438

The changes of the pressure profiles over time in the compressible case are illustrated in Figure 6.17 - Figure 6.20.

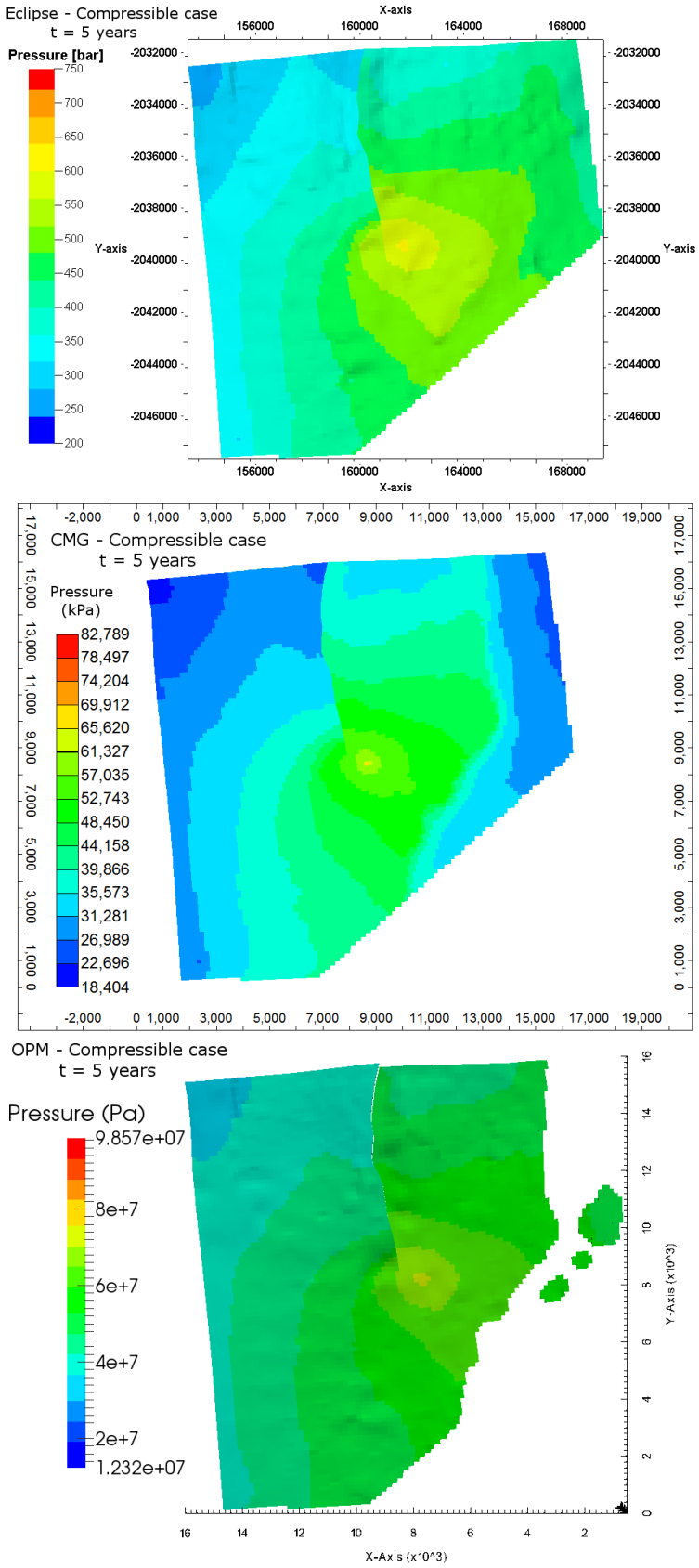

Figure 6.17: Pressure profile in the compressible case at t=5 years

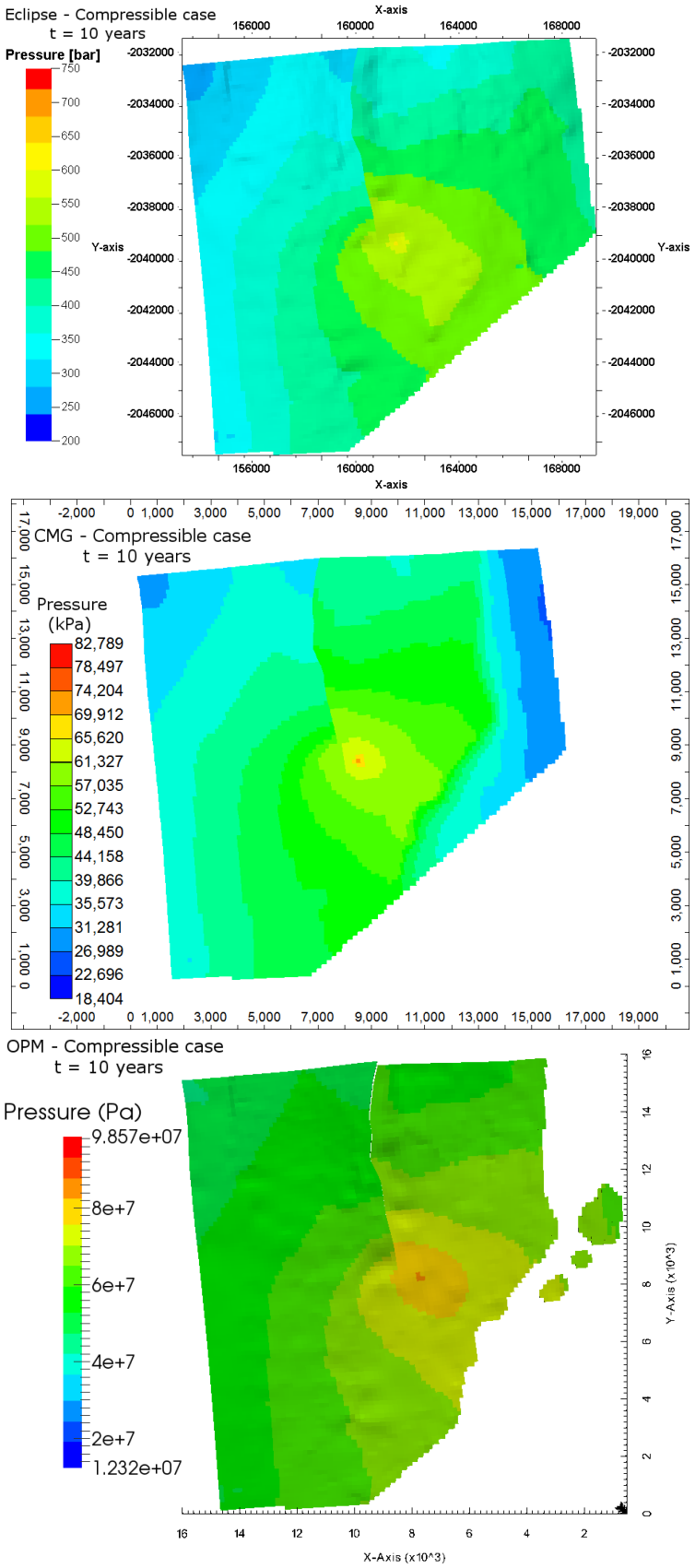

Figure 6.18: Pressure profile in the compressible case at t=10 years

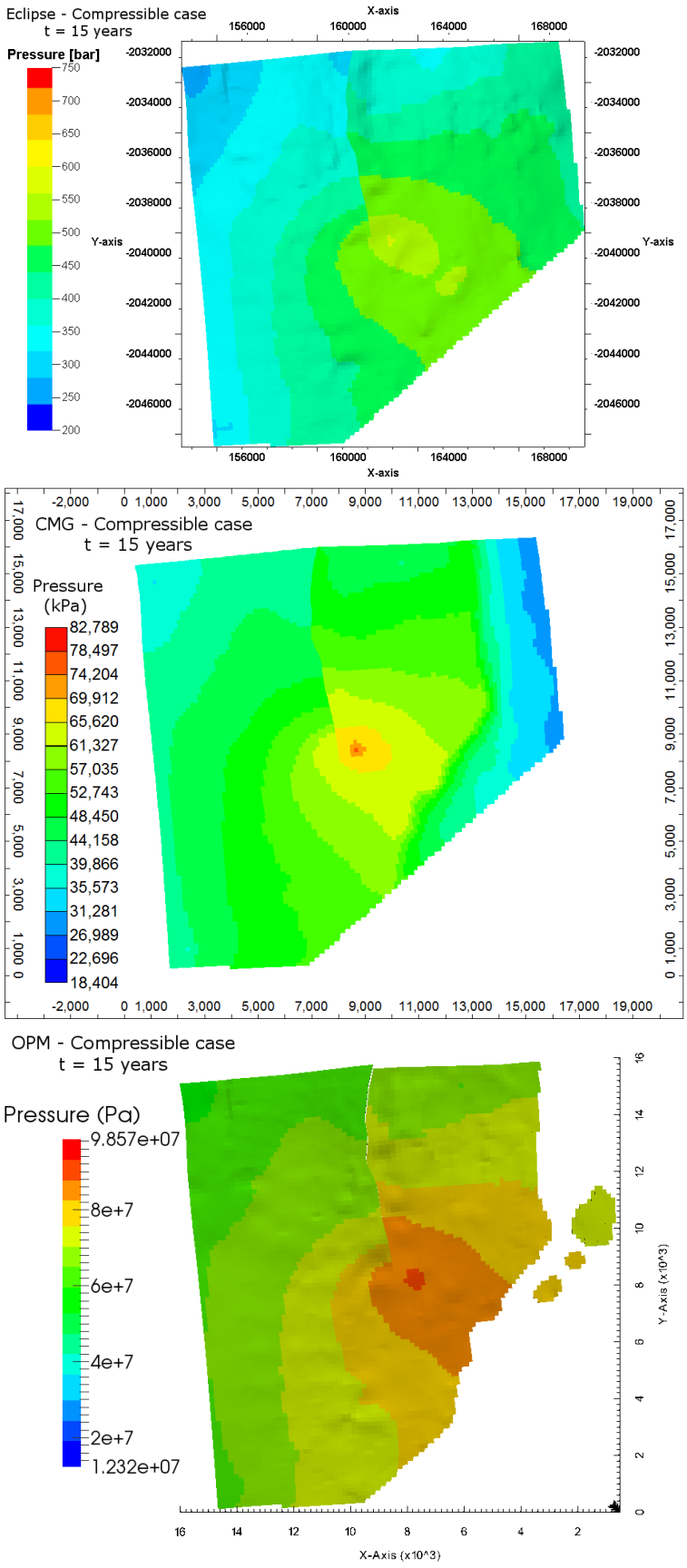

Figure 6.19: Pressure profile in the compressible case at t=15 years

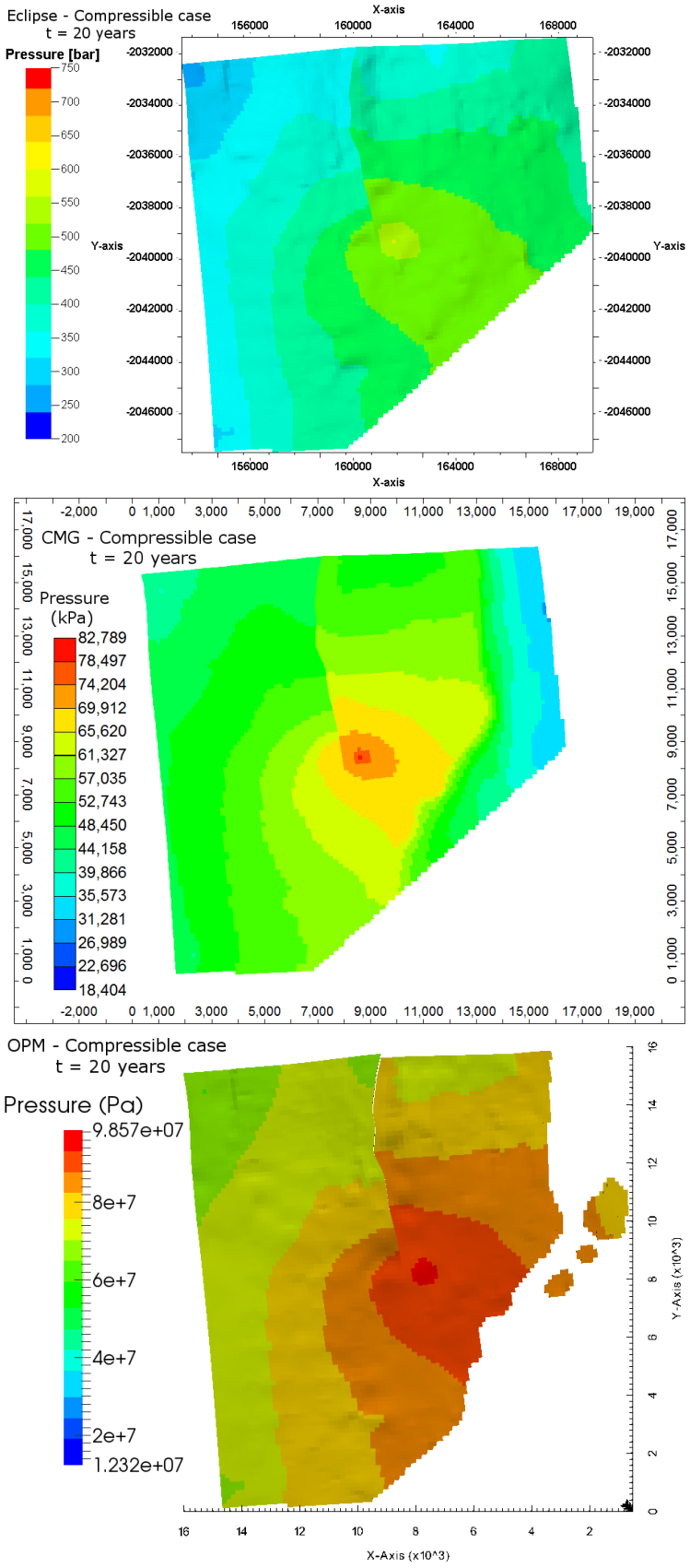

Figure 6.20: Pressure profile in the compressible case at t=20 years

In contrast to the incompressible case, major difference arises in the maximum values computed by the simulators when fluid compressibility is considered. As shown in Table 6.2 OPM estimated the highest pressure which emerged during the 20 years of CO_2 injection that is more than two times greater than the maximum pressure predicted by Eclipse with the narrowest pressure range.

Table 6.2: Pressure ranges in the compressible scenario

Simulator	Pressure range [bar]
Eclipse	184 - 712
IMEX	184 - 828
OPM	184 - 985

This difference is a consequence of applying different solution methods for the non-linear problem and the results are also severely affected by the fact that in OPM the CO_2 compressibility is a constant value, while in Eclipse and IMEX, it is a function of pressure and was set as a linear function with a gradient close to zero in order to make the fluid models as similar as possible. (Computer Modelling Group Ltd., 2013), (Schlumberger Ltd., 2011), (Rustad, 2013)

6.5. Computational time

In Table 6.3, the computational time of the used simulator software tools are summarized. In column 4 the CPU time needed for the prescribed process were compared with respect to the fastest simulator.

Table 6.3: Computational time of the simulations

Simulator	CPU [s]	CPU [min]	Relative CPU
Incompressible case			
Eclipse	940.0	15.67	180%
IMEX	521.6	8.69	100%
OPM	8336.0	138.93	1598%
Compressible case			
Eclipse	681.0	11.35	149%
IMEX	455.9	7.60	100%
OPM	8432.6	140.54	1850%

As shown in Table 6.3, for both introduced benchmark cases, the fastest simulation was executed by IMEX, while Eclipse ran the simulation in about 1.5 times slower. In comparison to these values, OPM, which is a relatively young, academic open source software with a development history of 7 years, performed the same simulation task in roughly 18 times slower as it needed 140 minutes, more than 2 hours. This large difference in the computational time is likely caused by the

underlying mathematical formulation of the model and its code implementation. One significant difference in the mathematical formulation which has significant impact on the computational time is that OPM solves the two governing equations – the saturation equation and the pressure equation – in a decoupled manner, while the commercial simulators apply a fully implicit scheme. A fully implicit scheme means that these two equations are solved simultaneously at a given time step, whereas in decoupled implicit scheme the equations are solved sequentially, first the pressure equation, then the saturation equation.

Another factor affecting the computational time is that Eclipse and IMEX are commercial software with more than 30 years of development history, where developers also concentrated on making the code work faster after the implementation of the underlying mathematical formulations were done. However OPM is in a development phase, where most developers still focus on increasing the capabilities of the code by including more features.

7. Conclusion

The purpose of my master thesis research was to propose a benchmark problem related to CO_2 sequestration in an existing geological formation. The suggested model is based on the real site data of the Johansen formation that is a potential field located offshore in Norway for CO_2 storage. I recommended three simulation software with capabilities to model advection-diffusion transport processes in a porous medium: Eclipse, IMEX and OPM.

The features of the numerical simulators that I consider important mentioning, are summarized in Table 7.1.

Table 7.1: Features of numerical simulators

	Eclipse	**IMEX**	**OPM**
Spatial discretization method	Finite difference method	Finite difference method	Finite volume – Two-point Flux approximation
Temporal discretization method	Fully Implicit Euler scheme	Fully Implicit Euler scheme	Decoupled Implicit Euler Scheme
Non-linear solution scheme	Newton iteration	Newton iteration	Reordered Gauss-Seidel iteration
Linear solver approach	Orthomin method	Generalized Minimum Residual method	Unsymmetric Multifrontal method

As the very same corner-point grid was used as a discretized model domain, the effect of implementing different spatial discretization methods into the software code is minimized.

Since all simulators apply implicit Euler scheme, time discretization is also assumed to not affect the results. However the different code implementation of this implicit method could have an impact on the computational time. Another factor affecting the computational time is that Eclipse and IMEX are commercial software with more than 30 years of development history, where developers also concentrated on making the code work faster after the implementation of the underlying mathematical formulations were done. However OPM is in a development phase, where most developers still focus on increasing the capabilities of the code by including more features.

Both subcases in the proposed Johansen benchmark are non-linear problems. The simulators use different solution approaches to linearize the equation system and each of them applies unique techniques to solve (i.e. iteratively or directly) the

resulting algebraic system. The underlying mathematical formulation also generates differences in the results which are somewhat more evident in a more complex scenario as the compressible subcase. Among the possible simulation outputs I compared the changes in the amount of the phases in the reservoir, the saturation profile and the pressure distribution over time. Generally, in the incompressible scenario all compared parameters yield similar results. On the other hand, when CO_2 compressibility is considered, the differences appearing among the computed pressure values are more evident. The alteration visible among the compared results are the consequences of the previously described differences in the mathematical solution methods implemented into the code of the applied reservoir simulators. Another important factor affecting the results in the compressible case is the different fluid model implementation.

In conclusion, this thesis made contribution in advancing the field of geological CO_2 storage by proposing a benchmark problem based on real site data. The two commercial simulators used for the modelling purposes are commonly used software in CCS with advanced modules implemented to simulate different processes arising during CO_2 injection yielding reliable results. In my opinion, OPM is not yet in a phase which is fully capable at simulations in fields related to CCS as it is lacking in the formulation of modelling fully compressible gas phase, but the two-phase incompressible and the slightly compressible codes produced reliable solutions. Further efforts may be done to develop the proposed benchmark by including capillary effects, expand it to fully compressible fluid flow when this feature is implemented in OPM or by using other potential simulators in the field of carbon capture and storage.

References

Barnett, C., 2015. *Groundwater Wake-up.* [Online]
Available at: http://ensia.com/features/groundwater-wake-up/
[Accessed 31 May 2015].

Beyer, C. et al., 2012. Modelling CO2-induced fluid–rock interactions in the Altensalzwedel gas reservoir. Part II: coupled reactive transport simulation. *Environmental Earth Sciences,* 67(2), pp. 573-588.

Böttcher, N. et al., 2012. Evaluation of thermal equations of state for CO2 in numerical simulations. *Environmental Earth Sciences,* 67(2), pp. 481-495.

Causon, D. M., Mingham, C. G. & Qian, L., 2011. *Introductory Finite Volume Methods for PDEs.* 1st ed. Manchester: Ventus Publishing ApS.

Celia, M. A. et al., 2005. Quantitative estimation of CO2 leakage from geological storage: Analytical models, numerical models, and data needs. *Greenhouse Gas Control Technologies,* 7(1), pp. 663-671.

Celia, M. A. & Gray, W. G., 1992. *Numerical methods for differential equations : fundamental concepts for scientific and engineering applications.* 1st ed. New Jersey: Prentice-Hall.

Chen, Z. & Zhang, Y., 2009. Well flow models for various numerical methods. *International Journal of Numerical Analysis and Modeling,* 6(3), pp. 375-388.

Class, H. et al., 2009. A benchmark study on problems related to CO2 storage in geologic formations. *Computational Geosciences,* 13(4), pp. 409-434.

Computer Modelling Group Ltd., 2013. *IMEX Manual.* Calgary: s.n.

Dahle, H. K., 2009. *The Johansen Data Set.* [Online]
Available at: https://www.sintef.no/projectweb/matmora/downloads/johansen/
[Accessed 22 May 2014].

Davis, T. A. & Duff, I. S., 1993. *An unsymmetric-pattern multifrontal method for sparse LU factorization,* Gainesville: University of Florida.

De Lucia, M. et al., 2012. Modelling CO2-induced fluid–rock interactions in the Altensalzwedel gas reservoir. Part I: from experimental data to a reference geochemical model. *Environmental Earth Sciences,* 67(2), pp. 563-572.

Deuflhard, P., 2011. *Newton Methods for Nonlinear Problems.* 1st ed. Berlin: Springer.

Ebigbo, A., Class, H. & Helmig, R., 2007. CO2 leakage through an abandoned well: problem-oriented benchmarks. *Computational Geosciences,* 11(2), pp. 103-115.

Eigestad, G. T. et al., 2009. Geological modeling and simulation of CO2 injection in the Johansen formation. *Computational Geosciences,* 13(4), pp. 435-450.

Eymard, R., Herbin, R. & Gallouet, T., 2010. *Finite Volume Method.* [Online]
Available at: http://www.scholarpedia.org/article/Finite_volume_method
[Accessed 25 February 2015].

Global CCS Institute, 2014. *The Global Status of CCS,* Melbourne: Global CCS Institute.

Greenbaum, A., 1987. *Iterative Methods for Solving Linear Methods.* 1st ed. Philadelphia: SIAM: Frontiers in Applied Mathematics.

Heinemann, Z., 2005. *Fluid Flow in Porous Media.* 1st ed. Leoben: Montanuniversität Leoben.

Heinemann, Z., 2013. *Introduction to Reservoir Simulation.* 1st ed. Leoben: Montanuniversität Leoben.

Hou, Z. et al., 2012. Development of a long-term wellbore sealing concept based on numerical simulations and in situ-testing in the Altmark natural gas field. *Environmental Earth Sciences,* 67(2), pp. 395-409.

Humez, P. et al., 2011. Modeling of CO2 leakage up through an abandoned well from deep saline aquifer to shallow fresh groundwaters. *Transport in Porous Media,* 90(1), pp. 153-181.

Kolditz, O. et al., 2012. A systematic benchmarking approach for geologic CO2 injection and storage. *Environmental Earth Sciences,* 67(2), pp. 613-632.

Le Quéré, C. et al., 2013. *Global Carbon Project,* Oak Ridge: CDIAC Data.

Lee, S. H., Wolfsteiner, C. & Tchelepi, H. A., 2008. Multiscale finite-volume formulation for multiphase flow in porous media: black oil formulation of compressible, three-phase flow with gravity. *Computational Geosciences,* 12(3), pp. 351-366.

Nordbotten, J. M., Celia, M. A. & Bachu, S., 2005b. Injection and storage of CO2 in deep saline aquifers: Analytical solution for CO2 plume evolution during injection. *Transport in Porous Media,* 58(3), pp. 339-360.

Nordbotten, J. M., Celia, M. A., Bachu, S. & Dahle, H. K., 2005a. Semianalytical solution for CO 2 leakage through an abandoned well. *Environmental Science & Technology,* 39(2), pp. 602-611.

Nordbotten, J. M. & Dahle, H. K., 2011. Impact of the capillary fringe in vertically integrated models for CO2 storage. *Water Resources Research,* 47(2), pp. 537-547.

Osman, P., 2007. *climate & energy.* [Online]
Available at: http://www.energysustained.com/managing_impacts.htm
[Accessed 21 March 2015].

Rustad, A. B., 2013. *The Open Porous Media Initiative.* [Online]
Available at: http://www.opm-project.org/
[Accessed 10 September 2014].

Schlumberger Ltd., 2011. *ECLIPSE Technical Discription.* Houston: s.n.

Singh, A. K. et al., 2012. Numerical analysis of thermal effects during carbon dioxide injection with enhanced gas recovery: a theoretical case study for the Altmark gas field. *Environmental Earth Sciences,* 67(2), pp. 497-509.

Wei, L. & Saaf, F., 2009. Estimate CO2 storage capacity of the Johansen formation: numerical investigations beyond the benchmarking exercise. *Computational Geosciences,* 13(4), pp. 451-467.

Appendix

Appendix A

Porosity distribution of all layers in the Johansen formation

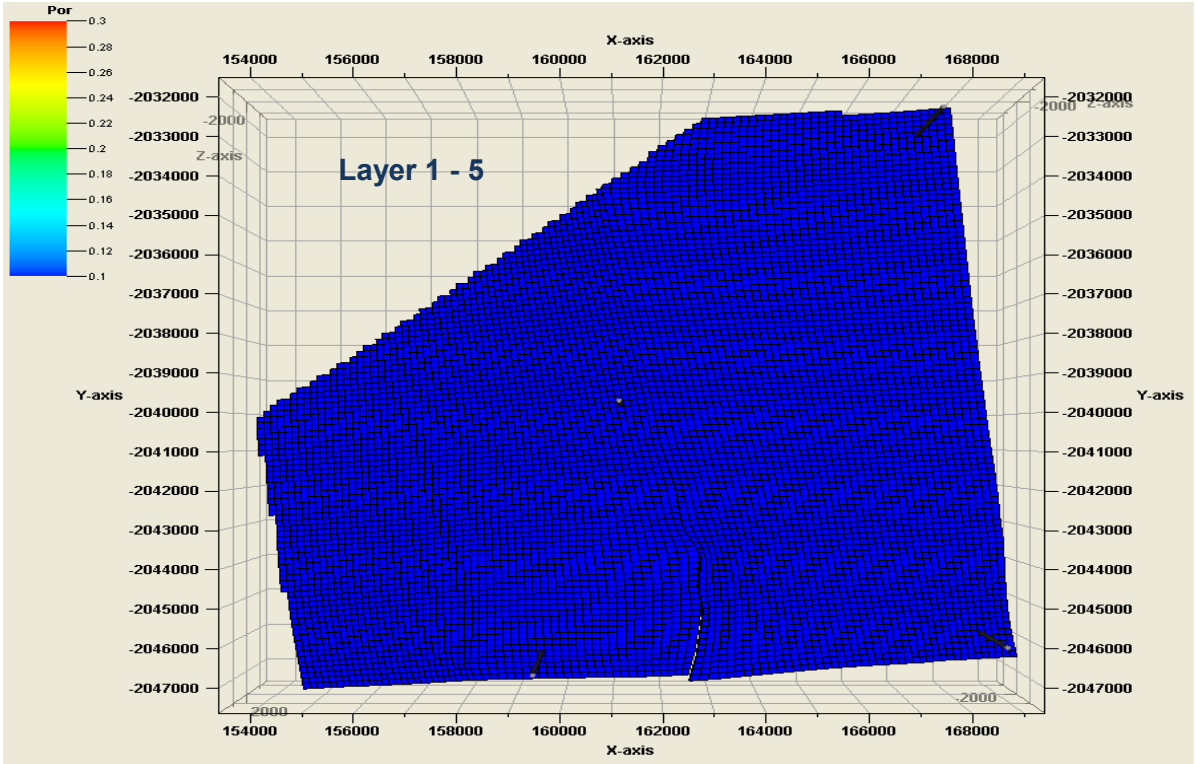

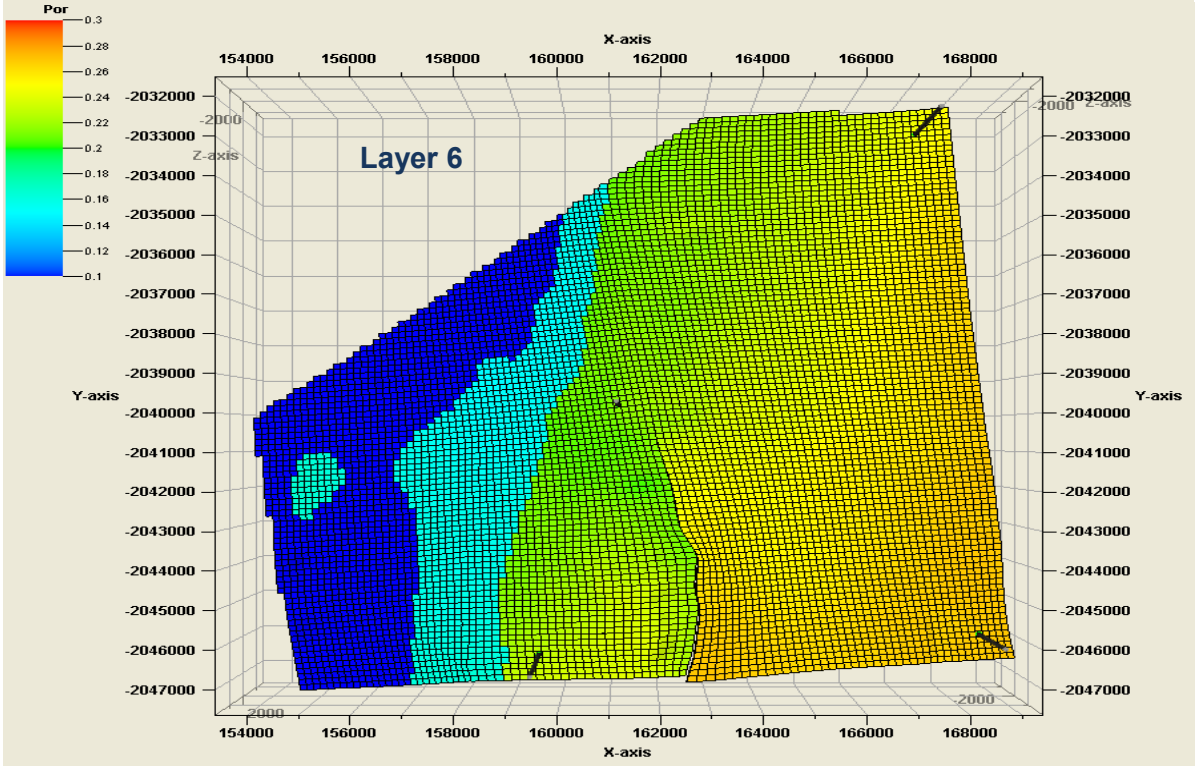

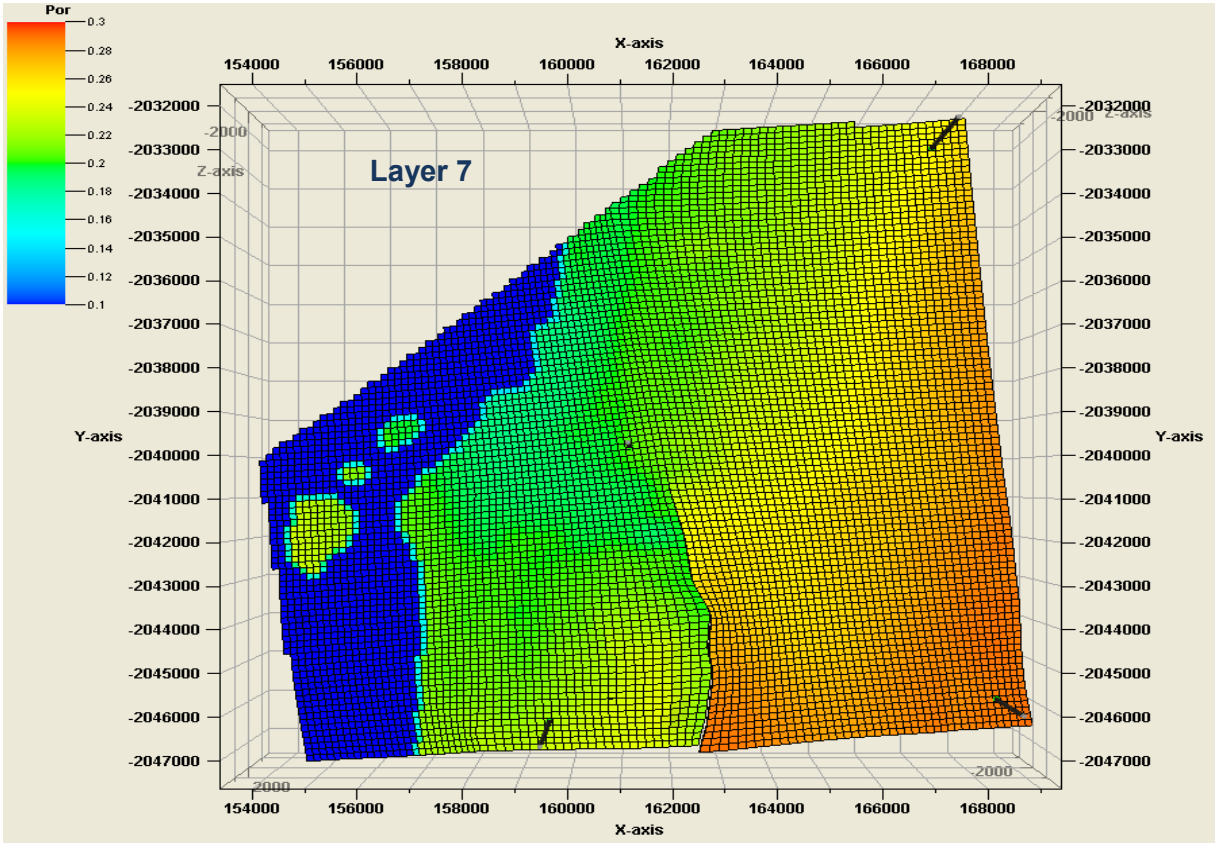
Por
0.3
0.28
0.26
0.24
0.22
0.2
0.18
0.16
0.14
0.12
0.1
X-axis
154000
156000
158000
160000
162000
164000
166000
168000
Y-axis
-2032000
-2033000
-2034000
-2035000
-2036000
-2037000
-2038000
-2039000
-2040000
-2041000
-2042000
-2043000
-2044000
-2045000
-2046000
-2047000
Z-axis
-2000
2000
Layer 7

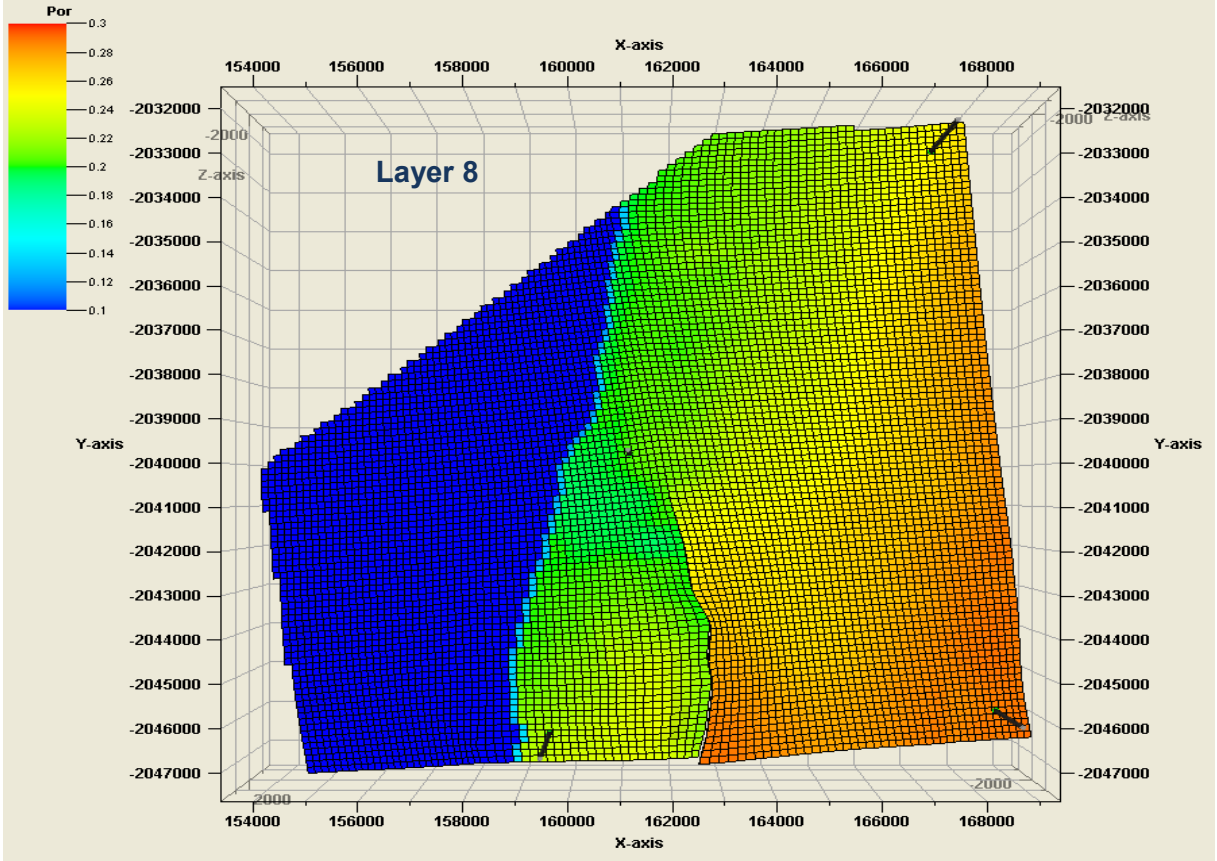
Por
0.3
0.28
0.26
0.24
0.22
0.2
0.18
0.16
0.14
0.12
0.1
X-axis
154000
156000
158000
160000
162000
164000
166000
168000
Y-axis
-2032000
-2033000
-2034000
-2035000
-2036000
-2037000
-2038000
-2039000
-2040000
-2041000
-2042000
-2043000
-2044000
-2045000
-2046000
-2047000
Z-axis
-2000
2000
Layer 8

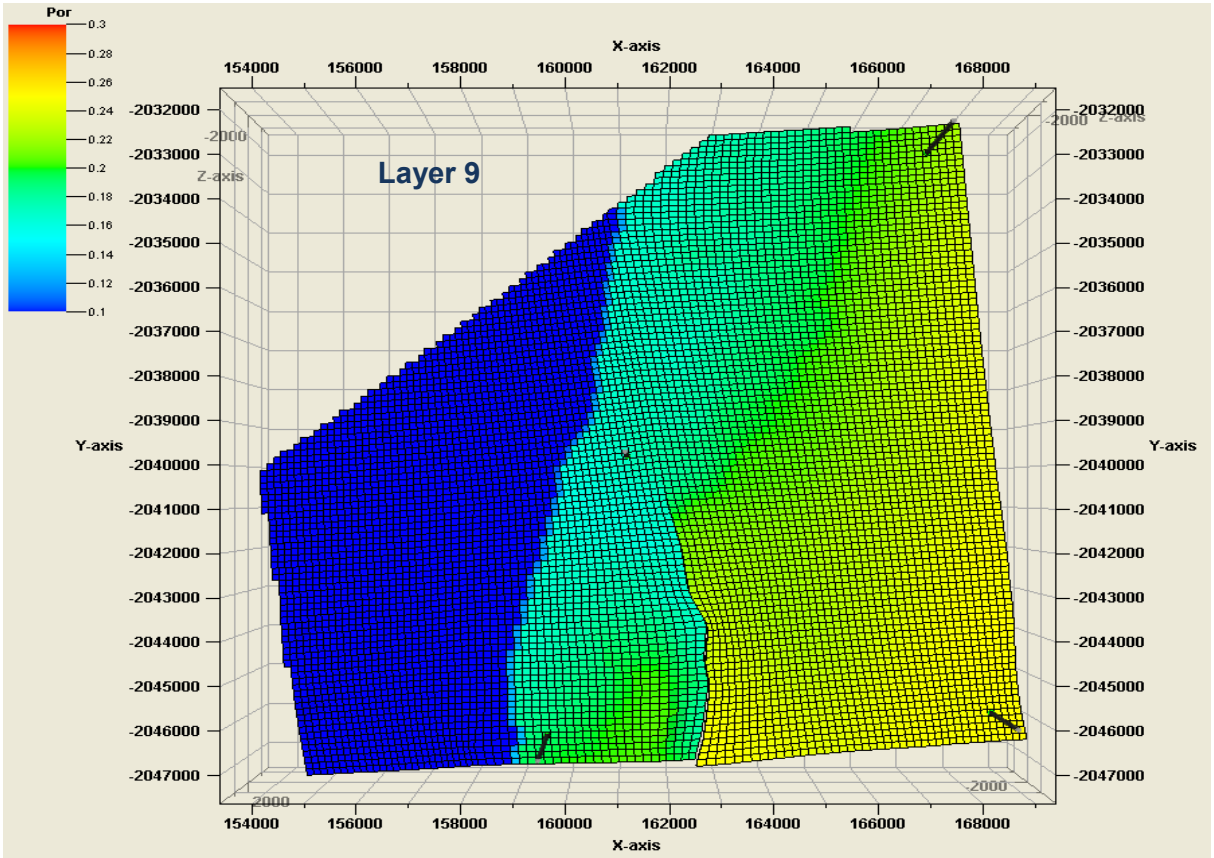
Por
0.3
0.28
0.26
0.24
0.22
0.2
0.18
0.16
0.14
0.12
0.1
X-axis
154000
156000
158000
160000
162000
164000
166000
168000
Y-axis
-2032000
-2033000
-2034000
-2035000
-2036000
-2037000
-2038000
-2039000
-2040000
-2041000
-2042000
-2043000
-2044000
-2045000
-2046000
-2047000
Z-axis
-2000
2000
Layer 9

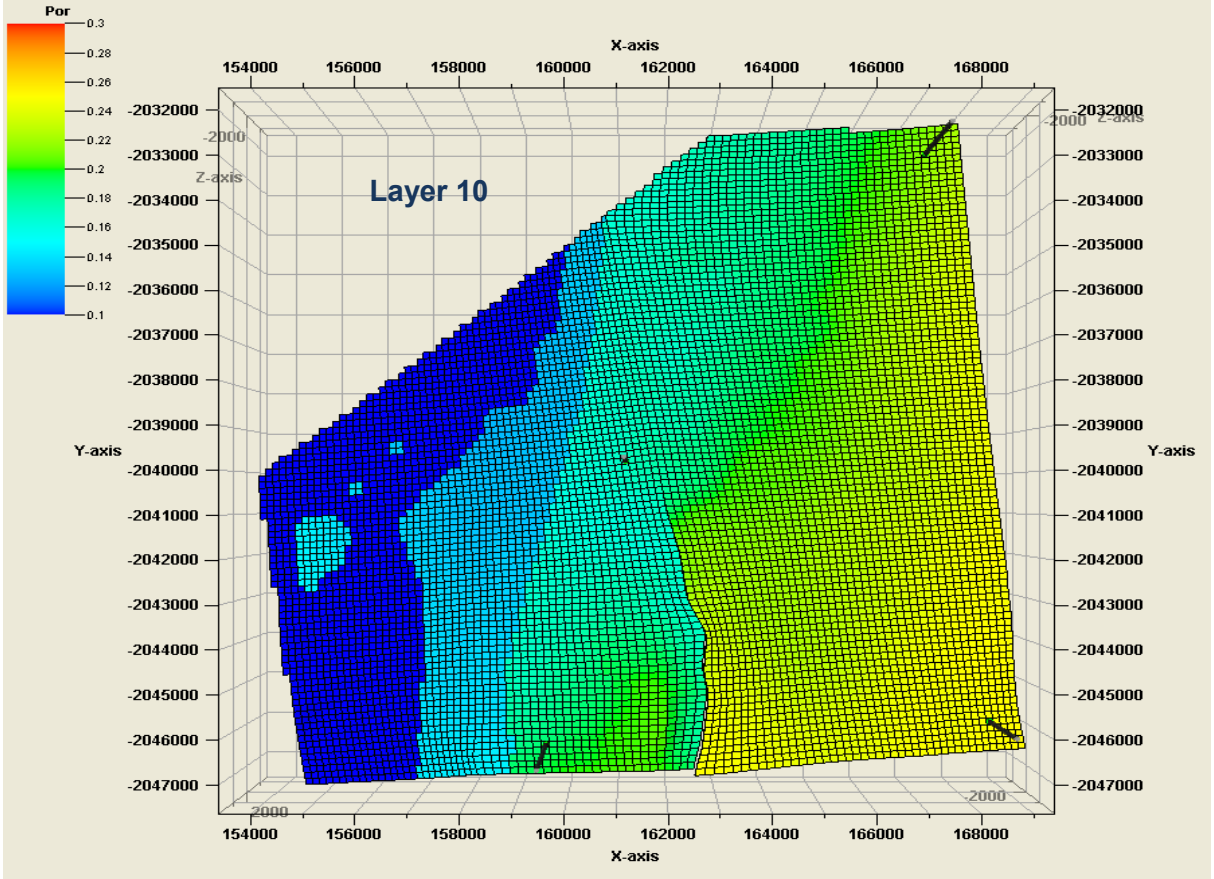
Por
0.3
0.28
0.26
0.24
0.22
0.2
0.18
0.16
0.14
0.12
0.1
X-axis
154000
156000
158000
160000
162000
164000
166000
168000
Y-axis
-2032000
-2033000
-2034000
-2035000
-2036000
-2037000
-2038000
-2039000
-2040000
-2041000
-2042000
-2043000
-2044000
-2045000
-2046000
-2047000
Z-axis
-2000
2000
Layer 10

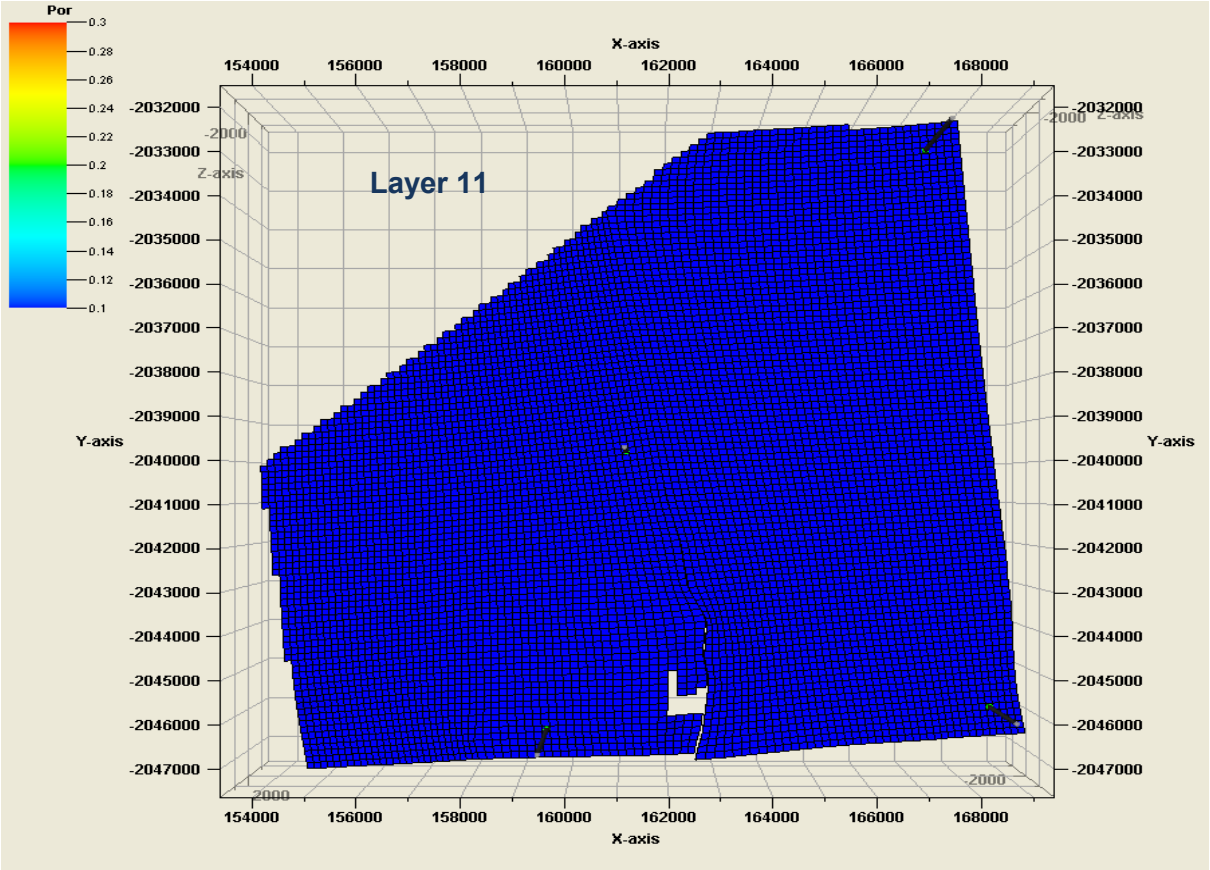
Por
0.3
0.28
0.26
0.24
0.22
0.2
0.18
0.16
0.14
0.12
0.1
X-axis
154000
156000
158000
160000
162000
164000
166000
168000
Z-axis
-2000
Layer 11
Y-axis
-2032000
-2033000
-2034000
-2035000
-2036000
-2037000
-2038000
-2039000
-2040000
-2041000
-2042000
-2043000
-2044000
-2045000
-2046000
-2047000

Appendix B

Permeability distribution of all layers in the Johansen formation

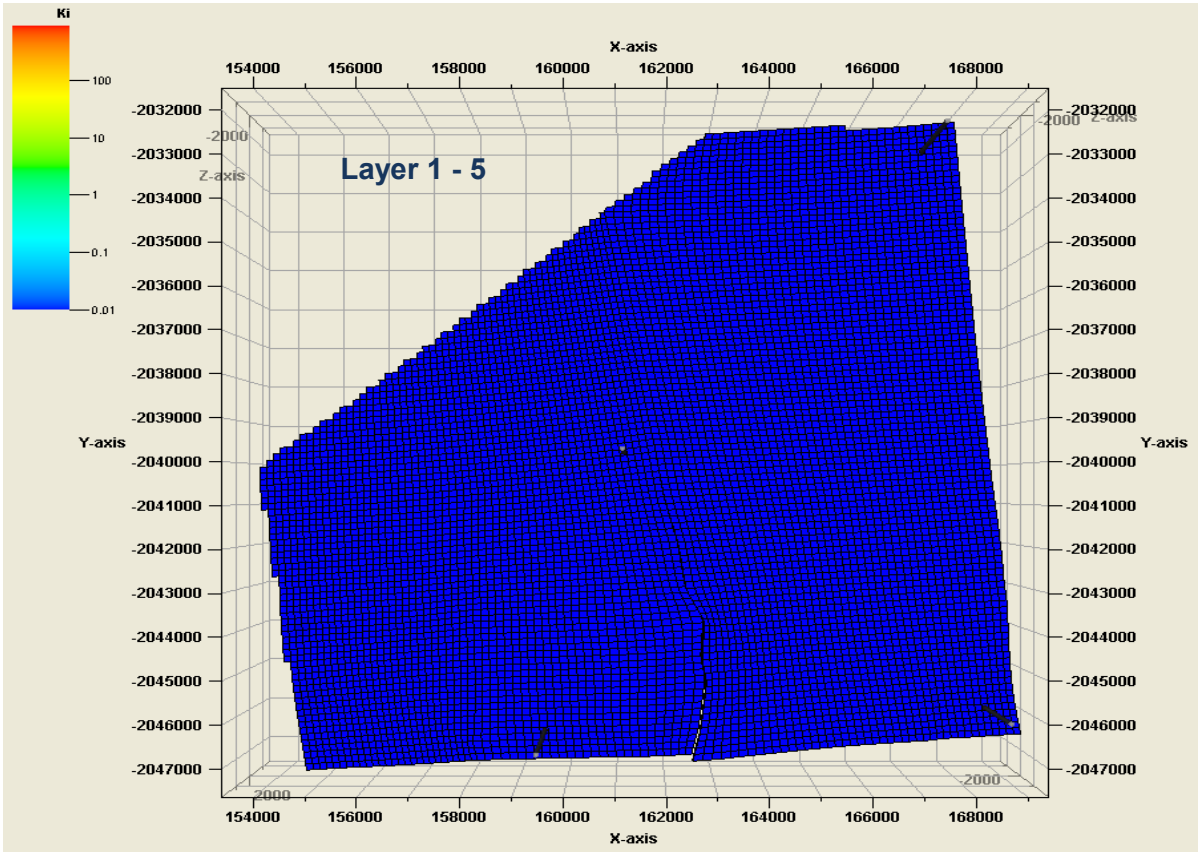

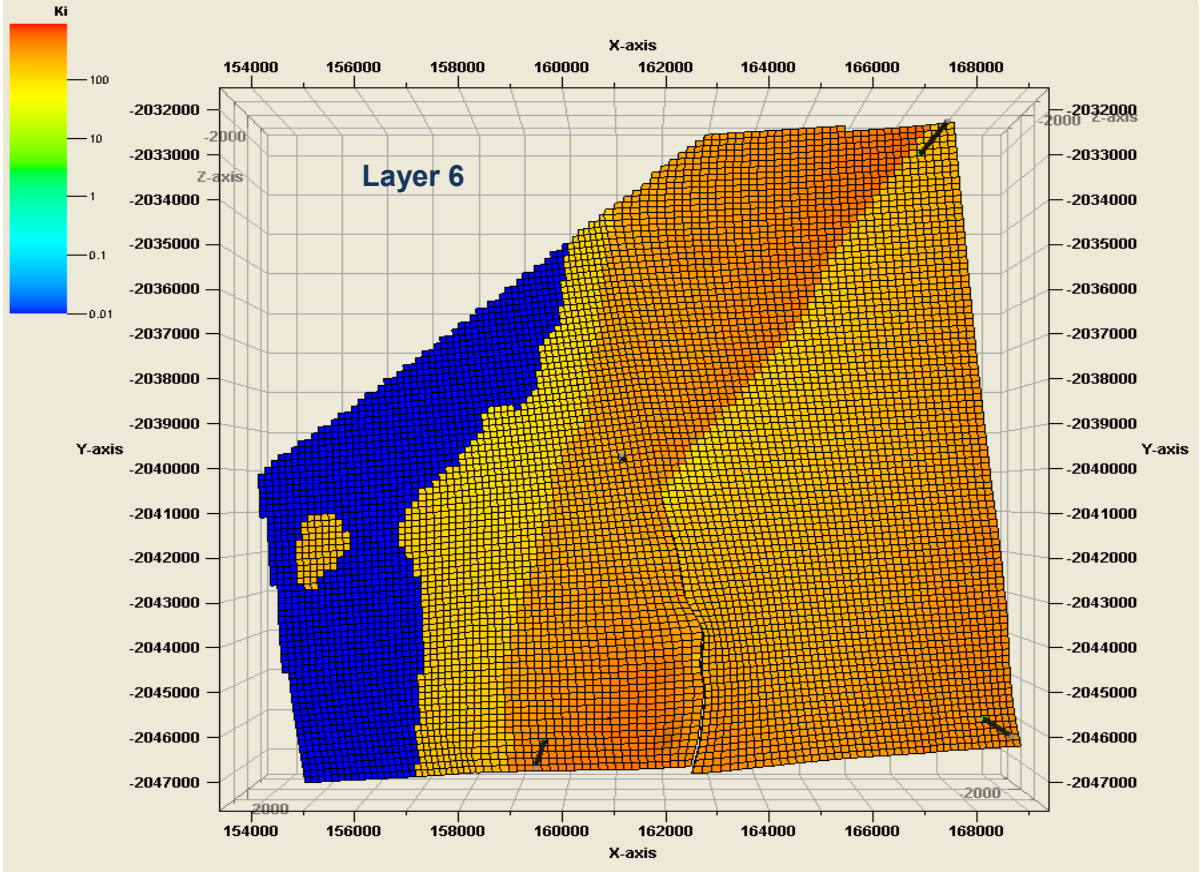

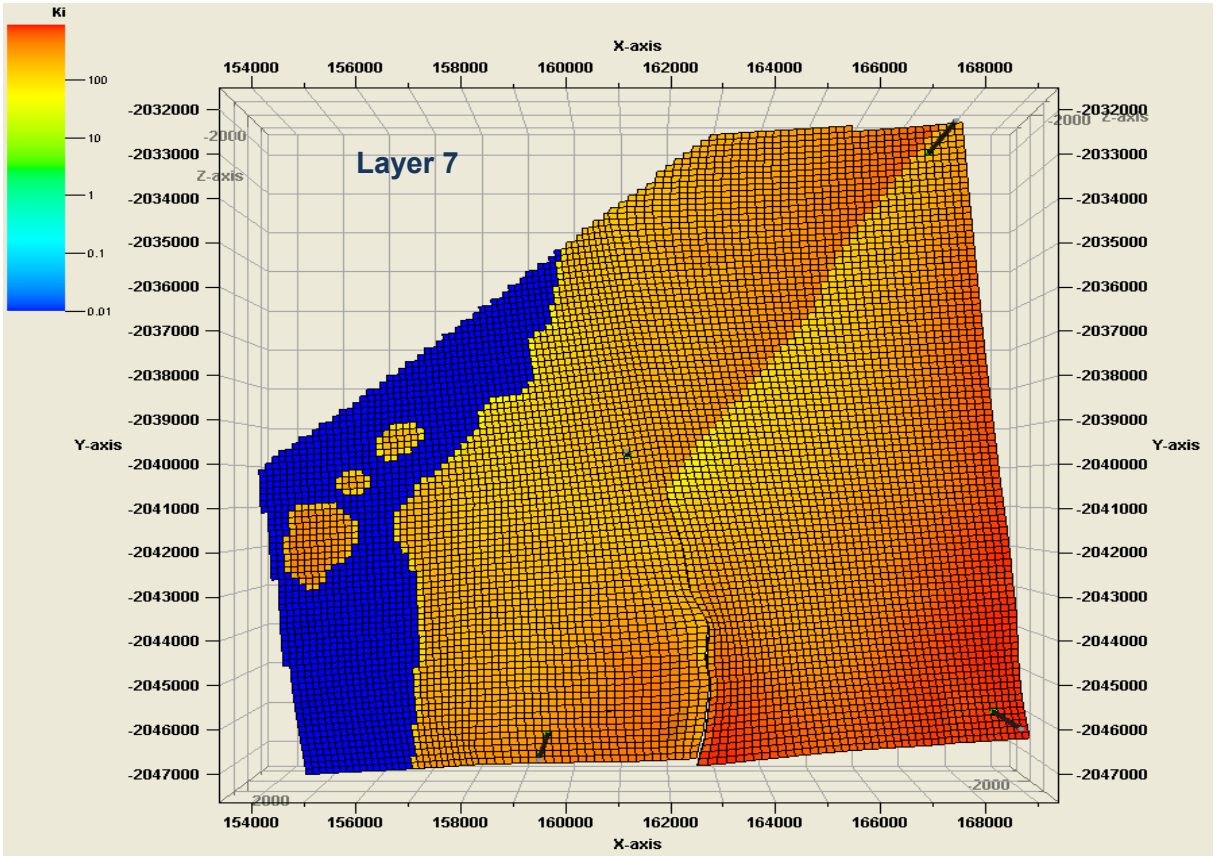
Ki
100
10
1
0.1
0.01
X-axis
154000
156000
158000
160000
162000
164000
166000
168000
Y-axis
-2032000
-2033000
-2034000
-2035000
-2036000
-2037000
-2038000
-2039000
-2040000
-2041000
-2042000
-2043000
-2044000
-2045000
-2046000
-2047000
Z-axis
-2000
2000
Layer 7

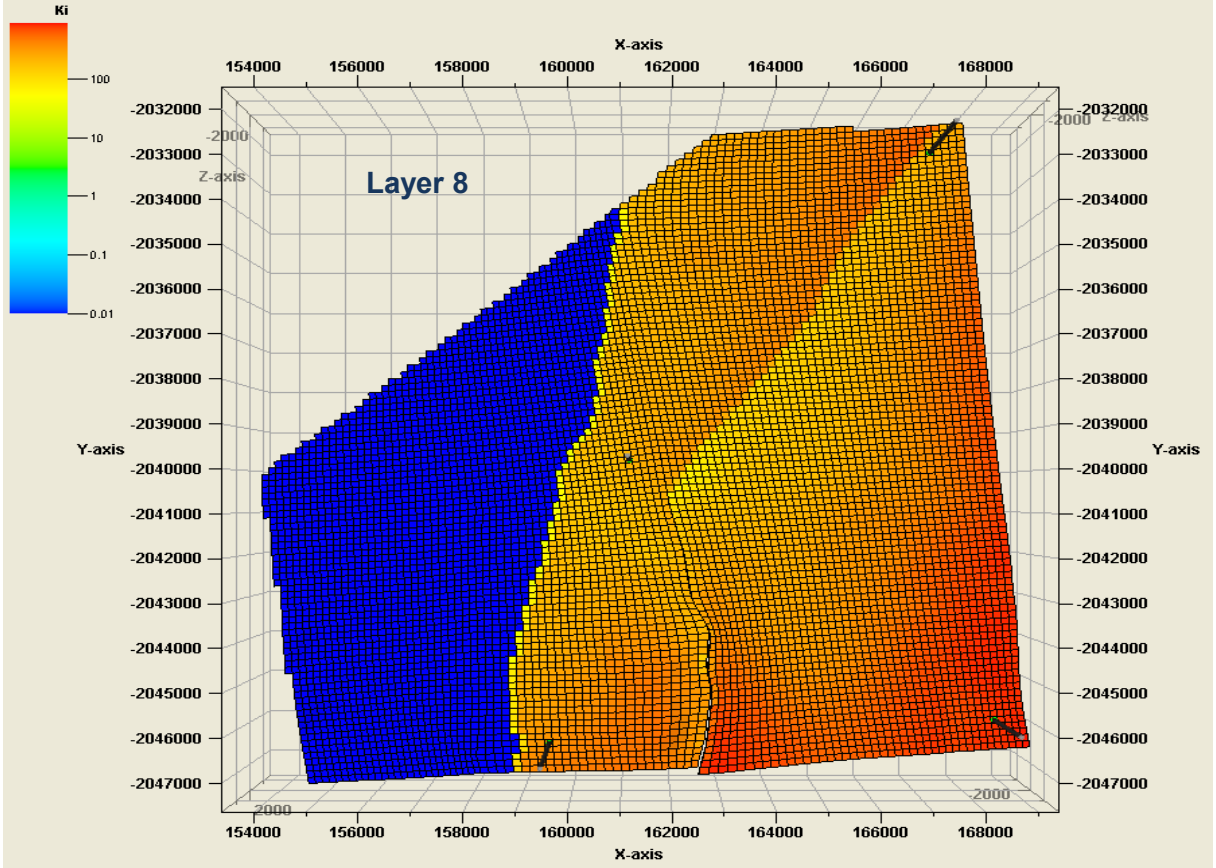
Ki
100
10
1
0.1
0.01
X-axis
154000
156000
158000
160000
162000
164000
166000
168000
Y-axis
-2032000
-2033000
-2034000
-2035000
-2036000
-2037000
-2038000
-2039000
-2040000
-2041000
-2042000
-2043000
-2044000
-2045000
-2046000
-2047000
Z-axis
-2000
2000
Layer 8

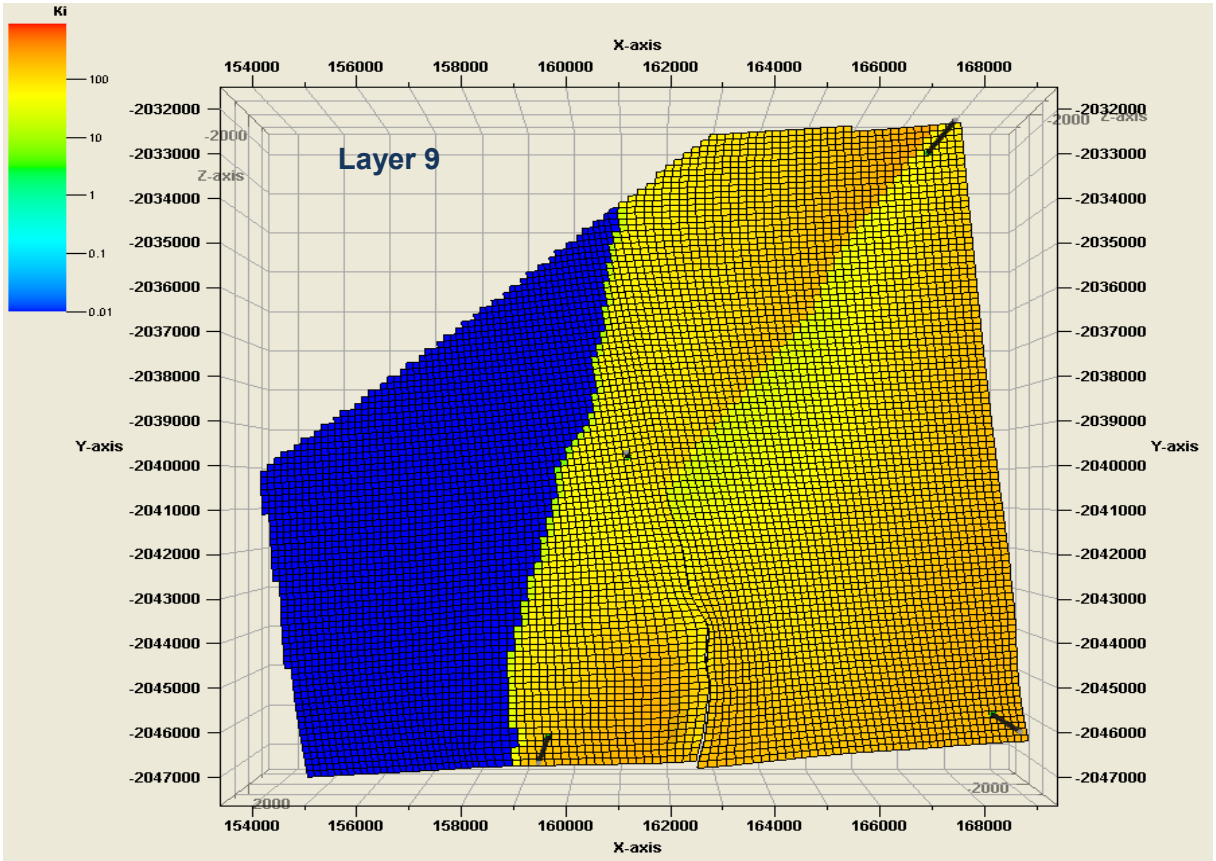
Ki
100
10
1
0.1
0.01
Layer 9
X-axis
Y-axis
Z-axis
154000
156000
158000
160000
162000
164000
166000
168000
-2032000
-2033000
-2034000
-2035000
-2036000
-2037000
-2038000
-2039000
-2040000
-2041000
-2042000
-2043000
-2044000
-2045000
-2046000
-2047000
-2000
2000

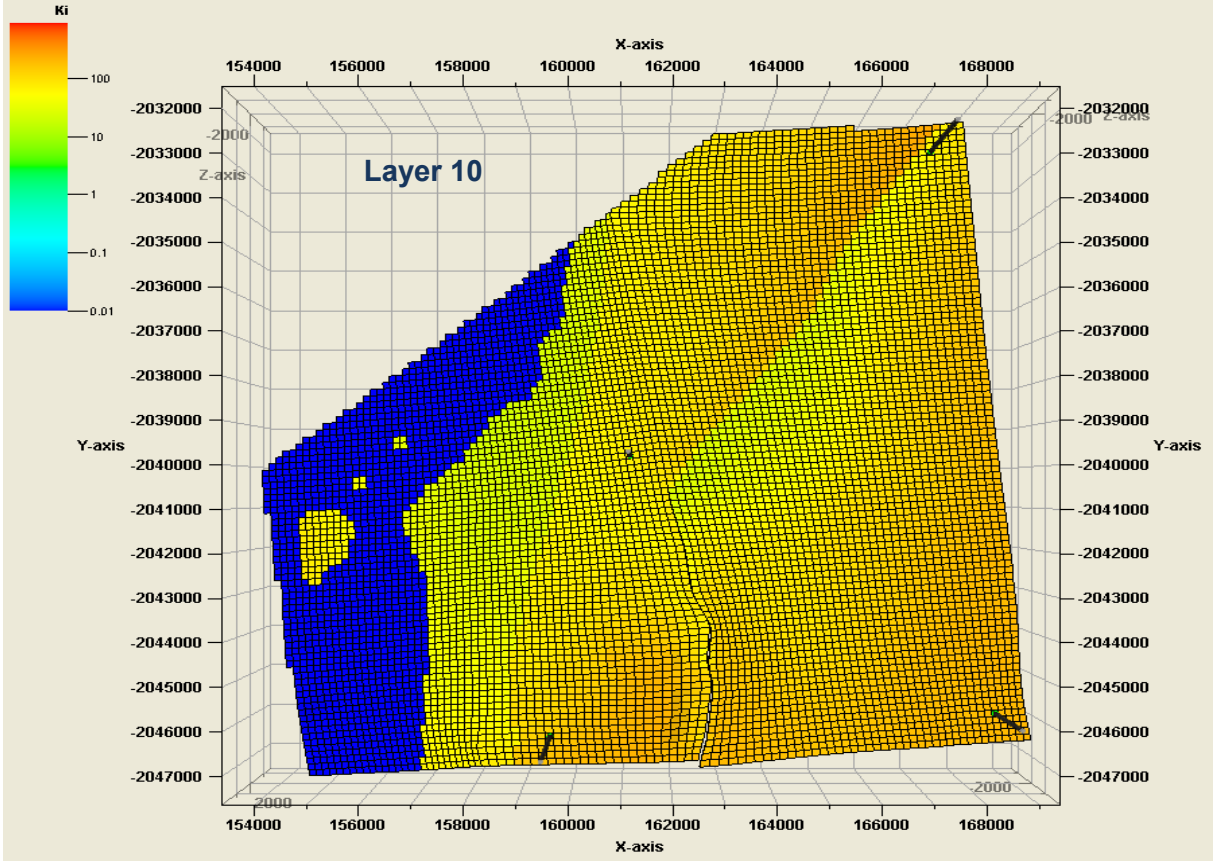
Ki
100
10
1
0.1
0.01
Layer 10
X-axis
Y-axis
Z-axis
154000
156000
158000
160000
162000
164000
166000
168000
-2032000
-2033000
-2034000
-2035000
-2036000
-2037000
-2038000
-2039000
-2040000
-2041000
-2042000
-2043000
-2044000
-2045000
-2046000
-2047000
-2000
2000

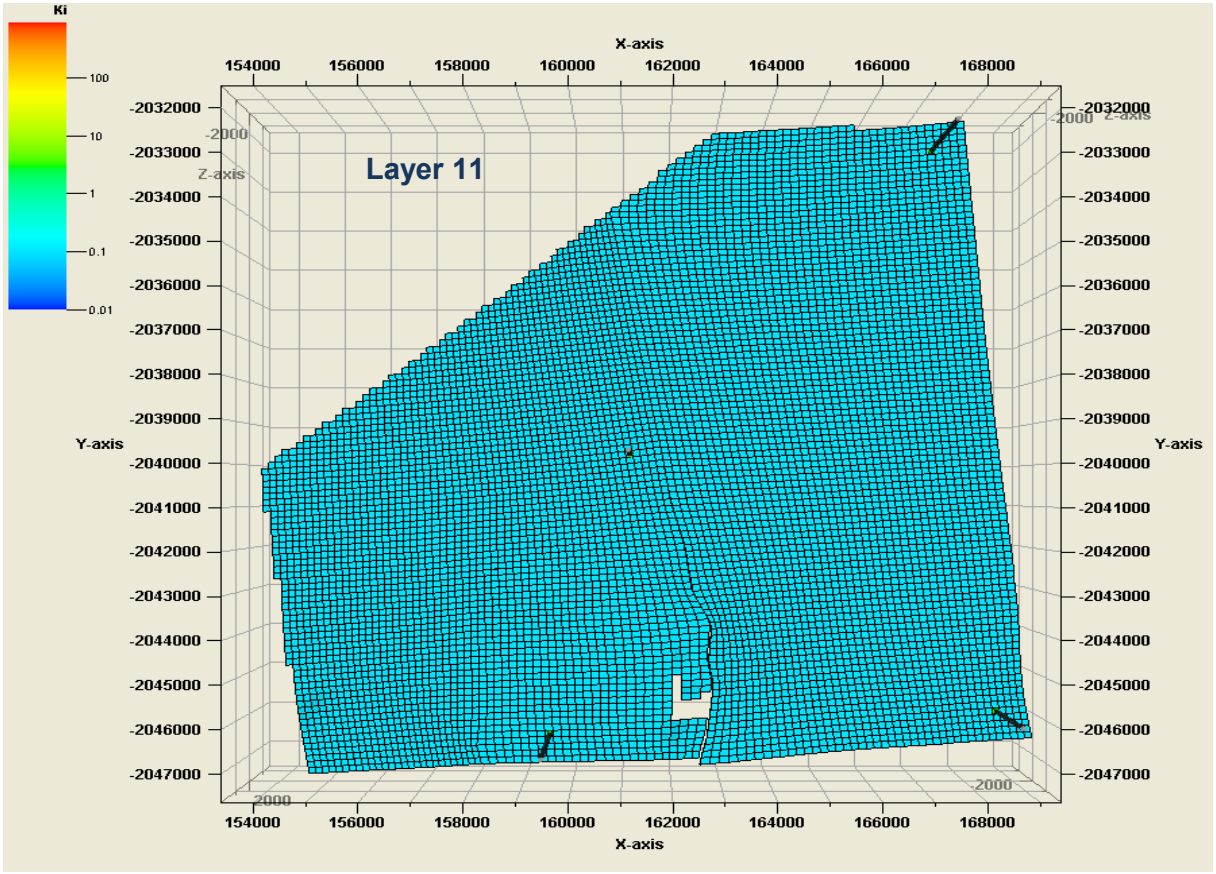
Ki
100
10
1
0.1
0.01
X-axis
154000
156000
158000
160000
162000
164000
166000
168000
Z-axis
-2000
2000
Layer 11
Y-axis
-2032000
-2033000
-2034000
-2035000
-2036000
-2037000
-2038000
-2039000
-2040000
-2041000
-2042000
-2043000
-2044000
-2045000
-2046000
-2047000

Appendix C

Well completion data

Well name	I grid block connection	J grid blocks connection	K grid blocks upper connection	K grid blocks lower connection	Operation flag	Well bore diameter [m]	Equivalent radius [m]
INJ	48	48	6	6	Open	0.1905	31.02
INJ	48	48	7	7	Open	0.1905	30.99
INJ	48	48	8	8	Open	0.1905	30.96
INJ	48	48	9	9	Open	0.1905	30.93
INJ	48	48	10	10	Open	0.1905	30.91
PROD1	5	5	6	6	Open	0.1905	29.21
PROD1	5	5	7	7	Open	0.1905	29.22
PROD1	5	5	8	8	Open	0.1905	29.22
PROD1	5	5	9	9	Open	0.1905	29.23
PROD1	5	5	10	10	Open	0.1905	29.21
PROD2	62	5	6	6	Open	0.1905	32.86
PROD2	62	5	7	7	Open	0.1905	32.87
PROD2	62	5	8	8	Open	0.1905	32.86
PROD2	62	5	9	9	Open	0.1905	32.82
PROD2	62	5	10	10	Open	0.1905	32.81
PROD3	5	95	6	6	Open	0.1905	30.90
PROD3	5	95	7	7	Open	0.1905	30.90
PROD3	5	95	8	8	Open	0.1905	30.92
PROD3	5	95	9	9	Open	0.1905	30.92
PROD3	5	95	10	10	Open	0.1905	30.91